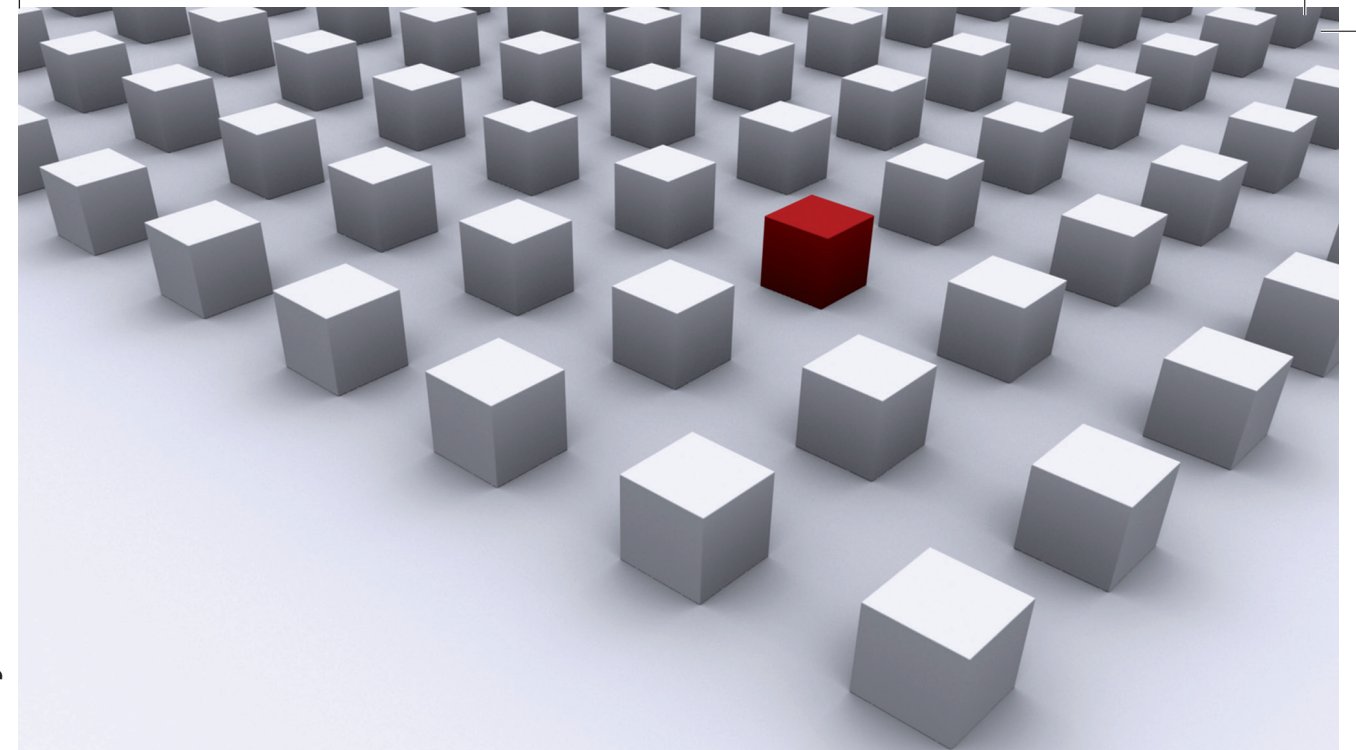


Since its first observation the Kondo effect has been a continuous drive for both theoretical and experimental physics and has seen an unprecedented renewed interest in the last years due to its observation in quantum dots. This work investigates the implications of ferromagnetic contacts (PdNi) for the transport properties in general and for the Kondo effect in particular. Despite the presence of the ferromagnetic leads, Kondo correlations are still possible. In contrast to a zero bias Kondo peak, the resonance peaks of the differential conductance are now at finite bias voltages. The reason for that is that the charge fluctuations between the quantum dot and the contacts renormalize the discrete states of the quantum dot in a spin dependent way. Intuitive formulas for the amount of splitting and its dependence on the level position are derived. Additionally, the scaling properties show that the tunneling induced exchange field influences the level structure and such the Kondo effect exactly in the same way as an external magnetic field.

Dissertationsreihe Physik - Band 27



Markus Gaaß

The Kondo effect  
in single wall carbon nanotubes  
with ferromagnetic contacts

Universitätsverlag Regensburg

Universitätsverlag Regensburg



Universität Regensburg

Markus Gaaß

27  
Dissertationsreihe  
Physik

Markus Gaaß



The Kondo effect  
in single wall carbon nanotubes  
with ferromagnetic contacts

# **The Kondo effect in single wall carbon nanotubes with ferromagnetic contacts**

Dissertation zur Erlangung des Doktorgrades der Naturwissenschaften (Dr. rer. nat.)  
der Fakultät für Physik der Universität Regensburg  
vorgelegt von

Markus Gaaß

aus Schierling

November 2011

Die Arbeit wurde von Prof. Dr. Christoph Strunk angeleitet.  
Das Promotionsgesuch wurde am 27.10.2011 eingereicht.  
Das Kolloquium fand statt am 19.12.2011.

Prüfungsausschuss: Vorsitzender: Prof. Dr. Vladimir Braun  
1. Gutachter: Prof. Dr. Christoph Strunk  
2. Gutachter: Prof. Dr. Jascha Repp  
weiterer Prüfer: Prof. Dr. Rupert Huber



## **Dissertationsreihe der Fakultät für Physik der Universität Regensburg, Band 27**

Herausgegeben vom Präsidium des Alumnivereins der Physikalischen Fakultät:  
Klaus Richter, Andreas Schäfer, Werner Wegscheider, Dieter Weiss

**Markus Gaaß**

**The Kondo effect  
in single wall carbon nanotubes  
with ferromagnetic contacts**

**Universitätsverlag Regensburg**



Bibliografische Informationen der Deutschen Bibliothek.  
Die Deutsche Bibliothek verzeichnet diese Publikation  
in der Deutschen Nationalbibliografie. Detaillierte bibliografische Daten  
sind im Internet über <http://dnb.ddb.de> abrufbar.

1. Auflage 2012

© 2012 Universitätsverlag, Regensburg

Leibnizstraße 13, 93055 Regensburg

Konzeption: Thomas Geiger

Umschlagentwurf: Franz Stadler, Designcooperative Nittenau eG

Layout: Markus Gaaß

Druck: Docupoint, Magdeburg

ISBN: 978-3-86845-088-0

Alle Rechte vorbehalten. Ohne ausdrückliche Genehmigung des Verlags ist es  
nicht gestattet, dieses Buch oder Teile daraus auf fototechnischem oder  
elektronischem Weg zu vervielfältigen.

Weitere Informationen zum Verlagsprogramm erhalten Sie unter:  
[www.univerlag-regensburg.de](http://www.univerlag-regensburg.de)

# The Kondo effect in single wall carbon nanotubes with ferromagnetic contacts



Dissertation  
zur Erlangung des Doktorgrades der Naturwissenschaften  
(Dr. rer. nat.)  
der Fakultät für Physik  
der Universität Regensburg

vorgelegt von  
**Markus Gaaß**  
aus Schierling

November 2011

Die Arbeit wurde von Prof. Dr. Christoph Strunk angeleitet.  
Das Promotionsgesuch wurde am 27.10.2011 eingereicht.  
Das Kolloquium fand statt am 19.12.2011

Prüfungsausschuss:	Vorsitzender:	Prof. Dr. Vladimir Braun
	1. Gutachter:	Prof. Dr. Christoph Strunk
	2. Gutachter:	Prof. Dr. Jascha Repp
	weiterer Prüfer:	Prof. Dr. Rupert Huber



**Für Beate**



# Contents

<b>1. Introduction</b>	<b>1</b>
<b>2. Structure and electronic properties of CNTs</b>	<b>7</b>
2.1. Lattice structure . . . . .	7
2.2. Electronic properties of carbon nanotubes . . . . .	10
<b>3. Electronic transport in mesoscopic structures</b>	<b>15</b>
3.1. Transport regimes . . . . .	15
3.1.1. Ballistic transport . . . . .	16
3.1.2. Classical transport . . . . .	17
3.1.3. Diffusive transport and localization . . . . .	17
3.2. Quantum dots and Coulomb blockade . . . . .	19
3.2.1. Classical Coulomb blockade . . . . .	19
3.2.2. Quantum Coulomb blockade . . . . .	24
3.2.3. Non-linear transport . . . . .	27
3.2.4. Quantum dots in carbon nanotubes . . . . .	29
<b>4. Kondo effect</b>	<b>33</b>
4.1. General description . . . . .	33
4.2. The Kondo effect with ferromagnetic contacts . . . . .	39
4.2.1. Polarization induced level renormalization . . . . .	42
4.2.2. Magnetization induced renormalization . . . . .	46
4.2.3. Parabolic bands in literature . . . . .	49
<b>5. Sample fabrication and experimental methods</b>	<b>53</b>
5.1. Sample fabrication . . . . .	53
5.1.1. Wafer material . . . . .	53
5.1.2. Single wall nanotubes . . . . .	54
5.1.3. Sample design . . . . .	56
5.2. Properties of the ferromagnetic alloy . . . . .	58
5.3. Experimental methods . . . . .	64
5.3.1. Low temperatures . . . . .	64
5.3.2. Transport measurements . . . . .	66

<b>6. Electronic sample characterization</b>	<b>69</b>
6.1. Sample classification . . . . .	69
6.2. Determination of the level spectrum . . . . .	70
6.3. Coupling strength and asymmetry . . . . .	76
<b>7. The Kondo splitting and its B-Field dependence</b>	<b>81</b>
7.1. Splitting of the Kondo resonance . . . . .	81
7.2. Magnetic field dependence . . . . .	86
<b>8. Scaling properties</b>	<b>93</b>
8.1. Scaling as a function of temperature . . . . .	93
8.2. Scaling as a function of magnetic field . . . . .	100
<b>9. Summary and discussion</b>	<b>111</b>
<b>A. Sample preparation parameters</b>	<b>I</b>
A.1. Substrate and alignment marks . . . . .	I
A.2. Nanotube growth . . . . .	II
A.2.1. Catalyst . . . . .	II
A.2.2. Growth . . . . .	II
A.3. Electron beam lithography and metallization . . . . .	III
<b>B. Measurement Scripts</b>	<b>V</b>
<b>Bibliography</b>	<b>IX</b>
<b>Bibliography</b>	<b>IX</b>
<b>Acknowledgments</b>	<b>XIX</b>



# List of Figures

1.1. Datta-Das spin field effect transistor . . . . .	2
2.1. Lattice structure of a carbon nanotube . . . . .	8
2.2. Carbon nanotubes with chiral indices (7,7), (12,0), and (8,3). . . . .	9
2.3. Real space and reciprocal lattice of graphene . . . . .	11
2.4. Band structure of graphene . . . . .	12
2.5. Dispersion relations for carbon nanotubes with chiral indices (5,5), (9,0), and (10,0) . . . . .	13
2.6. Density of states for carbon nanotubes with chiral indices (5,5), (9,0), and (10,0) . . . . .	14
3.1. Examples of ballistic and diffusive transport in carbon nanotubes. . . . .	17
3.2. Equivalent circuit of a quantum dot connected to leads . . . . .	20
3.3. Schematics of Coulomb blockade . . . . .	21
3.4. Classical Coulomb blockade . . . . .	22
3.5. Temperature dependence of classical and quantum Coulomb oscillations . . . . .	25
3.6. Non-linear transport spectroscopy . . . . .	28
3.7. Stability diagrams for different transport regimes. . . . .	30
3.8. Shell filling in the case of four-fold symmetry. . . . .	32
4.1. Temperature dependence of the resistance in metals and the conductance in quantum dots . . . . .	34
4.2. Kondo effect in metals and quantum dots . . . . .	35
4.3. Schematic of virtual processes resulting in Kondo correlations . . . . .	36
4.4. Main characteristics of a Kondo quantum dot . . . . .	37
4.5. Schematic of virtual processes resulting in Kondo correlations in finite field . . . . .	38
4.6. Effect of an external magnetic field on the Kondo effect . . . . .	39
4.7. Utilizing the Kondo resonance as spectroscopic tool . . . . .	40
4.8. Definition of the terms magnetization and polarization as used in this work . . . . .	42
4.9. Schematic of spin dependent charge fluctuations for finite polarization . . . . .	43
4.10. Schematic of spin dependent charge fluctuations for finite magnetization . . . . .	47
4.11. Band structures considered in groundbreaking theoretical works . . . . .	50
4.12. Spectral functions for different band structures calculated via NRG . . . . .	51
4.13. Influence of an external field on the spectral function . . . . .	51

5.1. Typical arrangement of alignment marks . . . . .	55
5.2. Structure design realized in eDraw <sup>TM</sup> . . . . .	56
5.3. Scanning electron micrographs of a typical sample . . . . .	57
5.4. Tunneling magnetoresistance in a carbon nanotube spin transistor . . . . .	59
5.5. Ab-initio calculations of the band structure for the two components of Pd <sub>0.3</sub> Ni <sub>0.7</sub> . . . . .	61
5.6. Ab-initio calculations of the band structure of Pd <sub>0.3</sub> Ni <sub>0.7</sub> . . . . .	62
5.7. Measurement equipment . . . . .	65
5.8. Measurement schematic . . . . .	67
6.1. Linear conductance as a function of gate voltage at different temperatures	71
6.2. Reproducibility of linear conductance measurements . . . . .	72
6.3. Charging diagram of sample AC . . . . .	73
6.4. Determination of characteristic electronic parameters . . . . .	74
6.5. Determination of the coupling strength between nanotube and leads . . . .	77
6.6. Determination of the asymmetry between coupling strength to source and to drain contact . . . . .	78
7.1. Close up of split Kondo resonance . . . . .	82
7.2. Amount of level splitting read off from Kondo resonance . . . . .	83
7.3. Comparison of Kondo temperature and exchange splitting as functions of tunnel coupling . . . . .	85
7.4. Experimental magnetic field dependence of the splitting of a Kondo reso- nance . . . . .	88
7.5. Theoretical magnetic field dependence of the splitting of a Kondo resonance	89
7.6. Line traces of experimental and theoretical conductance at different field values . . . . .	90
7.7. Full magnetic field dependence of a split Kondo resonance . . . . .	91
8.1. Numerically modeled magnetic field dependence of the Kondo conductance	94
8.2. Comparison of the temperature dependence of the conductance at zero and finite field . . . . .	95
8.3. Fit of the temperature dependence of the Kondo conductance in a finite field	96
8.4. Temperature dependence of the conductance on split Kondo resonances .	97
8.5. Different fitting efforts of $G(T)$ for the split Kondo case . . . . .	98
8.6. Magnetoconductance for six different gate voltages . . . . .	101
8.7. Numerical comparison between Kondo temperature and Kondo field . . .	102
8.8. Definition of $B_{\text{exch}}$ and $G(B_{\text{exch}})$ . . . . .	104
8.9. Scaling result for the magnetoconductance in the Kondo regime . . . . .	105
8.10. Comparison between theoretically expected and experimentally found level splitting and Kondo temperature . . . . .	107
8.11. Half width at half maximum of bias traces at zero effective field . . . . .	109

---

9.1. Possible charge fluctuations for a multi level quantum dot . . . . .	112
9.2. Theoretical predictions for a Kondo dot with spin orbit interaction . . . .	115
9.3. Substructure in the differential conductance at finite fields . . . . .	116



# 1. Introduction

In 1965 Intel co-founder Gordon E. Moore formulated an empirical law - that the number of transistors in an integrated circuit would double every year. It has later been refined to a period of two years [1]. The actual development of integration density has been following this law surprisingly close for more than 40 years now [2]. Although the real value of the law and its scientific legitimacy might be questionable - some even speak of a self-fulfilling prophecy - it can serve very well to describe a general trend of miniaturization in modern information technology. If this trend continues, it is foreseeable that structures of such small size will be reached that quantum effects of charge carriers can no longer be neglected. From the importance of information technology in our modern society alone one can already understand the huge interest in mesoscopic physics. This term describes a subfield of solid state physics that focuses on system sizes between the microscopic length scale, dealing with length scales of single atoms, and the macroscopic world that describes roughly speaking bulk properties. The dominant length scales in mesoscopic physics are usually several 10nm to 1000nm.

The understanding of fundamental quantum mechanical processes in solids is important for the ongoing miniaturization of integrated circuits. But even with this knowledge it is not possible to avoid another effect going hand in hand with higher integration density, that is heat dissipation. A very elegant way of increasing the degree of efficiency of information processing alongside with the miniaturization would be to use an additional parameter besides the charge to encode information. From quantum mechanics it is known that electrons carry not only a fundamental charge quantity but also have a spin [3]. Analogous to the field of electronics, where the charge is the relevant quantity, it has been suggested to design logic elements that use the spin rather than the charge for their operations. To stress the close connection to electronics this field of information processing is called spin-electronics or short spintronics [4]. A prominent conceptual example from spintronics is the spin field-effect transistor by Datta and Das [5], see figure 1.1, whose analogue is the field-effect transistor well known from electronics. The three key ingredients to spin based information processing are initialization of a certain spin state, its manipulation, and finally the read out [6].

The field of spintronics is not only a highly interesting field of fundamental research in itself but also the main focus of a dedicated research initiative at the University of Regensburg, the Collaborative Research Center (SFB) "Spin Phenomena in Reduced Dimensions". The reduced dimensions in the present case are provided by carbon nanotubes and

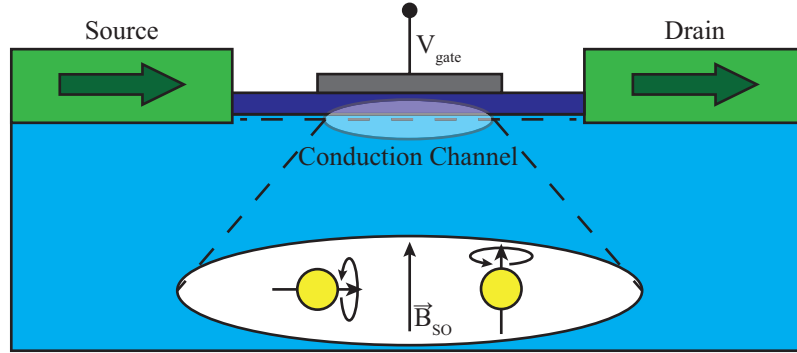


**Figure 1.1.:** Concept of a spin analog of the electric field effect transistor proposed by Supriyo Datta and Biswajit Das in 1990 [5]. The left electrode injects charge carriers with a spin parallel to the magnetization into the conducting channel. The resistance for the charge carriers at the other lead, the drain electrode, depends on whether the spin orientation of the particle has changed during its path along the channel. This can happen by spin-orbit interaction, where the orbital momentum of the particle influences its spin. This mechanism can be visualized as an effective magnetic field in the channel, consequently being referred to as spin-orbit field. In some materials this effective spin-orbit field is known to depend on an applied electric field. This would - via a gate voltage  $V_{gate}$  - give an all electric control over the resistance of the device due to the spin orientation.

the quantum dots defined in them. The spin phenomena that are investigated are tunneling induced exchange fields and the Kondo effect.

Carbon nanotubes (CNT) possess many properties that make them interesting candidates for the realization of spin sensitive logic elements. Being composed mainly of the far more frequent carbon isotope  $^{12}\text{C}$  which has no nuclear spin [7] the charge carrier spin lifetime and coherence is not limited by the hyperfine interaction. Thus, spins can relax predominantly only via spin-orbit interaction (SOI). In principle spin-orbit interaction is present in every carbon nanotube due to its curvature [8]. However, resolving SOI requires very clean carbon nanotubes [9]. Nowadays well controlled processes allow to fabricate very regular carbon nanotubes, showing ballistic transport over length scales of several 100nm and such also scattering events do not limit the coherence of the wave function. Employing these extraordinary electronic properties, there has been much research on effects like tunnel magnetoresistance, spin valve behavior, and phase coherence in carbon nanotubes, with the most prominent examples being Refs. [10–14].

Besides the remarkable electronic properties mentioned above, also other astonishing features of carbon nanotubes, more concerning the structural properties, are often discussed. These are, e.g., the potential for an immense current density of up to  $10^9 \text{ A cm}^{-2}$  [15] and

a mechanical stiffness expressed in terms of the Young's modulus which can be as high as 1 TPa [16, 17]. This latter feature has made nanotubes part of science fiction-like considerations of constructing a space elevator.<sup>1</sup> Standard building materials like steel or brick have the limitation of collapsing under their own weight once reaching a certain height, a limitation that affects carbon nanotubes much less. In addition, also more “down to earth” applications of carbon nanotubes are discussed, e.g. using them as drug delivery systems in biological or medical applications [18].

The field of carbon nanotube research is still rather young and really began to thrive with the discovery of multi wall nanotubes in transmission electron microscopy (TEM) experiments by Sumio Iijima in 1991 [19] and the subsequent observation of single wall nanotubes [20, 21]. It should be mentioned here however, that there is an ongoing debate in the scientific community [22] about whether the first observation of nanotubes was already made in 1952, when two Russian scientists published images indeed showing structures very reminiscent of the later observed nanotubes [23]. Since then there has been tremendous progress in the fabrication of nanotubes, which gave the possibility to use them in a controllable and reproducible fashion in scientific experiments. An essential step was the ability to fabricate carbon nanotubes in a way that allows to contact them individually. This can be achieved by different means. For fundamental research, the most common process today is chemical vapor deposition [24], which allows to investigate the electronic structure of single, defect-free carbon nanotubes [25–28]. Since then many hallmark experiments from mesoscopic physics have been reproduced or even conducted for the first time in carbon nanotubes. Coherent transport in an open quantum dot analogous to the optical case of a Fabry-Perot interferometer was for instance beautifully demonstrated in [29], as well as phase coherence along a multi wall carbon nanotube seen in Aharonov-Bohm oscillations in a magnetic field along the tube axis [30]. With the ability to fabricate quantum dots with varying contact transparencies the investigation of carbon nanotubes in different transport regimes [31] became feasible. This opened up the possibility to research many fundamental phenomena from condensed matter physics in the controllable sandbox that quantum dots offer.

One of these effects that has been a very fruitful drive for the development and testing of theoretical methods is the so-called Kondo effect. The still important and instructive field of Kondo physics started already in the 1930s. Experiments showed that the resistance of solids containing a small amount of ferromagnetic impurities exhibit an unusual temperature dependence. For reviews of the experimental results see e.g. Refs. [32, 33]. Up to that point, two distinct temperature dependences were known. For most metals the resistance saturates at a finite value for  $T \rightarrow 0$  K. A second class of metals, discovered in 1911 by Heike Kamerlingh Onnes [34], is given by superconductors, displaying an immeasurably low resistance below a certain critical temperature.

Metals containing magnetic impurities, however, show an increase of the resistance below

---

<sup>1</sup>cf. e.g. [http://science.nasa.gov/science-news/science-at-nasa/2000/ast07sep\\_1](http://science.nasa.gov/science-news/science-at-nasa/2000/ast07sep_1)



a characteristic temperature. In 1964 Jun Kondo successfully explained the experimental observation of this increasing resistance in dilute ferromagnets [35] with an enhanced scattering probability due to a screening of unpaired spins. The model proposed by Kondo however predicted a logarithmic divergence of the conductance for  $T \rightarrow 0\text{K}$ . Later Appelbaum [36], Anderson [37], and Wilson [38] were able to fully explain the unusual temperature behavior.

In these earlier years it was certainly not foreseen that the same effect would face a revival in mesoscopic physics as it did in the last years [39]. In 1998, the first observations of the Kondo effect were made in semiconductor based quantum dots by Goldhaber-Gordon et al. [40], Cronenwett et al. [41], and Schmid et al. [42]. Only shortly after this finding in two dimensional electron systems, the Kondo effect was also observed in carbon nanotubes by Nygård et al. [43]. The experimental fingerprint of the Kondo effect in quantum dots [44] is an increase of the conductance with a peak at zero bias rather than an increase of the resistance as might have been expected from bulk magnetic alloys. The value of the conductance at zero bias shows a very characteristic temperature dependence that is often used to identify an observed conductance enhancement as Kondo phenomenon. Another hallmark of the Kondo effect is that the conductance peak splits under the influence of an external magnetic field.

Being able to fabricate magnetic contacts to carbon based molecular conductors as well as to semiconductor quantum dots allows to investigate the effect of magnetization and spin polarization in the leads on the Kondo effect. The main observation in such experiments is a splitting of the Kondo resonance without an external field. This was observed, e.g., in semiconductor based devices [45, 46] formed by self assembled InAs quantum dots with Co leads or by magnetically focussing polarized charge carriers into the source contact of a split gate defined quantum dot. In another experiment a Buckminster Fullerene was contacted by nickel electrodes [47] causing the Kondo conductance to show a very strong splitting in zero field. Finally, the most influential experiment for this work has been performed with carbon nanotubes connected to nickel leads [48]. In this case the Kondo conductance did not only show a splitting in zero field but also displayed a very peculiar gate voltage dependence. There has already been extensive theoretical work [49–54] describing a renormalization of the level position on the quantum dot by tunneling induced exchange interaction. This thesis aims at experimentally complementing the rich theoretical literature. It is remarkable that the exchange field is zero when the contacts are magnetized anti-parallel and is on the order of Tesla if the magnetization is parallel. This means that with coercive fields on the order of 100 mT exchange fields on the order of several Tesla can be turned on and off. Also, since the exchange field is a result of the band structure of the leads, its strength is very stable and should surpass externally applied fields in this regard.

This thesis is organized as follows. Due to both their structural and electronic properties, carbon nanotubes are seen as promising candidates for further progress in modern

information processing. Consequently, chapter 2 provides a thorough introduction to the mechanical and electronic structure of carbon nanotubes. From that the electronic properties will be derived following the usually employed tight binding argumentation. That leads, e.g., to the explanation why nanotubes can either be metallic or semiconducting.

Chapter 3 begins with an introduction of important general concepts of mesoscopic transport. The predominant part of this chapter is devoted to quantum dots (QD) and the electronic transport through them. Important concepts like Coulomb blockade and transport spectroscopy will be introduced in this chapter. With this knowledge the basic properties of nanotube quantum dots like charging energy and level spacing can be derived from the experimental data.

After the chapter on general transport, chapter 4 deals with the many particle phenomenon called Kondo effect. The description is mainly phenomenological, following the experimental observations mentioned in literature. This leads from ferromagnetic impurities in bulk metals to semiconductor quantum dots all the way to carbon nanotube quantum dots. The second part of this chapter contains the main theoretical preparation for understanding the presented experiments. It is sketched both qualitatively and quantitatively how the presence of ferromagnetic contacts influences and alters the level structure of the quantum dot. These changes of the level structure in turn are reflected in the Kondo effect by a splitting of the conductance resonance. Two basic cases of magnetic band structures in the leads, finite polarization and finite magnetization, are discussed and their separate consequences for the transport properties summarized. The final result is that for both cases intuitive expressions for the expected size of the effect in terms of accessible quantities are given.

After the focus on theory in the first half of the thesis, the second part, describing the experimental work, starts in chapter 5 with an overview of the sample preparation steps as well as the sample properties and the measurement method. Here also the magnetic properties of the contact material that were measured within the diploma thesis of D. Steininger [55] are compared to literature like Refs. [56–58].

In chapter 6 measurements on two different CNT devices are evaluated in order to gain access to important electronic parameters of the nanotube. From transport spectroscopy the level structure is determined by giving numerical values for the charging energy, the level spacing, and the subband mismatch. The remainder of this chapter shows exemplary for one charge state the determination of the coupling strength as well as the coupling asymmetry.

A detailed qualitative and quantitative comparison between the theoretical predictions of chapter 4 and the experimental results is done in chapter 7. It is shown that the finite spin polarization and/or magnetization in source and drain contacts generates a tunneling induced exchange field. This results in a splitting of the Kondo resonance. With reference to the theoretical works that laid out the ground for the understanding, the splitting of

the Kondo resonance is explained. In addition also the dependence on an external field is investigated in this chapter.

Finally chapter 8 shows that the scaling properties, known to be present for the Kondo effect with normal leads, are found also for ferromagnetic contacts. While the conductance in the normal case scales universally with the temperature at zero field or with the field at zero temperature, for ferromagnetic contacts this universality is recovered if the field is replaced by an effective field.

At the end of this work, chapter 9 presents a short summary and a discussion of possible additional effects that have been excluded during the discussions in the main part. These are a potential extension of the single Anderson impurity model to the case of a multilevel quantum dot, i.e. a carbon nanotube, as well as spin-orbit interaction that might additionally influence the level structure. It concludes with a short outlook onto possible future experiments for gaining further insight into this fascinating field of spin dependent transport through mesoscopic structures.

## 2. Structure and electronic properties of carbon nanotubes

This chapter summarizes the most important structural, electronic and transport properties of carbon nanotubes, following Refs. [59–61]. Besides enabling the reader to follow the interpretations of the experimental results in chapter 6 and the following chapters, many important quantities of carbon nanotubes are introduced and defined.

### 2.1. Lattice structure

In nature, crystalline carbon appears in two variations which differ in the number of valence bonds of the carbon atoms. In one case, one  $s$ -orbital and two  $p$ -orbitals hybridize into three  $sp^2$ -orbitals; in a second case one  $s$ -orbital and three  $p$ -orbitals form four  $sp^3$ -orbitals through hybridization. In the latter case the result is a tetrahedral unit which forms a three dimensional network known as diamond which is very stiff, transparent, and insulating with a band gap of about 6 eV. The  $sp^2$ -hybridization results in a planar honeycomb lattice. Stacking of such planes upon each other builds up graphite. This hexagonal lattice can also be viewed as a superposition of two trigonal lattices, since the corner atoms of the hexagons are only equivalent to every second other corner point. The resulting different “flavors” of carbon atoms are often marked by lattice sites A and B [compare figure 2.3]. A single example of such a sheet is called graphene; this has become increasingly important since its first experimental isolation in 2004 [62], which ultimately led to awarding the pioneers of the field, Andre Geim and Konstantin Novoselov, the Nobel Prize in Physics in 2010.

Even sooner than the observation of isolated atomically thin carbon planes, in 1952, L. V. Radushkevich and V. M. Lukyanovich [23] and then again later, in 1991, S. Iijima discovered helical microtubules of graphene in a tunneling electron microscope [19]. These tubes with walls of carbon can be imagined to be constructed by seamlessly rolling up a graphene sheet into a cylinder that consequently has the thinnest possible wall thickness of one atom. Next to these just mentioned single wall carbon nanotubes (SWCNT) there are two other basic forms which are frequently observed. Two or more nanotubes arranged coaxially form what is called a multi wall carbon nanotube (MWCNT), and sev-

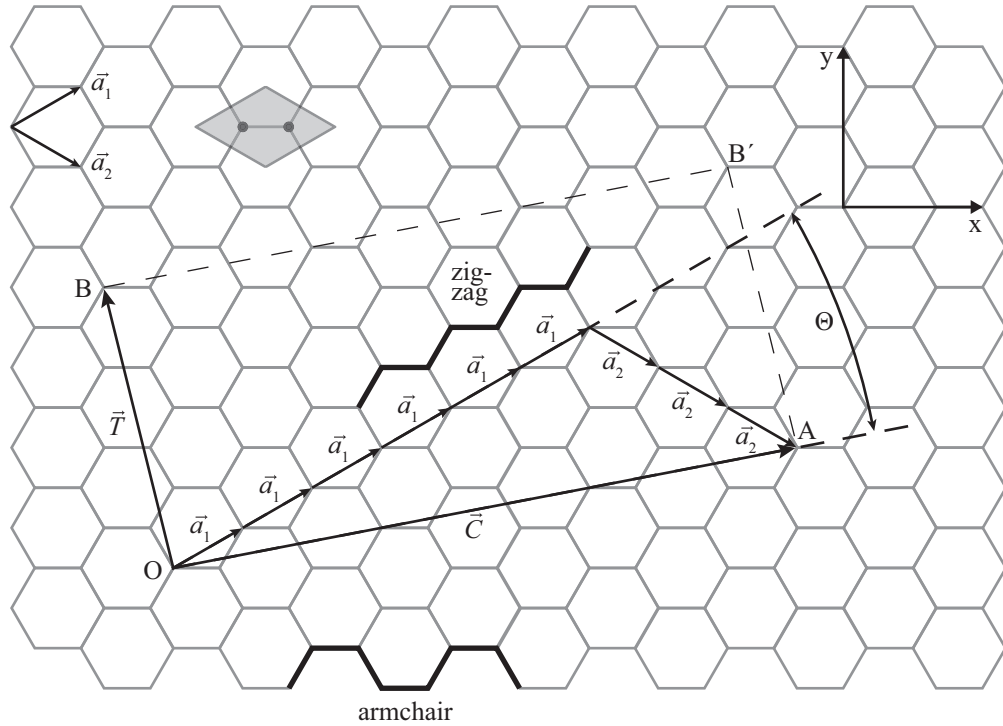


**Figure 2.1.:** A carbon nanotube can be imagined as being constructed by rolling up a graphene sheet. Graphene consists of a hexagonal Bravais lattice with one carbon atom at every corner point. In the top left corner the two atomic unit cell (shaded area) and the two basis vectors  $\vec{a}_1$  and  $\vec{a}_2$  are shown. One specific example of how a nanotube could be constructed is indicated by the vectors  $\vec{T}$  and  $\vec{C}$ . The point O is mapped onto point A so that  $\vec{C}$  runs once around the circumference of the tube. Thus,  $\vec{T}$  points along the tube axis. In this specific example a (6,3) chiral nanotube is shown (see text for details). The chiral angle is indicated as  $\Theta$ . The two special cases of  $\Theta = 0$  (zigzag) and  $\Theta = 30^\circ$  (armchair) are indicated as blue lines.

eral carbon nanotubes grouped together by van der Waals interaction appear as a bundle of carbon nanotubes.

Nanotubes can be generated by a number of different methods [63] including arc-discharge, laser ablation, chemical vapor deposition (CVD), and high pressure CO conversion (HiPCO). The process of CVD can be briefly sketched as follows. By providing a feedstock of carbon in form of a hydrocarbon gas (e.g. methane) and decomposing it by metal catalysts at growth temperatures between  $500^\circ\text{C}$  and  $1000^\circ\text{C}$  carbon nanotubes grow out from the catalysts in more or less random directions. This is the method used to grow the nanotubes in the present work and hence it will be described in more detail in chapter 5 and appendix A.

Being the building block for all three forms of nanotubes, the structure of a SWCNT will

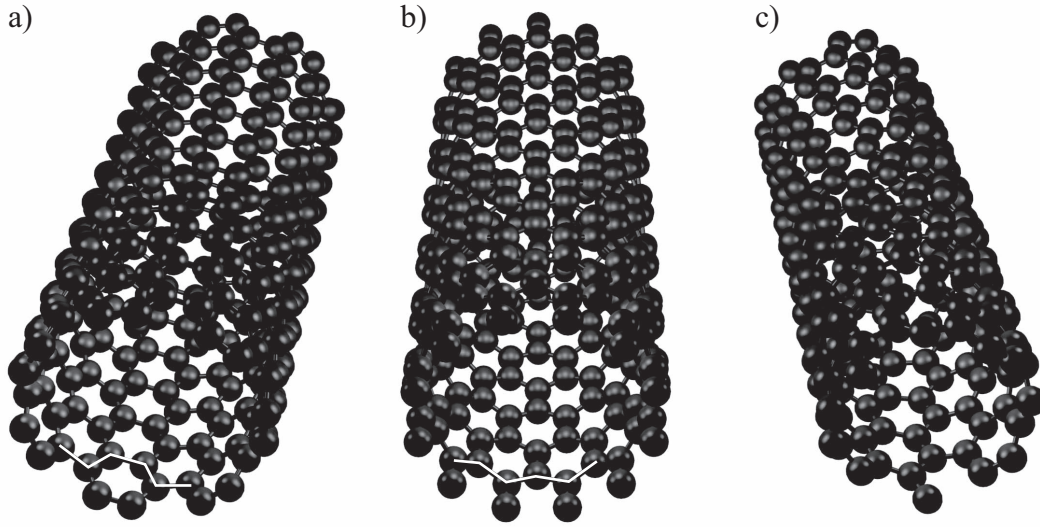


**Figure 2.2.:** Three examples of carbon nanotubes with different chiralities. The respective chiral indices are (a) (7,7), (b) (12,0), and (c) (8,3). These correspond to an armchair [indicated by the yellow line in (a)], a zig-zag [indicated by the yellow line in (b)], and a chiral tube. The high symmetry of the achiral tubes can best be seen when looking along the tube axis.

be described in more detail in the following. The picture of rolling up a single sheet of graphene has already been mentioned. This procedure can be carried out in an infinite number of ways. The outcome are tubes that differ not only in diameter but also in a property called chirality. The vector along which the carbon nanotube is rolled up and which accordingly then runs once around the circumference is called the chiral vector  $\vec{C}$ , compare figure 2.1. It can be expressed in terms of basis vectors as  $\vec{C} = n\vec{a}_1 + m\vec{a}_2$ , where  $n$  and  $m$  are called chiral indices. The shortest lattice vector pointing along the tube axis is denoted by  $\vec{T}$  and defines the lattice translations in axial direction. The diameter  $d$  and the so-called chiral angle  $\Theta$  [cf. figure 2.1] can be expressed in terms of  $(n, m)$  as

$$d = \frac{C}{\pi} = \frac{a}{\pi}(m^2 + mn + n^2)^{1/2} \quad (2.1)$$

$$\Theta = \arctan\left(\frac{\sqrt{3}m}{m + 2n}\right). \quad (2.2)$$

Here  $a = \sqrt{3}a_{CC}$  is the lattice constant and  $a_{CC}$  the nearest neighbor distance (i.e. bond length) of the carbon lattice (for graphite  $a_{CC} = 0.142\text{nm}$ ). There are two distinct cases in which the nanotube is highly symmetric and non-chiral. These two cases have chiral indices  $(n, 0)$  and  $(n, n)$  and are called “zigzag” and “armchair” nanotubes due to how the honeycomb lattice looks when following  $\vec{C}$  [cf. figure 2.1]. The general case of  $(n, m)$  is simply called a chiral nanotube [cf. figure 2.2]. The area  $OAB'B$  defined by the vectors

$\vec{C}$  and  $\vec{T}$  is the unit cell of the carbon nanotube, as opposed to the vectors  $\vec{a}_1$  and  $\vec{a}_2$  which define the unit cell of graphene. This connection allows to determine the number of hexagons  $N$  that are building up the unit cell of the carbon nanotube as

$$N = \frac{|\vec{C} \times \vec{T}|}{|\vec{a}_1 \times \vec{a}_2|}. \quad (2.3)$$

Since each hexagon contains two carbon atoms there are  $2N$  carbon atoms in the unit cell.

## 2.2. Electronic properties of carbon nanotubes

The electronic properties of carbon nanotubes are deduced from those of graphene following the same line of arguments as already mentioned in the previous section on the structure of nanotubes. At first one considers a flat surface of graphene and uses a tight binding approach to determine the band structure. The next step is often referred to as zone folding, i.e., rolling up the flat carbon sheet and imposing periodic boundary conditions for the wave functions along the circumference of the nanotube. In figure 2.3 the direct and reciprocal lattices of graphene are shown. The reciprocal lattice is again a hexagonal lattice but rotated by  $90^\circ$  with respect to the direct lattice.

It has already been pointed out that the graphene unit cell contains two atoms, each with three  $sp^2$ - and one  $p_z$ -orbital. This gives a total of six  $sp^2$ -orbitals which form 3  $\sigma$ - and 3  $\sigma^*$ -orbitals which are called bonding and antibonding orbitals, respectively. The three  $\sigma$ -orbitals are occupied with six electrons and lie far below the Fermi energy. The three  $\sigma^*$ -orbitals are unoccupied. Just in the same way the two  $p_z$ -orbitals form a  $\pi$ - and a  $\pi^*$ -band filled with two electrons. These behave like nearly free electrons and determine the electronic properties of graphene.

Within the tight binding approach the dispersion relation of graphene can be expressed as

$$E(k_x, k_y) = \pm \gamma_0 \left[ 1 + 4 \cos \left( \frac{\sqrt{3}k_x a}{2} \right) \cos \left( \frac{k_y a}{2} \right) + 4 \cos^2 \left( \frac{k_y a}{2} \right) \right]^{1/2}, \quad (2.4)$$

where  $\gamma_0 \approx 3 \text{ eV}$  is the hopping between neighboring carbon atoms. Plotting equation 2.4 one immediately realizes that the valence and the conduction bands touch at six discrete points, the corner points of the first Brillouin zone, see figure 2.4 (a). The six touching points can be classified into two triplets, each of which groups together points that are equivalent under lattice translations. These two inequivalent groups are usually addressed as  $K$  and  $K'$  points as indicated for instance in figure 2.4 (b). In the undoped case the Fermi energy lies exactly in the middle between valence and conduction band so that the Fermi surface consists only of the six touching points.



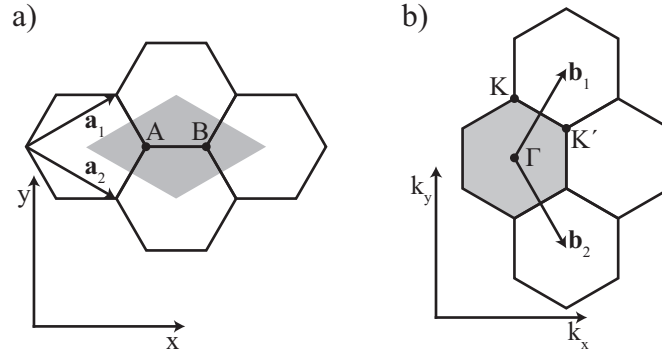


**Figure 2.3.:** (a) Two-dimensional crystal lattice of graphene in real space. Shown are the basis vectors and the primitive unit cell (shaded area). The unit cell contains two atoms, which consequently are not related by lattice translations. This is the reason for the two groups of  $K$  points that result in reciprocal space. (b) The reciprocal lattice of graphene is again a hexagonal lattice as in real space. The basis vectors are denoted  $\vec{b}_1$  and  $\vec{b}_2$ . The first Brillouin zone is indicated by the shaded area.

Next, the aforementioned zone folding is carried out leading to periodic boundary conditions for electrons moving around the circumference and consequently along the chiral vector  $\vec{C}$  of the nanotube. The wave vector associated with movement perpendicular to the tube axis becomes quantized:  $k_{\perp} = \vec{k} \cdot \vec{C} = 2\pi q$ , ( $q = 0, 1, 2, \dots, 2n$ ). The wave vector component along the tube axis, parallel to  $\vec{T}$ , remains continuous, at least as long as the nanotubes are assumed to be infinitely long. The result of this quantization are one dimensional subbands in  $k$ -space as indicated by the white lines in figure 2.4 (b). The orientation of these lines with respect to the reciprocal lattice depends on the chiral angle  $\Theta$ , their length depends on the translation vector  $\vec{T}$  as  $2\pi/T$ . The distance of these discrete lines will later be important for transport properties, as it is the distance of the one dimensional subbands. It is inversely proportional to the diameter  $d$  of the nanotube and given by  $\Delta k = 2/d$ . The interband spacing and the orientation of the subbands are of special interest because they determine whether the nanotube shows metallic or semiconducting behavior. If the discrete lines that indicate the one dimensional subbands cross the  $K$  and  $K'$  points, the nanotube is metallic if not, it is semiconducting.

As has already been mentioned in the beginning of this chapter, both diameter and chiral angle, are closely related to the chiral indices  $(n, m)$  and hence the two classes of nanotubes can be discriminated by their chiral indices. It turns out that armchair nanotubes  $(n, n)$  are always metallic. For zigzag nanotubes  $(n, 0)$  just like for all other chiral tubes it holds true that every third tube is metallic, namely every time  $(2n + m)$  or equally  $(n - m)$  is an integer multiple of three.

For a better understanding of the formation of the one dimensional dispersion relation the two highly symmetric, non chiral cases of armchair and zigzag nanotube will be discussed

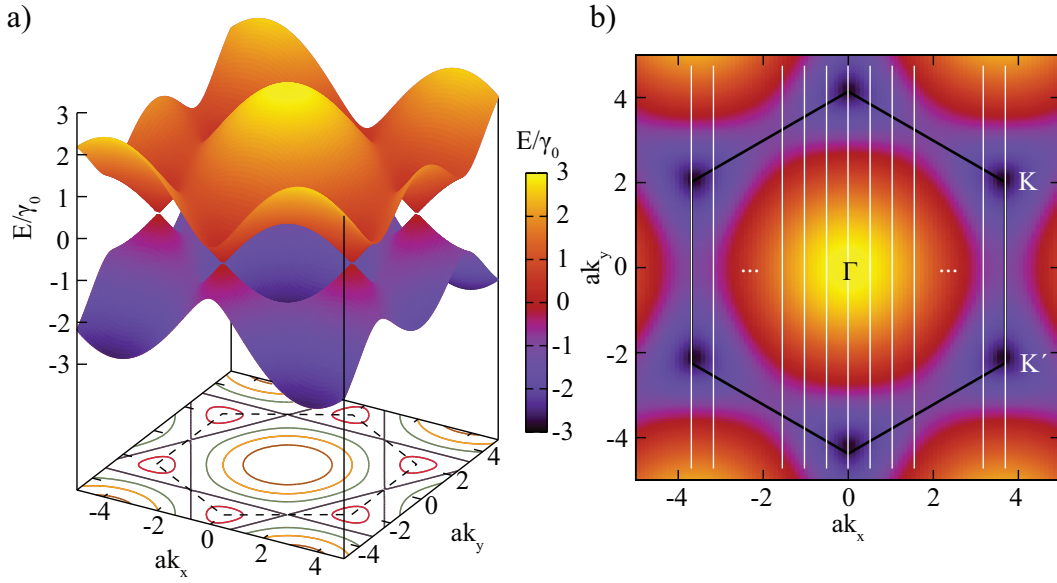


**Figure 2.4.:** (a) Result of tight binding calculations for the band structure of graphene. The valence and conduction bands touch at six discrete points which fall into two physically distinguishable triplets referred to as  $K$  and  $K'$ . In the vicinity of these six points the dispersion relation can be approximated linearly. In the undoped case the Fermi energy lies in the middle between the valence and the conduction band and consequently the Fermi surface consists just of these six points. (b) Color scale plot of the anti-bonding  $\pi^*$ -band of graphene. Imposing periodic boundary conditions for  $k_x$  (once around the circumference) results in discretization of the allowed  $\vec{k}$  points (indicated by the white lines). Only if these white lines touch the  $K$  and  $K'$  points, the tube is metallic. In all other cases it is semiconducting. The white lines are drawn for the case of an armchair nanotube.

in more detail. For armchair nanotubes the length of the chiral vector  $\vec{C}$  is simply  $a$  while for zigzag tubes its length is  $\sqrt{3}a$  where  $a$  again is given by the graphene lattice constant  $a_{CC}$  as  $a = \sqrt{3}a_{CC}$ . In the case of armchair nanotubes the quantization is along the  $k_x$ -direction and reads  $\sqrt{3}nak_x = 2\pi q$  while for zigzag nanotubes the  $k_y$ -direction is getting discretized as  $nak_y = 2\pi q$ . For both cases  $q$  is running from 1 to  $2n$ . Plugging these two quantization conditions into equation 2.4 the energy dispersions for armchair and zigzag nanotubes can be expressed as

$$E_{\text{armchair}}(k_y) = \pm\gamma_0 \left[ 1 \pm 4 \cos\left(\frac{\pi q}{n}\right) \cos\left(\frac{k_y a}{2}\right) + 4 \cos^2\left(\frac{k_y a}{2}\right) \right]^{1/2} \quad (2.5)$$

$$E_{\text{zigzag}}(k_x) = \pm\gamma_0 \left[ 1 \pm 4 \cos\left(\frac{\sqrt{3}k_x a}{2}\right) \cos\left(\frac{\pi q}{n}\right) + 4 \cos^2\left(\frac{\pi q}{n}\right) \right]^{1/2}. \quad (2.6)$$

The one dimensional dispersion relations shown in figure 2.5 are examples created by

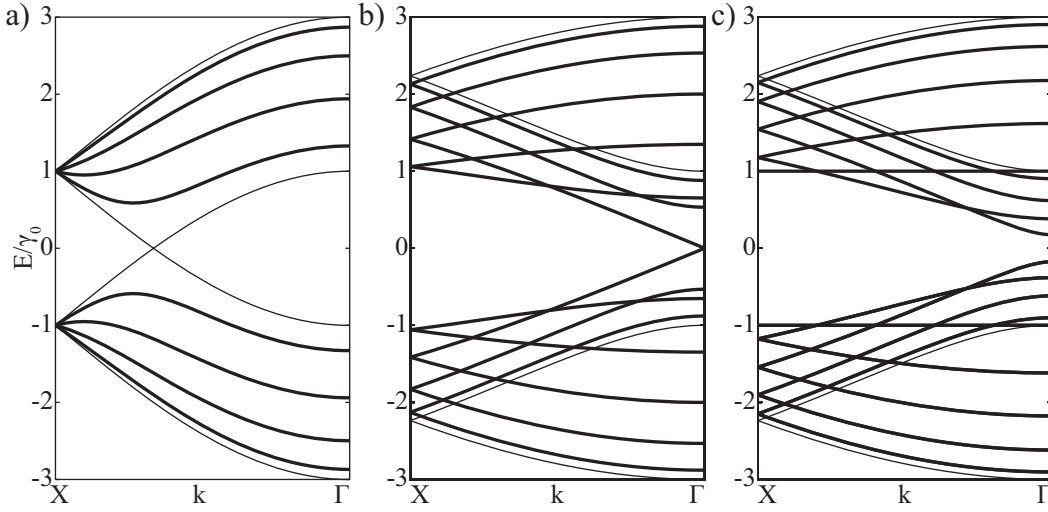


**Figure 2.5.:** One dimensional dispersion relation examples of single wall carbon nanotubes with different chiral indices. Note that the zone boundary or the X point for armchair nanotubes corresponds to  $k = \pm\pi/a$  and for zigzag tubes to  $k = \pm\pi/\sqrt{3}a$ . The slightly thicker lines indicate doubly degenerate levels. (a) Dispersion relation of a (5,5) armchair nanotube. As can be seen, there are two bands crossing two thirds between the  $\Gamma$  and the X point. Armchair nanotubes are always metallic. (b) Example of a metallic zigzag (9,0) nanotube. (c) A (10,0) zigzag tube has a band gap and no states available at the Fermi energy.

plotting equations 2.5 and 2.6 for  $(n,m)$  equal to (5,5), (9,0), and (10,0). In case of an armchair nanotube like for instance (5,5) there are six one dimensional subbands in the conduction band and an equal number in the valence band (see figure 2.5(a)). Four of the six bands are doubly degenerate so that there is a total number of ten levels which is consistent with the ten hexagons around the circumference of a (5,5) nanotube. The valence and the conduction band for the armchair nanotube cross at a  $k$  point two thirds of the distance between  $\Gamma$  and X point. This crossing takes place at the Fermi energy and makes that specific nanotube a zero-gap semiconductor exhibiting metallic conduction at finite temperatures. For zigzag nanotubes,  $(n,0)$ , one has to distinguish between situations in which  $n$  is an integer multiple of three and situations in which this is not the case. Figure 2.5 (b) shows the one dimensional dispersion relations of a (9,0) tube. Also here there is no energy gap and consequently the tube will show metallic conduction. However, for a (10,0) nanotube shown in figure 2.5 (c) a finite energy gap appears and the tube will behave like a semiconductor. The resulting densities of states for the respective tubes are shown in figure 2.6 and have been experimentally observed for instance in Ref. [26].

This overview of the electronic properties of carbon nanotubes is concluded with a short account of additional effects that result from the curvature of nanotubes. These effects are, e.g., different lengths of C-C bonds parallel or perpendicular to the tube axis and a mixing

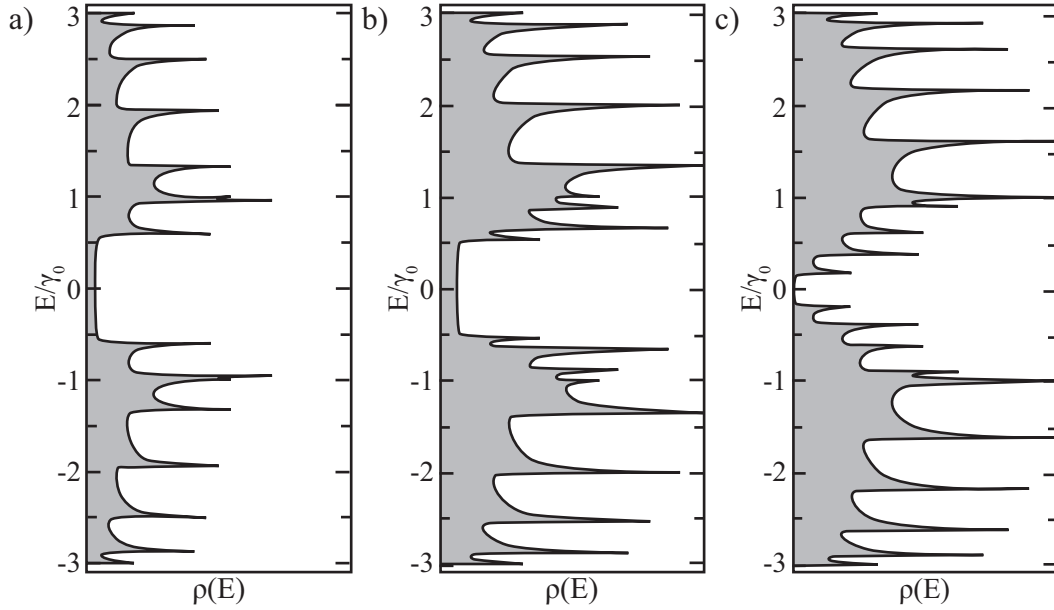


**Figure 2.6.:** Density of states for the same tubes for which the dispersion relations were shown in figure 2.5. These densities can be mapped out for instance by measurements of the differential conductance in scanning tunneling microscopes. (a) Density of states for a (5,5) tube. It can be clearly seen that there is a finite density around zero energy, i.e. the Fermi edge. (b) The same holds for the (9,0) nanotube which also has a finite density of states stemming from the level crossing in figure 2.5(b). (c) A (10,0) nanotube exhibits a finite energy gap and consequently shows semiconducting behavior.

of the  $\pi$ - and  $\sigma$ -states due to the broken planar symmetry. This area is usually referred to as “beyond zone folding” as it is not described by the model given above [61]. One of the curvature induced effects is that the Fermi vector  $k_F$  is shifted away from the corners ( $K$  point) of the Brillouin zone. For non-armchair nanotubes this shift of  $k_F$  opens a small band gap around  $E_F$ . This means that, when the curvature is taken into account, at first only armchair nanotubes remain metallic. Due to symmetry reasons armchair nanotubes preserve their metallic character even with this alteration. The non-armchair nanotubes where the difference between the chiral indices ( $n - m$ ) is an integer multiple of three are then called small band gap nanotubes. In addition to that, the mixing of the  $\pi$ - and  $\sigma$ -states can have the effect that, e.g. a (6,0) nanotube, which is turned into a small band gap nanotube as just described, becomes again metallic, i.e. shows a finite density of states at the Fermi level when this mixing is taken into account [64].

## 3. Electronic transport in mesoscopic structures

### 3.1. Transport regimes

This section briefly reviews some important transport phenomena of mesoscopic physics in general and their occurrence in carbon nanotubes in particular. As a starting point, the differences between classical and quantum transport are shortly reviewed.

For a macroscopic system the resistance  $R$  and conductance  $G$  are simply given by

$$R = \rho \frac{L}{W^2}, \quad (3.1)$$

$$G = \sigma \frac{W^2}{L} = R^{-1}, \quad (3.2)$$

where  $L$  and  $W$  are sample length and width respectively. The resistivity  $\rho$  and its inverse the conductivity  $\sigma$  generally depend on neither sample dimension nor applied fields but are material constants. However, when the size of the conductor becomes small compared to the characteristic length scales for the motion of electrons,  $\rho$  or  $\sigma$  will depend on the sample dimension through quantum effects as, e.g., interference when scattered on the sample boundaries or off a defect or an impurity. The criterion whether a nanotube or a conductor in general appear as a classical or a quantum conductor is set by three length scales. These are the Fermi wavelength  $\lambda_F$ , the momentum relaxation length or simply mean free path  $L_m$ , and the phase relaxation length  $L_\phi$ . The Fermi wavelength  $\lambda_F = 2\pi/k_F$  is the de Broglie wavelength  $\lambda_B = h/mv_F$  for electrons at the Fermi energy  $E_F$ . The phase correlation length  $L_\phi$  is the distance over which an electron can travel before losing its coherence as a wave, i.e. the information about its phase.

Charge carriers behave differently according to how  $L_m$  and  $L_\phi$  compare to the characteristic sample length  $L$ . In the following subsections different situations according to table 3.1 will be discussed. It should be noted that the mentioned length scales are not equally affected by the different scattering mechanisms. Elastic scattering on the one hand does not affect the phase coherence length  $L_\phi$  but only the mean free path  $L_m$ . Inelastic scattering on the other hand limits both, the momentum relaxation length  $L_m$  as well as the phase coherence length  $L_\phi$ . A third type of scattering mechanism comes from electron-electron interactions. This only limits  $L_\phi$  while it has no effect on  $L_m$ . In transport experiments

regime	relationship	coherence length
classical	$L_\phi < L_m \ll L$	$\sim L_m$
localized	$L_m \ll L_\phi < L$	many $L_m$ 's
weakly	$L_\phi < L_c$	$L_\phi$
strongly	$L_\phi > L_c$	$L_c$
ballistic	$L_m > L_\phi > L$	$L$

**Table 3.1.:** Summary of the different transport regimes in mesoscopic physics. The case of diffusive transport is represented by the two situations of weak and strong localization. The second column describes the conditions for the respective regime. In the last column the resulting length scale over which coherence effects can be observed is listed.  $L_c$  is called the localization length (see subsection 3.1.3). Adapted from [63].

only the electrons at the Fermi energy contribute and hence the Fermi wavelength  $\lambda_F$  or more directly the Fermi velocity (in carbon nanotubes  $v_F \sim 8.1 \times 10^5 \text{ m s}^{-1}$ ) connects the length scales to time scales - in particular the momentum relaxation time  $t_m = L_m/v_F$  and the phase relaxation time  $t_\phi = L_\phi/v_F$ . The relation between the aforementioned length scales determines one of three transport regimes: ballistic, diffusive, or classical transport.

### 3.1.1. Ballistic transport

$L \ll L_m, L_\phi$  — Ballistic transport manifests as single electron conduction without momentum or phase relaxation. In this regime the electron wave function is the solution of Schrödinger's equation. In carbon nanotubes the structural quality, depending on the control over the fabrication process, can be sufficiently high to observe ballistic transport. In the case of highly transparent contacts and defectless tubes the one-dimensional subbands [cf. figure 2.5] form conduction channels in the sense of the Landauer-Büttiker formalism [65]. In case of spin-degenerate channels each channel contributes  $G_0 = 2e^2/h$  to the conductance. Adding the additional orbital or angular momentum degeneracy corresponding to the  $K$  and  $K'$  points, the overall theoretical conductance of a single nanotube is given by

$$G = 2G_0 = 4e^2/h = (6.4 \text{ k}\Omega)^{-1}. \quad (3.3)$$

In a realistic experimental situation non ideal contacts and lattice irregularities of the carbon nanotube limit the conductance typically to  $G \approx 3e^2/h$ . The reality of ballistic transport has been shown for instance by Liang et al. [29] where electron coherence has been demonstrated by Fabry-Perot interference of multiply reflected electrons in a single wall carbon nanotube [see figure 3.1(a)].

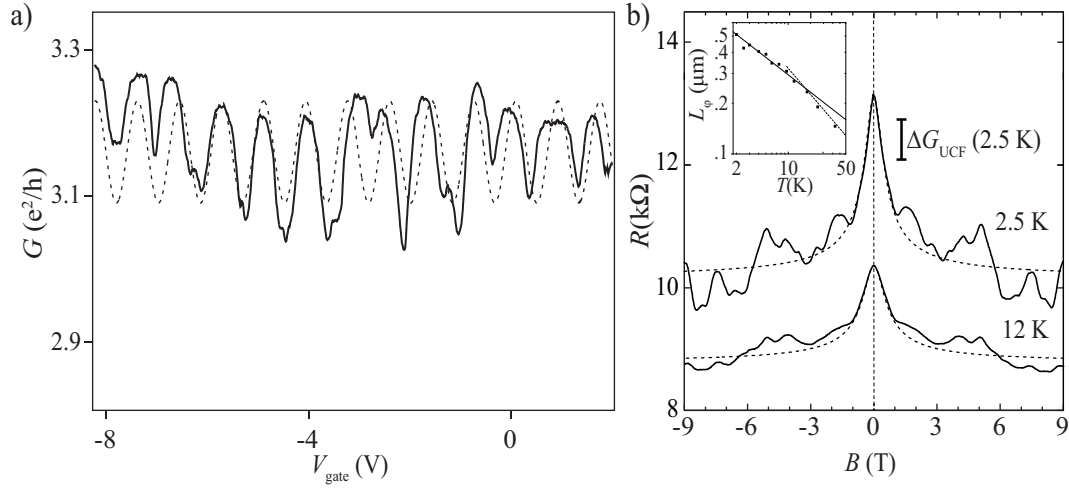


**Figure 3.1.:** (a) Measurement by Liang et al. [29] of a multi wall carbon nanotube demonstrating ballistic transport. The oscillatory conductance stems from the constructive and destructive Fabry-Perot interference of frequently reflected electron wave functions in the carbon nanotube “cavity”. As the electron wave vector is influenced by the gate voltage, the oscillations depend on  $V_{\text{gate}}$ . (b) Measurement by Schönenberger et al. [66] showing diffusive transport phenomena in multi wall carbon nanotubes. The central peak of the resistance versus magnetic field can be explained by weak localization, while the aperiodic fluctuations clearly visible for the lower temperature are attributed to universal conductance fluctuations (see text). The insert shows the determination of the phase coherence length  $L_\phi$ .

### 3.1.2. Classical transport

$L_\phi \ll L_m \ll L$  — In this regime momentum and phase relaxation events occur so frequently that the electron can be viewed as a particle. Since the phase is not preserved over a length  $L$ , Schrödinger’s equation cannot be solved for the entire sample. In this case the total resistance is given by a series connection of microscopic resistances for every momentum relaxation length  $L_m$ , and summing up all resistances results in Ohm’s law as expected for a classical conductor.

### 3.1.3. Diffusive transport and localization

$L_m \ll L_\phi < L$  — When transport through a conductor occurs in the diffusive regime many elastic scattering events take place. Since elastic scattering events only affect the mean free path and not the phase coherence length,  $L_\phi$  can become much longer than  $L_m$ . The wave function is said to be localized. One can distinguish between two different cases of localization which will be described in the following.



Both localization regimes have in common that the phase coherence length  $L_\phi$  has to be larger than the mean free path  $L_m$ . An additional length scale to discriminate the localization regimes is provided by the localization length  $L_c = ML_m$  where  $M$  denotes the number of channels. The localization length  $L_c$  describes the average spatial extent of quantum mechanical states. For a perfectly periodic lattice, the Bloch states are spread out infinitely ( $L_c = \infty$ ). Defects or disorder may lead to a restriction of the spatial extent giving rise to a finite value of the localization length [67].

For the case that the phase coherence length  $L_\phi$  is much larger than the localization length the sample is in the strong localization regime. This localization is the effect of a random potential, generated, e.g., by defects, on the wave function and is called Anderson localization. If, on the other hand, the phase coherence length is smaller than the localization length the predominant transport regime is called weak localization. There are two important consequences of weak localization that are regularly observed in experimental situations and hence justify a closer look.

### Universal conductance fluctuations

When the phase coherence length  $L_\phi$  is comparable to or larger than the sample length  $L$ , interference effects from a superposition of all transmission channels become important [see figure 3.1 (b)]. The interference contribution originates in the random phases of different paths and varies as a function of magnetic field or Fermi wave vector. These fluctuations, although random, do not average out but produce a universal contribution to the conductance of magnitude  $G \approx e^2/h$ . If, on the other hand, the phase coherence length is smaller than the sample size, the fluctuations in the consecutive segments of length  $L_\phi$  sum up independently and the relative size of the fluctuations is suppressed.

### Negative magnetoresistance at $B = 0$

Negative magnetoresistance is another effect that is observable in the presence of weak localization and describes the fact that the resistance of a sample is decreasing when a magnetic field is applied [see figure 3.1 (b)]. It is closely related to the Aharonov-Bohm effect as will become clear from the following description. Consider the special case of an electron path that forms a closed loop. An electron can travel along this path either in a clockwise or a counter clockwise, time-reversed, direction. If the length of path does not exceed the phase coherence length, the two processes of clockwise and counter clockwise propagation are coherent. This coherence results in *enhanced backscattering*. The vector potential of a magnetic field influences the phases of the wave functions of the time-reversed paths differently and consequently destroys phase coherence. This in turn increases the conductance because backscattering is suppressed.

### Electron-electron interaction

While in macroscopic conductors effects of electron-electron interactions (EEI) are usually very weak because the long range part of the Coulomb interaction is only appearing as an exponentially screened interaction potential, in conductors of reduced dimensions this screening is less effective. This results in an anomaly in the density of single particle states near the Fermi energy. For strictly one dimensional systems as, e.g., single wall carbon nanotubes, the Fermi liquid theory is predicted to break down completely. Instead, the system is in a state whose lowest energy excitations are plasma oscillations with a bosonic character. This new state is referred to as Tomonaga-Luttinger liquid. Although its most prominent prediction, spin-charge separation, is very intriguing, it will not be covered in more detail within this work.

A much more frequently observed implication of electron-electron interactions, Coulomb blockade (CB), takes place under certain conditions in conductive islands connected to metallic leads by tunnel junctions [cf. figure 3.2 (a)]. This structure is called a quantum dot and due to its great importance for the study of transport phenomena will be described in greater detail in the following section.

## 3.2. Quantum dots and Coulomb blockade

A quantum dot in general is a conductive island of nanoscale proportions in an otherwise non-conductive environment [see figure 3.2]. For the measurement of transport properties a source and a drain electrode are connected via tunnel junctions. In addition, the potential of the quantum dot can be adjusted by a capacitively coupled gate electrode. This clustering of atoms can in principle be almost anything from a molecule, to a small grain or metallic island, or an electrostatically defined patch of a 2DEG. Despite the variety of systems that exist, the transport properties of a quantum dot are quite generic. These transport properties are summarized in this section which follows closely the reviews by Kouwenhoven et al. [68–70]. Additionally, several other sources as e.g. [71] are used. Groundbreaking articles in this field were Refs. [72–76]. For the first two subsections the discussion is restricted to the linear response regime, i.e.  $V_{sd} \simeq 0$  or  $\mu_s \simeq \mu_d$ .

### 3.2.1. Classical Coulomb Blockade (continuous level spectrum)

In a model assuming a metallic capacitor, the number of charges on the quantum dot can only change by one if the charging energy  $U = e^2/C_\Sigma$  is supplied to overcome the repulsion of the remaining electrons already residing on the dot. In the expression for the charging energy the capacitance of source and drain as well as for the gate electrode are summed with any other residual capacitance into  $C_\Sigma$ . If the thermal energy of the

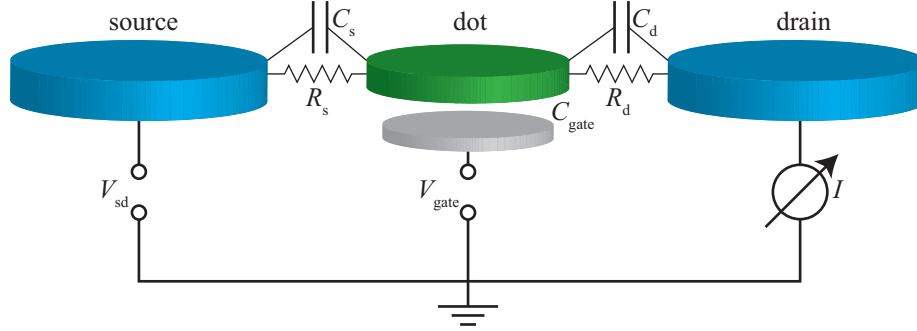


**Figure 3.2.:** Schematic of a quantum dot (QD) in transport experiments. Source and drain contacts are tunnel coupled to the conductive island. The coupling can be parametrized by a capacitance  $C_{s,d}$  and a tunneling resistance  $R_{s,d}$ . The connection scheme for transport measurements is indicated. The current  $I$  through the device is measured depending on the voltage  $V_{sd}$  between source and drain and the gate voltage  $V_{gate}$  applied across a capacitance  $C_{gate}$ .

electrons due to a finite temperature is much smaller than the charging energy, the number of charges can not fluctuate due to thermal excitations either. This gives the first condition for a fixed charge number and can be summarized as

$$\frac{e^2}{C_\Sigma} \gg k_B T. \quad (3.4)$$

The second condition arises from the fact that the number of charges during the time scale of a typical measurement should be well defined. In order for this to be valid, the tunneling resistance  $R_t = R_{s,d}$  from the island to source or drain contacts has to be sufficiently high. With a typical time  $\Delta t = R_t C_{s,d}$  for charging or discharging the island, the Heisenberg uncertainty relation  $\Delta E \Delta t = U \Delta t = (e^2/C_\Sigma) R_t C_{s,d}$  implies that the tunneling resistance has to be bigger than the quantum of resistance

$$R_t \gg \frac{h}{e^2} = 25.813 \text{ k}\Omega. \quad (3.5)$$

The condition of equation 3.4 can be met by a combination of millikelvin temperatures and small structures (recall that the capacitance of, e.g., a sphere,  $C = 4\pi\epsilon_r\epsilon_0 R$ , a flat disc,  $C = 8\epsilon_r\epsilon_0 R$ , or a cylinder over a flat plane  $C = 2\pi\epsilon l / \text{arcosh}(d/R)$  all scale with the radius). The inequality expressed in equation 3.5 on the other hand means that the contact between electrodes and island has to be sufficiently opaque, providing the mentioned requirement of tunnel barriers.

If both conditions are met, a phenomenon called Coulomb blockade (CB) can be observed which essentially means that charge transfer through the nanostructure is blocked due to

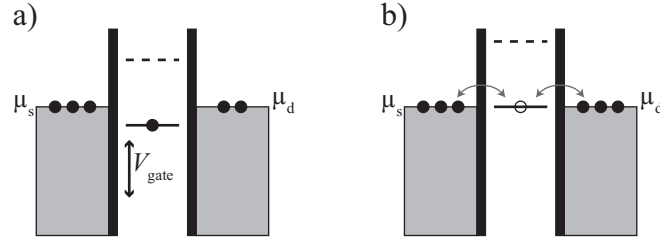


**Figure 3.3.:** Energy diagram for the process of single electron tunneling through a quantum dot. (a) The chemical potential of the quantum dot lies below those of the leads. No current can flow due to Coulomb blockade. The potential of the dot can be adjusted by a capacitively coupled gate voltage  $V_{\text{gate}}$ . (b) The condition for charge fluctuation is fulfilled and the quantum dot changes its behavior from Coulomb blockade to single electron tunneling.

Coulomb repulsion between the electrons on the dot and those in the leads. The first observations of this phenomenon were made on metallic islands [77]. The high density of states in metals has the effect that many states contribute to the tunneling event. The probability for  $N$  charges on the quantum dot can be derived from the grand canonical potential as

$$P(N) = \frac{1}{Z} \exp \left( -\frac{\Omega(N)}{k_B T} \right), \quad (3.6)$$

where the grand canonical potential is given by  $\Omega(N) = F(N) - \mu N$ . Here  $\mu$  is the chemical potential of the surrounding reservoirs,  $Z$  is the partition function, and  $F(N) = E(N) - ST$  the free energy. At sufficiently low temperatures the free energy can be approximated by the ground state energy  $E(N)$  of the quantum dot.

In order for current being able to flow through the quantum dot, the charge number on the dot has to fluctuate at least by one which means that the probability for  $N$  and  $N+1$  charge carriers have to be equal. The condition  $P(N) = P(N+1)$  at low temperatures simplifies to

$$E(N) - E(N+1) = \mu, \quad (3.7)$$

where  $E(N)$  is the total ground state energy for  $N$  electrons on the island at zero temperature. That means that the chemical potential of the leads has to be as large as the *difference* between the ground state energies with  $N$  and  $N+1$  particles, in order to allow for the transition between the states with these particle numbers.

It is common to define the difference between the two ground state energies given in equation 3.7 as the chemical potential

$$\mu_{\text{dot}}(N) \equiv E(N) - E(N+1) \quad (3.8)$$

of the quantum dot with  $N$  charge carriers. This allows to formulate the condition for single electron tunneling simply as  $\mu_{\text{dot}} = \mu$ . This condition is illustrated in figure 3.3. If

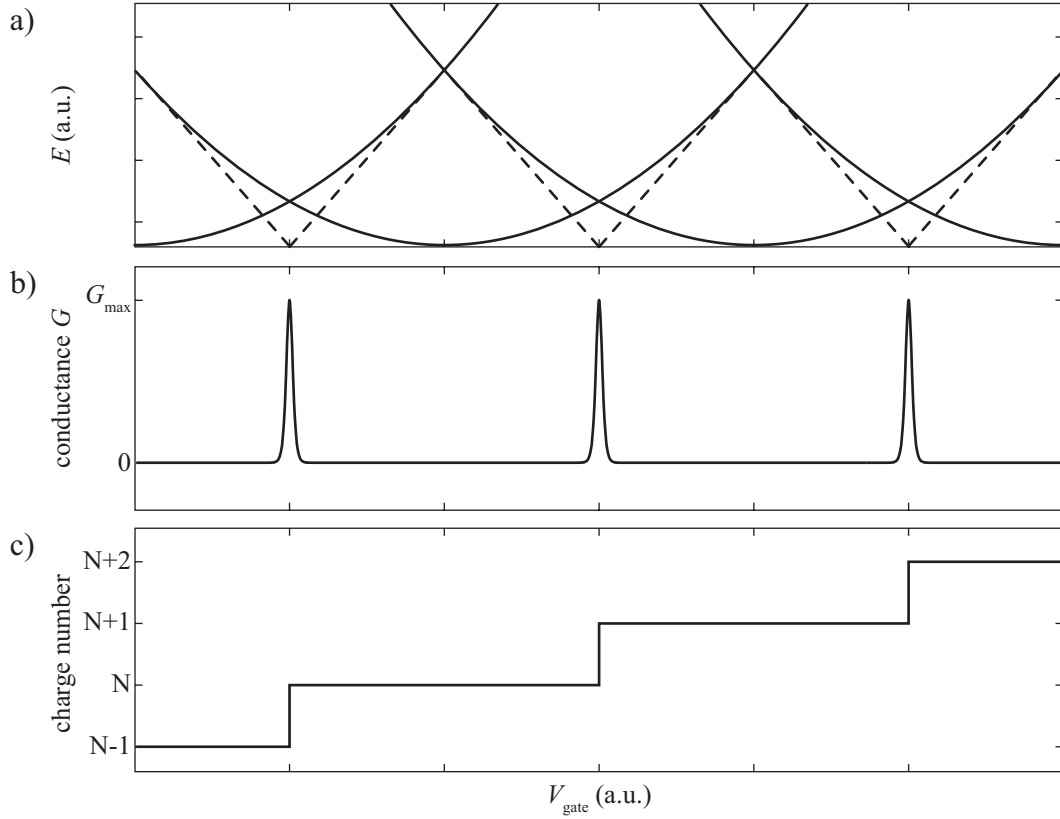


**Figure 3.4.:** Schematic of the interrelations between the involved quantities of classical Coulomb blockade and their dependence on the gate voltage  $V_{\text{gate}}$ . (a) Electrostatic energy of the quantum dot (solid lines) and difference of the electrostatic energies for adjacent charge numbers (dashed lines). (b) Differential conductance through the quantum dot in the linear regime and at  $T \simeq 0$ . (c) Charge number on the quantum dot.

the chemical potential of the dot is below the chemical potential of the leads as shown in figure 3.3(a) no current can flow and the quantum dot is said to be in Coulomb blockade. In figure 3.3(b) the chemical potential of the dot is aligned with the chemical potential of the leads and the charge number on the dot can fluctuate by one, i.e. current can flow.

For a metallic island where the quantization of the states can be neglected due to the quasi constant density of states in the metal, the energy  $E(N)$  can be approximated by the classical charging energy for a capacitor

$$E(N) \simeq \frac{1}{2C_{\Sigma}}(eN + C_{\text{gate}}V_{\text{gate}})^2, \quad (3.9)$$

where  $C_{\Sigma}$  is again the sum of all capacitances of the system

$$C_{\Sigma} = C_s + C_d + C_{\text{gate}} + C_{\text{rest}}. \quad (3.10)$$

(a) $\Delta\epsilon \lesssim e^2/C_\Sigma \ll k_B T$	no discreteness of charge due to: · temperature too high · or quantum dot not small enough · or tunneling resistance too low
(b) $\Delta\epsilon \ll k_B T \ll e^2/C_\Sigma$	classical or metallic Coulomb blockade regime · many levels contribute to tunneling · many levels excited by thermal fluctuations
(c) $k_B T \ll \Delta\epsilon < e^2/C_\Sigma$ $\hbar\Gamma \ll k_B T$	quantum Coulomb blockade regime · only one or a few levels participate in transport · width of conductance peaks set by <i>temperature</i>
(d) $k_B T \ll \hbar\Gamma \ll \Delta\epsilon$	quantum Coulomb blockade regime · only one or a few levels participate in transport · width of conductance peaks set by <i>life time</i>

**Table 3.2.:** Transport regimes for single electron tunneling.

With this expression for the ground state energy and equation 3.7 the condition for single electron tunneling can be written as

$$\mu = e\alpha_{\text{gate}}V_{\text{gate}} + \frac{e^2}{C_\Sigma} \left(N + \frac{1}{2}\right) = e\alpha_{\text{gate}}V_{\text{gate}} + U \left(N + \frac{1}{2}\right). \quad (3.11)$$

Here the ratio between the gate capacitance and the total capacitance was shortened into the so-called gate conversion factor  $\alpha_g$ , i.e.

$$\alpha_{\text{gate}} \equiv \frac{C_{\text{gate}}}{C_\Sigma}. \quad (3.12)$$

Since the potential of the QD can be changed by the gate voltage, Coulomb blockade can be removed by aligning the chemical potential for the next additional charge  $\mu_{\text{dot}}(N+1)$  at the chemical potential of the leads. With equation 3.11 and assuming that  $\alpha_{\text{gate}}$  is constant for different particle numbers on the dot, the distance in terms of gate voltage between two Coulomb oscillations is given by

$$\Delta V_{\text{gate}} = \frac{e}{\alpha_{\text{gate}}C_\Sigma} = \frac{e}{C_{\text{gate}}}, \quad (3.13)$$

i.e. the oscillations are equidistant. The above discussed properties of the QD and the gate voltage are depicted in figure 3.4. In panel (a) the electrostatic energy as given in equation 3.9 is plotted against the gate voltage. The quadratic dependence on  $V_{\text{gate}}$  results in the parabolas. The energy difference between states separated by one charge is indicated

by the dashed lines. At the points where two neighboring parabolas intersect, the energies  $E(N)$  and  $E(N+1)$  are degenerate. This means that current can flow which is reflected by the peaks in the conductance in panel (b) at exactly those positions. In panel (c) finally the average charge number of the quantum dot is plotted. Every time a conductance maximum is passed, the charge number changes by  $\Delta N = 1$ .

### 3.2.2. Quantum Coulomb blockade

So far only the case of a metallic quantum dot with a continuous density of states has been discussed. If the quantum dot however is fabricated for instance within a semiconductor heterostructure where the Fermi wavelength can be easily on the order of 100 nm and thus on the scale of the device itself, the energy spectrum will be discrete. If the spacing of the discrete states is bigger than the thermal energy ( $\Delta\epsilon \gg k_B T$ ) it is observed in experiments. The value of  $\Delta\epsilon$  at the Fermi energy  $E_F$  depends on the dimensionality  $D$  of the system. For a particle in a box of size  $L$ , including spin degeneracy, one obtains for instance

$$\Delta\epsilon = \frac{N \hbar^2 \pi^2}{4 m L^2} \quad (1D)$$

$$= \frac{1 \hbar^2 \pi^2}{\pi m L^2} \quad (2D)$$

$$= \left( \frac{1}{3\pi^2 N} \right)^{1/3} \frac{\hbar^2 \pi^2}{m L^2}. \quad (3D)$$

Typically, in semiconductor quantum dots the spacing of the discrete states for structure sizes of around 100 nm is in the range of 0.1 meV to several meV. Compared to the thermal energy at typical cryogenic temperatures  $k_B \cdot 100 \text{ mK} \sim 10 \mu\text{eV}$ , it is clear that  $\Delta\epsilon$  plays a role in the spectrum of quantum dots in this situation.

In order to describe the implications of a discrete level structure an account of the typical transport regimes is given here starting with the purely classical case of an Ohmic conductor. At thermal energies that are even larger than the classical charging energy of the metallic island it behaves like a regular conductor. By subsequently lowering the thermal energy with respect to the other energy scales like the charging energy  $U = e^2/C_\Sigma$ , the level spacing  $\Delta\epsilon$ , or the tunnel coupling  $\hbar\Gamma$  the basic transport mechanism changes. These different transport regimes together with the relation of the involved energy scales are summarized in table 3.2.

In the high temperature limit  $e^2/C_\Sigma \ll k_B T$  [(a) in table 3.2] the conductance is independent of the electron number. Its inverse, corresponding to the resistance, is given by the sum of the inverse barrier conductances  $1/G = 1/G_\infty = 1/G_S + 1/G_D$ . Note that the high temperature conductance  $G_\infty$  is completely independent of the size of the dot and that it is entirely characterized by the two barriers.

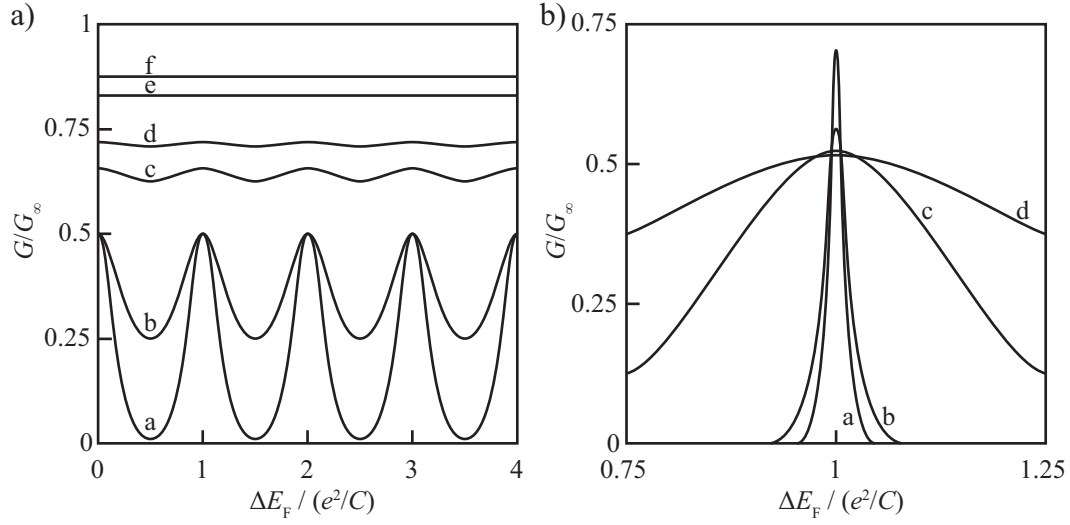


**Figure 3.5.:** Plots of the calculated temperature dependence of Coulomb oscillations as a function of the Fermi energy in the classical regime (a) and the quantum regime (b) both in the situation where the linewidth is set by thermal activation. In (a) the parameters for the calculation were  $\Delta\epsilon = 0.01e^2/C_\Sigma$  and  $k_B T/(e^2/C_\Sigma) = 0.075$  [a], 0.15 [b], 0.3 [c], 0.4 [d], 1 [e], and 2 [f]. In (b) the parameters were  $\Delta\epsilon = 0.01e^2/C$  and  $k_B T/\Delta\epsilon = 0.5$  [a], 1 [b], 7.5 [c], and 15 [d]. Reproduced from [80]

The classical Coulomb blockade [(b) table 3.2] can be described by the so-called “orthodox” Coulomb blockade theory [75, 78–80]. In figure 3.5(a) Coulomb oscillations for the classical case were calculated following [80] for energy independent tunneling rates  $\Gamma_s$  and  $\Gamma_d$  as well as an energy independent density of states  $D$  in the leads. The line shape of an individual Coulomb peak in this regime is given by

$$G = G_{\max} \frac{\delta/k_B T}{2 \sinh(\delta/k_B T)} \approx \frac{1}{2} \cosh^{-2} \left( \frac{\delta}{2.5 k_B T} \right) \quad \text{for } \hbar\Gamma \ll k_B T \ll e^2/C_\Sigma \quad (3.14)$$

with

$$G_{\max} = \frac{e^2 D}{2} \frac{\Gamma_s \Gamma_d}{\Gamma_s + \Gamma_d}. \quad (3.15)$$

Here  $\delta$  is related to gate voltage by  $\delta = e\alpha_{\text{gate}}|V_{\text{gate, res}} - V_{\text{gate}}|$ , where  $V_{\text{gate, res}}$  is the gate voltage at the peak center. Effectively,  $\delta$  denotes the distance from the position of the resonance maximum. For  $k_B T \ll e^2/C_\Sigma$  the peak width decreases linearly with temperature and the peak height  $G_{\max}$  is independent of temperature (cf. curves a and b in figure 3.5). The value of  $G_{\max}$  is equal to half of the high temperature value  $G_{\max} = G_\infty/2$ . This is because when Coulomb blockade becomes effective an electron first has to tunnel off the island before a second one can enter it. So the tunneling probability decreases by a factor of 2.



In the quantum Coulomb blockade regime [(c) and (d) in table 3.2] tunneling occurs through a single quantum level. Depending on the relation between the charging energy  $e^2/C_\Sigma$  and the level spacing  $\Delta\epsilon$  nearly equidistant or aperiodic Coulomb oscillations are observed. The temperature dependence of the Coulomb peaks was derived in [75] as

$$G = G_{\max} \cosh^{-2} \left( \frac{\delta}{2k_B T} \right), \quad \text{for } \hbar\Gamma \ll k_B T \ll \Delta\epsilon, e^2/C_\Sigma \quad (3.16)$$

with

$$G_{\max} = \frac{e^2}{4k_B T} \frac{\Gamma_s \Gamma_d}{\Gamma_s + \Gamma_d}. \quad (3.17)$$

One can see that the line shape of the classical and the quantum case are practically the same. It is the peak height where the main distinction can be found. While the peak height was constant in the classical case, it is inversely proportional to the temperature in the quantum case.

For the last case [(d) in table 3.2], the assumption  $\hbar\Gamma \ll k_B T$  is dropped. This means that the barrier conductances are now becoming important. At sufficiently low temperatures, the coupling  $\hbar\Gamma$  can be substantially larger than the thermal energy  $k_B T$ . This results in charge fluctuations between the quantum dot and the contacts which corresponds to a finite life time of the state with, e.g.,  $N$  electrons. By the Heisenberg principle a finite life time corresponds to an energy uncertainty which means that the state will be smeared out. In this situation the line shape is given by the Breit-Wigner formula for the conductance as

$$G = G_{\max} \frac{(\Gamma/2)^2}{(\Gamma/2)^2 + (e\alpha_{\text{gate}}(V_{\text{gate}} - V_{\text{gate,res}}))^2}. \quad (3.18)$$

The maximum conductance is given by

$$G_{\max} = \mathcal{G} \frac{e^2}{h} \frac{\Gamma_s \Gamma_d}{\Gamma_s + \Gamma_d} \frac{4}{\Gamma} \quad (3.19)$$

where  $\mathcal{G}$  denotes the degree of degeneracy of the electronic states participating in the tunneling process. The tunneling rates to source and drain contacts are given by  $\Gamma_s$  and  $\Gamma_d$ , respectively. The rate  $\Gamma \geq \Gamma_s + \Gamma_d$  corresponds to the total life time broadening.

For the case that tunneling occurs only through a single quantum level calculating  $E(N)$  for a quantum dot with discrete levels is not straight forward and usually several assumptions to simplify the problem are made and summarized under the name “constant interaction model”. These are

- that the quantum levels on the dot can be calculated independent of the total number of electrons on the dot,
- that the Coulomb interactions among the electrons on the dot and the interactions between electrons on the dot and those in the leads or the metallic gates can be parametrized by a single parameter, the capacitance  $C_\Sigma$ , and

- that this total capacitance  $C_\Sigma$  is independent of the total number of electrons on the dot.

### 3.2.3. Non-linear transport

So far the only energy supplied to the quantum dot came from charging the gate electrode. In addition to measuring the linear response Coulomb oscillations at negligible bias voltage, further information about the relevant energy scales of the quantum dot can be gathered by measuring the non-linear dependence of the current on the bias voltage  $V_{sd}$ .

A guide is that the current depends on the number of available states within the bias window given by  $eV_{sd} = \mu_s - \mu_d$ . For the details of non-linear transport it is again helpful, like in the previous section, to distinguish between the classical and the quantum case.

In the classical regime the current is zero as long as the chemical potential of the quantum dot does not lie within the interval between  $\mu_s$  and  $\mu_d$  [compare figure 3.3]. Current will flow as soon as either  $\mu_s > \mu_{dot}(N+1)$  or  $\mu_d < \mu_{dot}(N)$ , depending on how the voltage drops across the two barriers. These two cases correspond to either the transition  $N \leftrightarrow (N+1)$  or  $(N-1) \leftrightarrow N$ , respectively. If  $V_{sd}$  is increased even further a second charge state can enter the bias window leading to yet another increase in current. This stepwise increase of the current is known as the *Coulomb staircase*. The width of each step is given by the classical charging energy  $e^2/C_\Sigma$ .

The real correspondence to spectroscopy becomes obvious only in the quantum regime. Here discrete levels as well as excitations of these levels can be made visible by tunneling experiments. Increasing  $V_{sd}$  leads to two different types of changes in the tunneling current. One corresponds to the change in the number of accessible charge states just as in the classical case. The second one, though, corresponds to changes in the number of quantum states that electrons can occupy while on the dot. According to their origin, the voltage difference between current steps of the first type is called *addition energy* while the voltage difference for current changes of the second type is called *excitation energy*.

Figure 3.6 shows the typical pattern that results when the current is measured versus bias and gate voltage and color coded in a two dimensional map. The white diamonds in figure 3.6 mark the combinations of bias and gate voltage where no current can flow due to Coulomb blockade; these are also called Coulomb (blockade) diamonds. Along the zero bias line the touching points of the diamonds are the degeneracy points where the charge state of the quantum dot is aligned with both chemical potentials of the leads. A trace at zero bias along the gate voltage reproduces the Coulomb oscillations that were shown already for instance in figure 3.4(b).

Consider a fixed gate voltage in the regime where current is blocked. Increasing the source drain voltage at one point will bring a charge state into the bias window. At this point

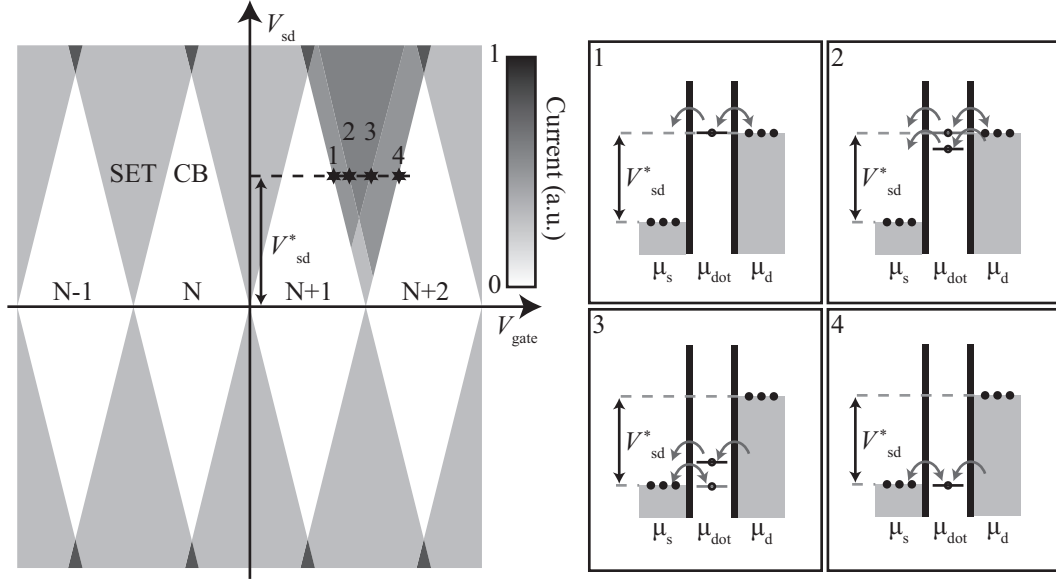


**Figure 3.6.:** Non-linear transport spectroscopy: the left panel shows a schematic of what is commonly called a charging or a stability diagram. Such a measurement records the color coded size of the current at different combinations of gate and bias voltage,  $I(V_{\text{sd}}, V_{\text{gate}})$ . The areas where current is blocked due to Coulomb blockade (CB) form white diamond shaped areas. The diamonds touch at zero bias voltage at the degeneracy points where the chemical potential of the dot is in resonance with the chemical potentials of the leads. The lightest grey areas map the region where exactly one charge state is within the bias window and current is given by single electron tunneling (SET). At the transition  $(N+1) \leftrightarrow (N+2)$  the right panel visualizes the potential landscape at four distinct points that are also marked on the two dimensional plot on the left. The source-drain voltage  $V_{\text{sd}}^*$  for all four points is the same. Transport on the boundary lines of the diamonds is due to the dot level being in resonance with the chemical potential of either source or drain. The additional lines that are shown exemplarily in one case come from charge transfer through excited states as also depicted on the right side.

single electron tunneling can occur. In addition to the ground state energies of the  $N$  and  $N+1$  charge states, there will also be excited states due to size quantizations analogous to a particle in a box. The excited states offer additional charge transfer channels that usually increase the tunneling probability, leading to an increase of current. This is indicated in figure 3.6 by the different shades of grey in one of the SET regimes. For a more detailed quantitative analysis one defines conversion factors for source ( $\alpha_s$ ) and drain ( $\alpha_d$ ) contacts

$$\alpha_s \equiv \frac{C_s}{C_\Sigma} \quad \alpha_d \equiv \frac{C_d}{C_\Sigma} \quad (3.20)$$

in analogy to the gate conversion factor  $\alpha_{\text{gate}}$  with the capacitances between the quantum dot and source and drain contacts,  $C_s$  and  $C_d$  respectively.

Assuming the drain potential is constant ( $\mu_d = \text{const.}$ ) and considering the SET line through point 1 in figure 3.6, the chemical potential of the quantum dot can be written as

$$\mu_{\text{dot}} = \mu_d = E_N + \left(N + \frac{1}{2}\right) \frac{e^2}{C_\Sigma} + e(\alpha_s V_{\text{sd}} + \alpha_{\text{gate}} V_{\text{gate}}) = \text{const.} \quad (3.21)$$

Equally, the condition for the SET line through point 4 in figure 3.6 can be written as

$$\mu_{\text{dot}} = \mu_s = E_N + \left(N + \frac{1}{2}\right) \frac{e^2}{C_\Sigma} + e((\alpha_s - 1)V_{\text{sd}} + \alpha_{\text{gate}} V_{\text{gate}}) = \text{const.} \quad (3.22)$$

With these two equations one can determine the slopes of the lines that define the Coulomb diamond as

$$\lambda_s \equiv \frac{dV_{\text{gate}}}{dV_{\text{sd}}} = \frac{1 - \alpha_s}{\alpha_{\text{gate}}} = \frac{C_\Sigma - C_s}{C_{\text{gate}}} \quad (3.23)$$

$$\lambda_d \equiv \frac{dV_{\text{gate}}}{dV_{\text{sd}}} = -\frac{\alpha_s}{\alpha_{\text{gate}}} = -\frac{C_s}{C_{\text{gate}}}. \quad (3.24)$$

These slopes allow to determine the gate conversion factor  $\alpha_{\text{gate}}$  as

$$\alpha_{\text{gate}} = \frac{1}{|\lambda_d| + |\lambda_s|}. \quad (3.25)$$

### 3.2.4. Quantum dots in carbon nanotubes

After the general description of quantum dots in the previous sections, the focus of the present part is set on quantum dots formed in carbon nanotubes following [76] and [81]. Especially the different transport regimes depending on the transparency of the tube-contact interface will be reviewed. These will allow to divide devices into classes showing almost exclusively certain transport properties. Unfortunately in carbon nanotube quantum dots it is not as easy to vary the transparency as in split-gate defined heterostructure quantum dots. In CNT quantum dots usually the relation between the work function of the contact material and the nanotube sets the transparency. The transparency however is not fully set by the choice of material. Since the electrostatic potential of the quantum dot can be tuned by a gate voltage the actual transparency can vary with  $V_{\text{gate}}$ . This is again especially obvious in semiconducting tubes where the tunnel barrier for hole transport can be much smaller than for electron transport. Consequently, semiconducting tubes often show different transport behavior on either side of the gap [31, 82].

Starting at the lowest transparency or the highest interface resistance, carbon nanotube quantum dots are in the so-called closed regime. This means that electrons will tunnel

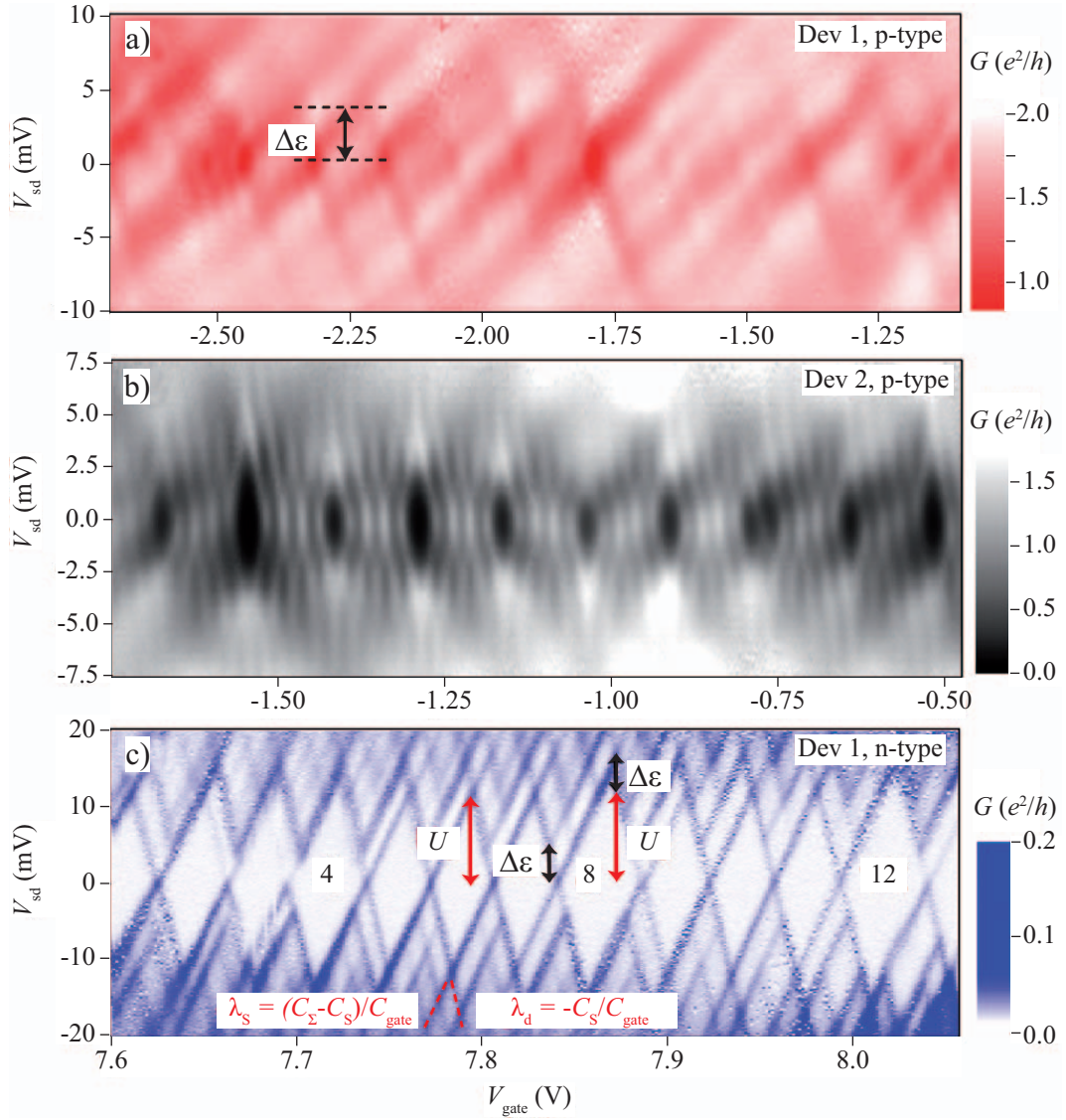


**Figure 3.7.:** Stability diagrams of the conductance for different transport regimes, taken from [31]. (a) For highly transmissive contacts the carbon nanotube acts as a waveguide and displays interference effects. This Fabry-Perot interference pattern allows to read off the cavity length from the characteristic period  $\Delta\epsilon$ . Note that the conductance in this regime can reach the maximum of conductance of  $4e^2/h$ . (b) For intermediate coupling between the contacts and the carbon nanotube the transport is influenced by higher order processes such as the Kondo effect. (c) Low transparency of the contact interfaces leads to single charge tunneling and Coulomb blockade. In this example, several excited states can be observed (see text and figure 3.8 for details).

one by one and the system is often called a single electron transistor (SET). This has been already extensively discussed in the previous sections.

When intermediate transparency is achieved the electron number on the quantum dot is still well defined. Higher order effects like cotunneling will however give rise to correlations between the localized electrons on the dot and the delocalized electrons in the leads. It is in this regime where one can also observe the Kondo effect that is the main focus of the experimental part of this work. The necessary details of the Kondo effect will be explained in chapter 4.

Increasing the transparency even further will allow the observation of a transport phenomenon that is a direct analog of Fabry-Perot interference in optical interferometers. The nanotube behaves like a coherent electron wave guide with the cavity being formed between the two tube-contact interfaces [29]. Also this transport regime has already been mentioned in the part on general mesoscopic transport phenomena [cf. figure 3.1].

The experimental observation of these three transport regimes is shown in figure 3.7 that has been taken from [31]. From top to bottom the samples that have been investigated become less and less transparent. While in panel (a) the high transmission leads to interference effects, in panel (b) the intermediate regime is reached in which several different manifestations of the Kondo effect can be seen. In panel (c) finally, the transmission is so low that the transport is governed by electron-electron interaction which leads to Coulomb blockade.

The samples investigated in this work lie in the intermediate regime, which is supported by the presence of higher order processes. However, regular single electron charging is still observed. In the experimental part later in this work, the important energies for interpreting the data will be deduced from transport spectroscopy.

At this point the review is restricted to the information that can be derived from the Coulomb blockade features. It reflects the subsequent filling of the shells by single electrons. This filling happens in a characteristic fashion, which allow to derive all important energy scales of the CNT QD [28]. For that an extension of the constant interaction model (CI) to five independent parameters is carried out [83]. These five parameters are the charging energy  $U$ , the quantum energy level separation  $\Delta\epsilon$ , the subband mismatch  $\delta$ , the exchange energy  $J$ , and the excess Coulomb energy  $dU$ . The intuitive meaning of these energies is visualized schematically in figure 3.8. The exchange energy  $J$  corresponds to the energy difference between parallel and antiparallel spin configurations in different orbital states. The excess Coulomb energy  $dU$  is the difference between the energy of two electrons in the same orbital state and that of two electrons in different orbital states. One can deduce following expressions for the energies

$$\begin{aligned}\Delta\mu_1 &= U + dU + J, & \Delta\mu_2 &= U + \delta - dU, \\ \Delta\mu_3 &= \Delta\mu_1, & \Delta\mu_4 &= U + \Delta\epsilon - \delta - dU, \\ \mu_1^{\text{ex}} &= \delta, & \mu_2^{\text{ex}} &= \delta - J - dU.\end{aligned}\tag{3.26}$$



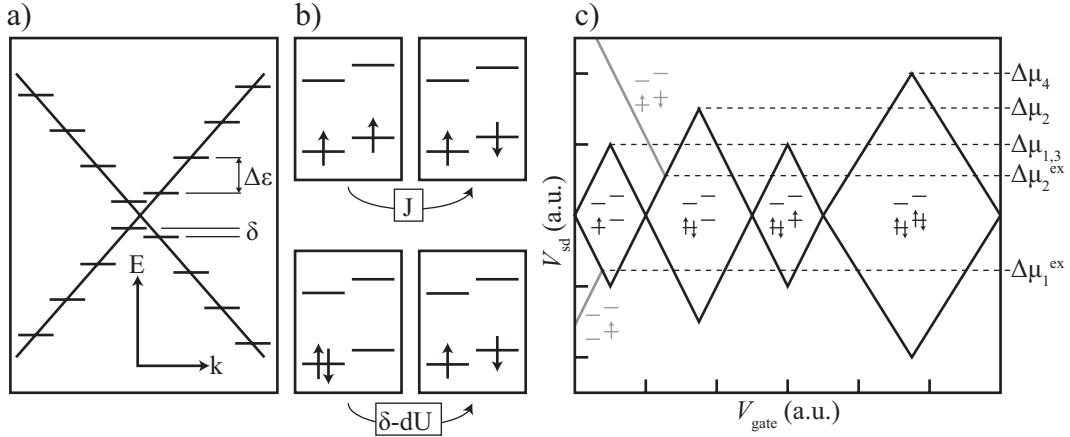


**Figure 3.8.:** Schematic of the shell filling for a four-fold symmetric metallic nanotube adapted from [28]. (a) Due to the longitudinal constriction of the tube the two linear branches of the carbon nanotube band structure get discretized. The discrete levels on each branch are spaced by the quantum level separation  $\Delta\epsilon$ . Due to, for instance, spin-orbit effects, the orbital momenta on the two branches can vary slightly. This leads to the so-called subband mismatch  $\delta$ . (b) Visualization of  $J$  and  $dU$ , two of the five independent parameters of the extended model. (c) The Coulomb diamonds in this case will follow a regular pattern of small size, medium size, small size, and large size. In the Coulomb diamonds the shell filling for the corresponding electron number is shown. For one and two electrons also the excited states  $\mu_{1,2}^{ex}$  are indicated (see text for details).

Note that the  $\Delta\mu_i$  are the addition energies for specific charge numbers as marked in figure 3.8(c). The addition “ex” for the last two equations indicates that these are transport channels in which excited states are involved.

## 4. Kondo effect

When in the 1930s the temperature dependence of the electrical resistance of different metals and alloys was investigated, two distinct types of behavior were known. For ordinary metals the resistance decreases, as lattice vibrations which disturb the regularity of the crystal lattice freeze out [cf. blue trace in figure 4.1(a)]. The finite saturation value is determined by lattice mismatches and impurity scattering. A second type of temperature dependence was observed already in 1911, shortly after the liquefaction of helium in 1908 [34]. In the laboratory of Heike Kamerlingh Onnes at the University of Leiden the resistance of mercury was observed to drop to immeasurably low values [cf. green trace in figure 4.1(a)]. This new state of matter became known as superconductivity [84].

Eventually, when dilute ferromagnetic alloys were investigated, a third type of behavior was discovered. When lowering the temperature, the resistance displays a minimum at a certain temperature after which it increases again [cf. red trace in figure 4.1(a)]. This unusual temperature dependence was a longstanding puzzle until finally in 1964 Japanese physicist Jun Kondo solved the problem with a perturbative approach [35]. Consequently this effect has been named *Kondo effect*. Kondo's solution correctly describes the dependence of the resistance at low temperatures. However, it also predicts a logarithmic divergence of the resistance at even lower temperatures. This unphysical issue was solved partly through the idea of scaling introduced by Phil Anderson in the 1960s. The full solution was eventually found by the introduction of Kenneth Wilson's numerical renormalization approach [85].

The fact that the Kondo effect is still an active field in research is due to its rediscovery in mesoscopic physics and especially quantum dots [39, 40, 44]. This system, compared to the bulk systems with ferromagnetic impurities, offers a much more direct access to many of the properties affecting the Kondo effect. The role of the impurity in the case of a quantum dot is played by an unpaired spin on the dot. The following introduction has been inspired by the concise accounts given in Refs. [71, 86].

### 4.1. General description

The qualitative picture for understanding the Kondo effect is straightforward. It is based on the assumption that a spin degenerate impurity exists and is only singly occupied by an electron. This unpaired spin is screened by the mobile electrons of the metal. This was



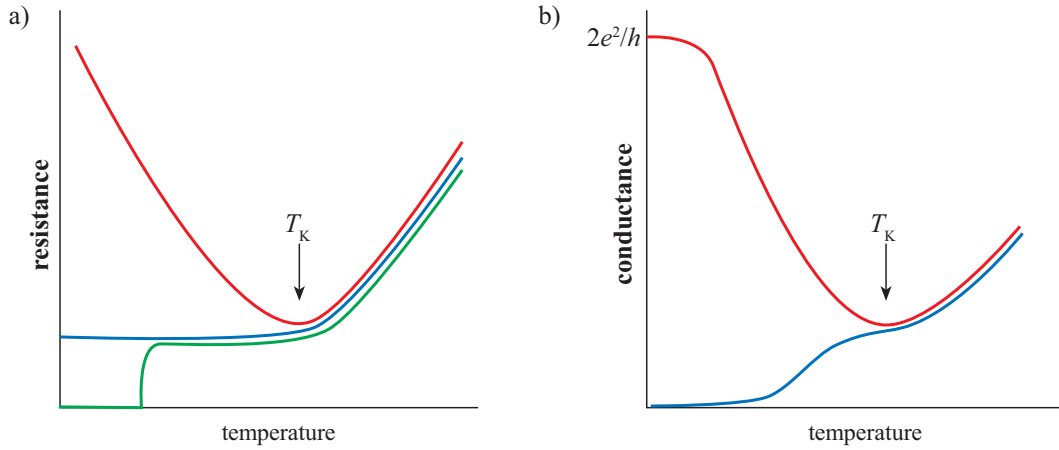


**Figure 4.1.:** (a) Different temperature dependences of the resistance of bulk materials. Normal metals (—) show a finite resistance at low temperatures. Superconductors (—) on the other hand feature an immeasurably low resistance below a certain critical temperature. Metals containing ferromagnetic impurities (—) were found to display an unusual resistance minimum at temperatures on the order of 10 K below which the resistance rises again. (b) For a quantum dot the result of the Kondo effect is exactly the opposite of the result in bulk materials. While the conductance usually decreases for decreasing temperatures (—), the Kondo correlations give rise to a logarithmic increase of the conductance (—) below temperatures of typically half a kelvin to several kelvin.

described in 1961 by P. Anderson in Ref. [87] by assuming a single level with an energy  $\epsilon$ . The impurity carries a spin  $1/2$ . However, via virtual transitions of the free electrons between the conduction band and the impurity the spin of the impurity can be flipped. The consequence of a coherent summation of many such transitions is the formation of a new state at the Fermi energy of the metal, cf. figure 4.2. This state is called the *Kondo resonance*. In the bulk metal it offers a large density of states into which electrons can be scattered. This can be visualized as a cloud of electrons with the opposite spin to that of the impurity surrounding the location of the unpaired spin. This *Kondo cloud* increases the scattering cross section of the impurity thus increasing the resistance. In figure 4.2 the exchange process between the free electrons and the impurity spin is indicated by the red dashed ellipses which symbolizes the spin singlet that is formed. The binding energy of this spin singlet corresponds to the so-called Kondo temperature. It is also seen in the energy width of the resonance.

Today the Kondo effect has seen an unprecedented revival in mesoscopic physics [39]. It owes this to the fact that its appearance in quantum dots fabricated from semiconductor heterostructures [40, 41] or nanotubes [43] is accompanied by a high tunability. Thus, different predictions for the Kondo effect can readily be tested within one system only by adjusting e.g. the tunnel coupling, the temperature, or the gate potential. In recent

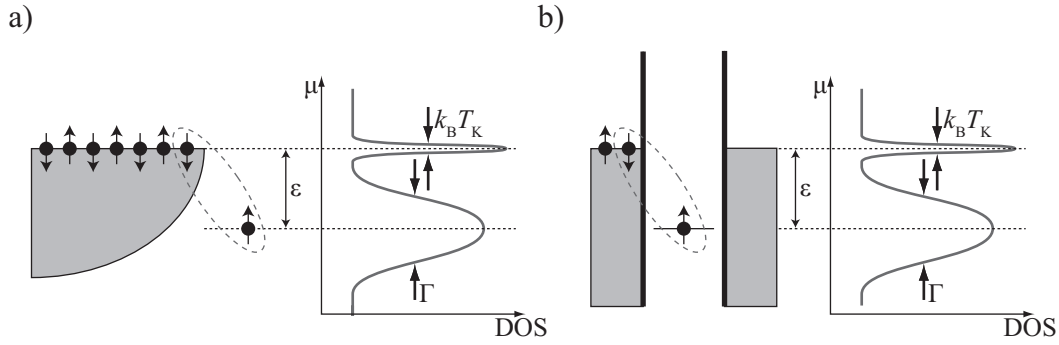


**Figure 4.2.:** Kondo effect in metals and quantum dots. (a) Schematic of the spin exchange between the electrons of the host material and the spin of a localized impurity. The coherent superposition of many such exchange events gives rise to a sharp resonance in the density of states (DOS) at  $\mu = E_F$ . The linewidth of the Kondo resonance is typically much sharper than that of the localized state. (b) Analogous situation for a quantum dot. The role of the impurity spin is played by an unpaired electron on the spin degenerate quantum dot state.

years the growing understanding of the Kondo effect has led to an almost technological employment of it to test other fundamental predictions.

The qualitative picture of the Kondo effect in quantum dots relies on the same arguments as for bulk metals. The quantum dot replaces the impurity mentioned above, see figure 4.2(b). An unpaired spin on the quantum dot is screened by a cloud of electrons in the contacts which again results in a sharp resonance of the density of states on the quantum dot at the Fermi energy of the leads, cf. figure 4.2(b). Despite the exact same mechanism in bulk systems and quantum dots, the consequences for the transport properties of the quantum dot are exactly the opposite. Instead of increasing the resistance, the conductance increases [88, 89]. This can again be understood qualitatively by appreciating that the Kondo resonance is built up by charge transition effects from both leads. This introduces a mixing of states from opposite leads which results in the increased conductance as shown in figure 4.1(b).

The intuitive but strongly simplified picture that illustrates the Kondo effect in a quantum dot is shown in figure 4.3. The different states shown in figures 4.3(a) to (c) effectively flip the spin on the quantum dot. Coherent superposition of such spin-flip events leads to the extra resonance at the Fermi energy of the leads and gives rise to an increased conductance across the quantum dot.

Figure 4.4 shows schematically the main characteristics of electronic transport through a quantum dot in the Kondo regime, i.e. with a coupling strength between the leads and the dot sufficiently high to efficiently screen the spin by charge fluctuations. As the Kondo effect is only expected for a finite spin of the impurity, it occurs primarily for an odd number of electrons on the dot. Here, typically, the spin of one electron remains unpaired and the total spin of the quantum dot is  $S = 1/2$ . For an even number of electrons the spin

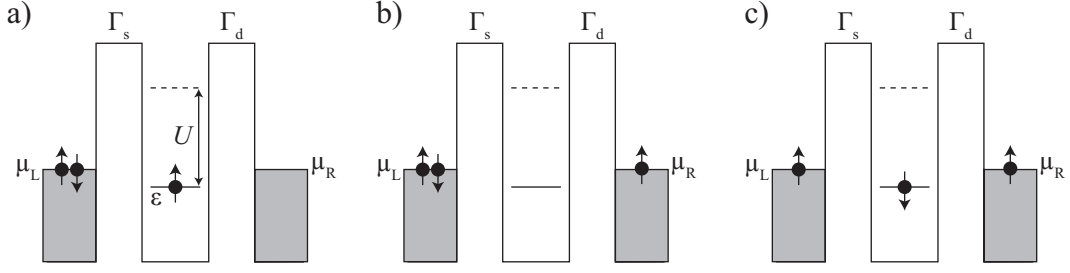


**Figure 4.3.:** Schematic of the effective spin flip process leading to the Kondo conductance across a quantum dot. (a) Coulomb blockade due to charging energy  $U$  for a state at energy  $\varepsilon$  below  $E_F$  of the leads. (b) Classically forbidden virtual state. (c) An electron with opposite spin tunnels onto the dot. The dot spin has effectively been flipped.

is  $S = 0$  in the simplest case, and Kondo correlations do not arise. This is illustrated by the linear conductance plotted versus the gate voltage at different temperatures shown in figure 4.4(a). For a temperature above the Kondo temperature ( $T_3 > T_K$ ) no conductance enhancement is observed. At a temperature slightly below the Kondo temperature ( $T_2 \lesssim T_K$ ) the Kondo correlations already strongly influence the conductance in every second, i.e. odd valley. Finally at the lowest temperature ( $T_1 < T_K$ ) the conductance in the ideal case reaches  $G = 2e^2/h$ , the theoretical maximum for transport across a spin degenerate channel.

Figure 4.4(b) shows another central aspect of Kondo correlations, the typical temperature dependence of the conductance. It has been shown in [90] that the result for the differential conductance at zero dc bias obtained from numerical renormalization group calculations [91] can be expressed in a simple empirical formula as

$$G(T) = G_0 \left( \frac{T_K'^2}{T^2 + T_K'^2} \right)^s, \quad (4.1)$$

where  $T_K' = T_K / \sqrt{2^{1/s} - 1}$  so that  $G(T_K) = G_0/2$ . The parameter  $s$  is a fit parameter which has been determined in [90] to be  $s = 0.22 \pm 0.01$  for a spin 1/2 impurity. The Kondo temperature  $T_K$  corresponds to the binding energy of the spin singlet that is formed between the localized, unpaired electron and the electrons in the surrounding electrodes. The expression for  $T_K$  in the single Anderson impurity model contains all relevant parameters of the system and can be written as

$$k_B T_K = \frac{\sqrt{\Gamma U}}{2} e^{\pi \varepsilon (\varepsilon + U) / \Gamma U}. \quad (4.2)$$

Note that  $T_K$  does strongly depend on the level position  $\varepsilon$  and such the Kondo enhanced conductance is strongest, i.e.  $T_K$  is largest, near the degeneracy points  $\varepsilon \rightarrow 0$  and  $\varepsilon \rightarrow -U$ . Consequently, in the normal case of a spin 1/2 Kondo resonance, the center of the charge state,  $\varepsilon = -U/2$  would not be the ideal point to investigate the temperature dependence; a

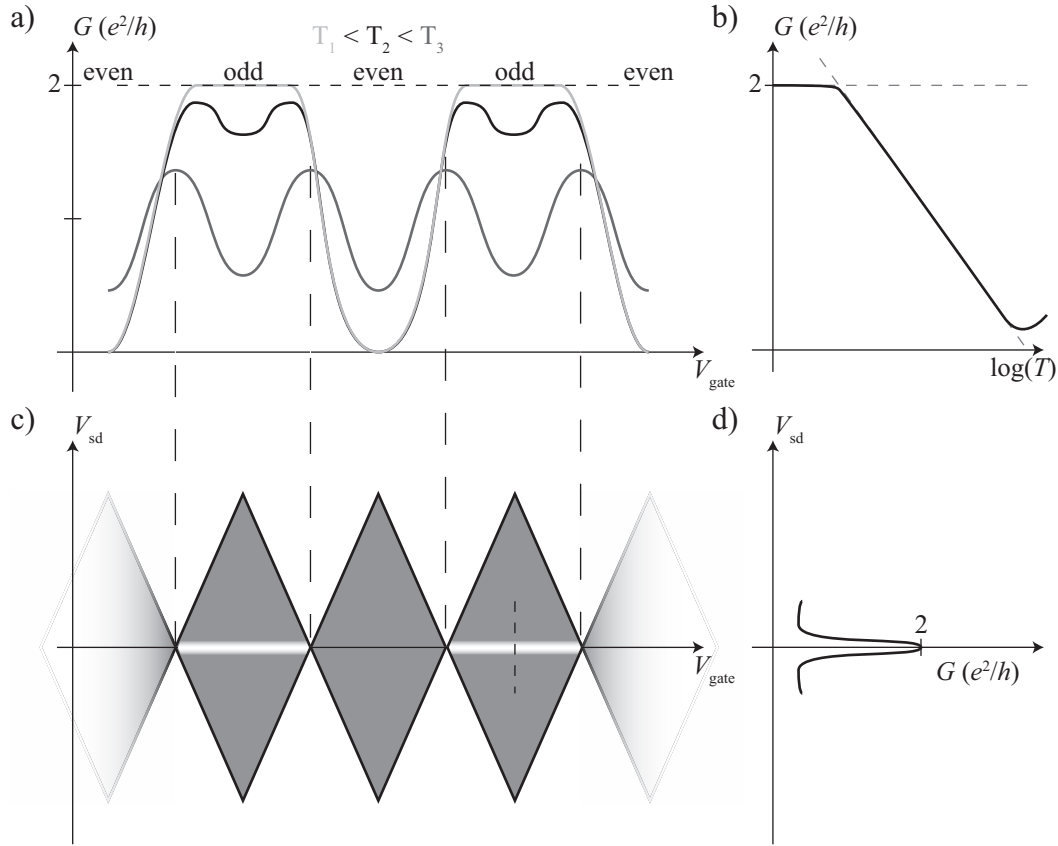


**Figure 4.4.:** Main characteristics of electronic transport through a Kondo quantum dot. (a) Linear conductance versus gate voltage for different temperatures. The Kondo temperature in this case is  $T_K \gtrsim T_2$  and accordingly  $T_1 < T_K < T_3$ . In the odd carrier number valleys the Kondo effect increases the conductance theoretically all the way to the unitary limit. (b) The temperature dependence of the conductance shows a characteristic logarithmic behavior. (c) In the stability diagram  $G(V_{sd}, V_{gate})$  the increased conductance shows up as a horizontal line in every second Coulomb diamond. (d) Zero bias resonance along the dashed line in (c) caused by the Kondo effect.

larger range of temperature values could be covered closer to the degeneracy points. The Kondo temperature  $T_K$  contains all characteristic parameters of the system and sums them up in one quantity. This results in a very distinct behavior of Kondo correlations. Let us consider for instance the temperature dependence of the Kondo conductance for systems with, e.g., different  $\Gamma$  or different  $U$ . Then all the properties of the system are summed up by the Kondo temperature and the temperature dependences for different systems collapse on one *universal* curve if the temperature is scaled by the Kondo temperature, i.e. if the

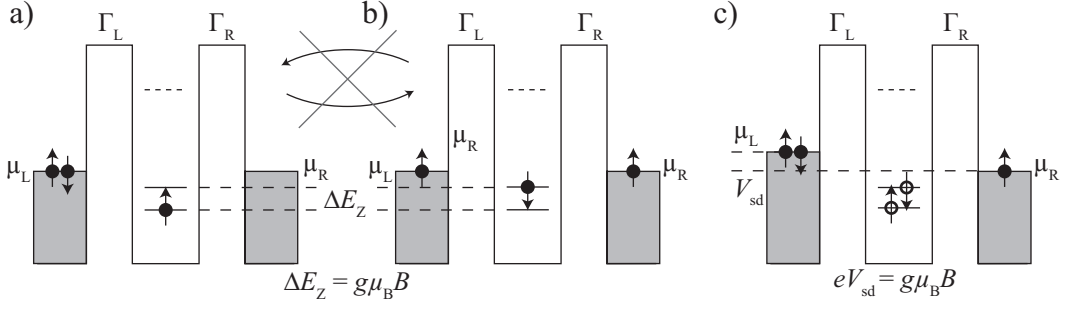


**Figure 4.5.:** (a) and (b) With an external magnetic field  $B$  the spin degeneracy of the quantum dot is lifted and initial and final states are not connected by zero energy fluctuations any more. (c) The energy difference necessary for the fluctuations to occur needs to be supplied by, e.g., a bias voltage  $V_{sd}$ .

normalized conductance  $G(T)/G(T=0)$  is plotted versus  $T/T_K$ , see chapter 8 for more details.

In figure 4.4(c) and (d) the signature of the Kondo resonance in the differential conductance is illustrated. The experimental fingerprint of the Kondo effect in a stability diagram is a line of increased conductance at zero bias across every second Coulomb diamond. The relation to the linear conductance gate trace is indicated by the dashed lines. The short dashed line vertically across the Kondo resonance finally marks the spot along which the differential conductance trace in figure 4.4(d) is plotted.

The picture used in figure 4.3 also helps understanding another important property of the Kondo effect. In an external magnetic field the spin degeneracy of the quantum dot state is lifted, essentially making one spin direction the designated ground state. The fact that the two spin directions are now separated by a finite Zeeman energy  $\Delta E_Z = g\mu_B B$  inhibits fluctuations between the two states of opposite spin directions [cf. figures 4.5(a) and (b)]. Only if the energy difference between these two states is provided through a bias voltage between the source and drain contacts, fluctuations screening the spin can occur again. The condition for this bias voltage is

$$|eV_{sd}| = g\mu_B B, \quad (4.3)$$

where  $B$  is the external field,  $\mu_B$  the Bohr magneton and  $g = 2$  the  $g$ -factor of an electron in a nanotube. Since this condition is fulfilled twice, once for forward and once for backward bias, the resonance lines due to the Kondo effect lie at

$$V_{sd} = \pm g\mu_B B/e, \quad (4.4)$$

see figure 4.6. The distance between the two conductance resonances observed in transport experiments is therefore expected to be

$$\Delta V_{sd} = 2g\mu_B B/e. \quad (4.5)$$

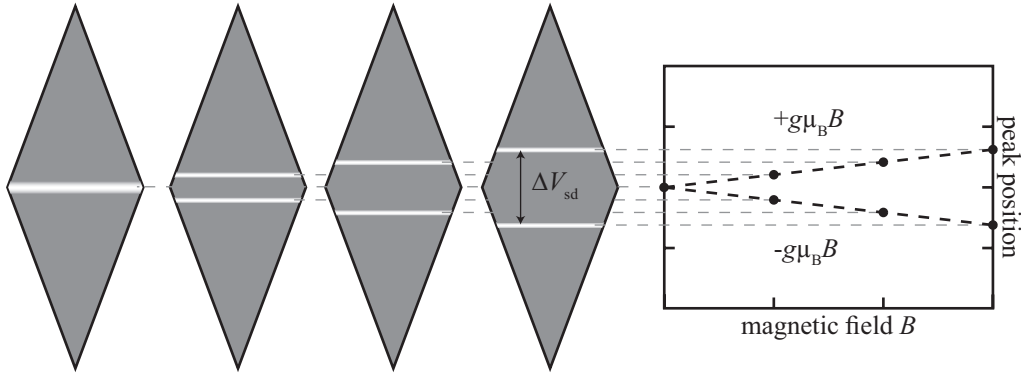


**Figure 4.6.:** Implications of an external magnetic field on the Kondo effect. As sketched in figure 4.3(f) the fluctuations between the two spin directions are now only possible if a finite voltage  $V_{sd}$  is applied supplying the energy  $eV_{sd} = \pm g\mu_B B$ .

## 4.2. The Kondo effect with ferromagnetic contacts

In the previous section the Kondo effect was shown to arise if an unpaired spin is present on the quantum dot. The result of the Kondo correlations is a sharp peak in the density of states of the quantum dot which lies at the position of the Fermi level of the leads. An external magnetic field leads to a splitting of the zero bias conductance peak to finite bias voltages, which correspond to the Zeeman energy of the electrons in the external field. Thus, interesting consequences can be expected when ferromagnetic material is used for the source and drain contacts of the quantum dot. It will be shown here that the influence on the Kondo effect is not simply that of a stray field giving rise to a Zeeman splitting, but rather a change of the level structure of the quantum dot, which is reflected as a peculiarity of the Kondo effect.

The root of this influence are spin dependent charge fluctuations leading to a renormalization of the quantum dot level. The size of the renormalization can be described well by treating the charge fluctuations as a perturbation to the bare Hamiltonian. As has been said before, the effect of charge fluctuations, meaning a variation of the charge number of the dot, can be treated as a small perturbation of the dot with constant charge number. The second order correction for the ground state energy due to a perturbation is known from quantum mechanics textbooks to be always negative [92]. In other words, the renormalization due to charge fluctuations will shift the quantum dot state to lower energies in a spin-dependent fashion. One has to identify how “easily” the charge fluctuations can occur in order to determine the size of the energy shift.

The tunneling induced level shifts are - as will be shown later - on the order of a few hundred  $\mu\text{eV}$ , while the life-time broadening of the quantum dot states typically is on the order of  $\text{meV}$ . In the regime of intermediate coupling where the effect of renormalization

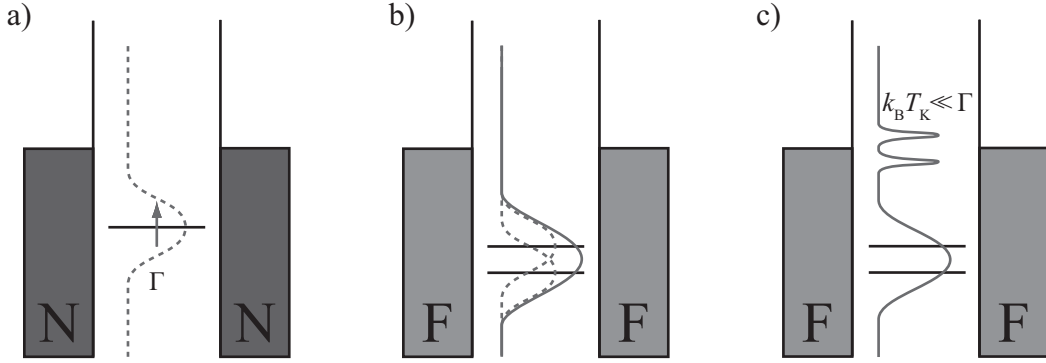


**Figure 4.7.:** (a) A quantum dot in Coulomb blockade. The dot level is broadened due to a finite life-time of the charge state. The broadening is determined by the coupling strength  $\Gamma$ . (b) For ferromagnetic leads the dot level is split by a tunneling induced exchange field. This splitting is typically so small that the densities of states for the two states overlap and appear as a single peak. Spectroscopically it is not resolvable. (c) For the situation of an unpaired spin on the quantum dot, the Kondo effect provides a sharp resonance of width  $k_B T_K \ll \Gamma$  that allows to distinguish the splitting of the dot level.

will be appreciable the presence of the leads at the same time destroys the possibility to resolve this effect. Fortunately, the Kondo effect introduced in the previous section occurs precisely in this same regime and gives rise to a sharp resonance in the density of states at the Fermi level of the leads. The width of this resonance is on the order of  $k_B T_K \ll \Gamma$ . This gives a sharp spectroscopic tool to resolve the splitting of the levels by investigating the Kondo resonance, as illustrated in figure 4.7.

The influence of ferromagnetic contacts on the level structure of a quantum dot in the Kondo regime has theoretically already been extensively studied [49, 51–53, 93]. For the sake of simplicity the theoretical treatment will be only crudely summarized. For the interested reader the above mentioned references are the entry points into a deeper discussion of the details. When any reference to theory is given in this section, it will mostly be from the latest of these studies [53] that can be seen as a review or a summary of much of the work published before. In it the authors compare three basic spin asymmetric densities of states which are

1. a finite spin polarization in the leads (at the Fermi surface),
2. a Stoner splitting of the bands, and
3. an arbitrary shape of the lead density of states.

The present discussion will focus on the first two of these band structure types and discuss in detail the corrections to the energy of the quantum dot level that are to be expected. The starting point is an expression for the spin-dependent energy correction of the dot level

position which reads

$$\delta\epsilon_\sigma \simeq -\frac{1}{\pi} \int d\omega \left\{ \frac{\Gamma_\sigma(\omega)[1-f(\omega)]}{\omega - \epsilon_\sigma} + \frac{\Gamma_{\bar{\sigma}}(\omega)f(\omega)}{\epsilon_{\bar{\sigma}} + U - \omega} \right\}. \quad (4.6)$$

This equation already indicates that the spin-dependent energy renormalization is not only an effect of the Fermi surface, i.e. the states at  $E_F$  but rather the full density of states. The first term of equation 4.6 describes electron-like processes which can be seen from the factor  $[1 - f(\omega)]$  that corresponds to the amount of available states for the electron from the dot to tunnel into. In the same sense the second term describes hole-like processes, indicated by the factor  $f(\omega)$  that includes the number of states from where a second electron can tunnel onto the dot. Both terms are divided by the energy difference between final and initial state. The larger this difference is, the less the according fluctuation contributes to the renormalization. The spin dependence enters through the coupling strength

$$\Gamma_\sigma(\omega) = \pi \rho_\sigma(\omega) |V(\omega)|^2$$

where  $\rho_\sigma(\omega)$ , with  $\sigma = \uparrow (\downarrow)$  and  $\bar{\sigma} = \downarrow (\uparrow)$ , is in the most general case the spin- and energy-dependent density of states and  $V(\omega)$  is the tunneling matrix element between the dot and the leads. The tunneling matrix element  $V(\omega)$  is assumed to be spin independent, and the whole spin dependence of the coupling strength  $\Gamma_\sigma$  is described by the spin-dependent density of states  $\rho_\sigma$  in the leads. Equation 4.6 is the central starting point from which the scaling can be derived for both limiting cases that are going to be examined. With equation 4.6 the total energy splitting can be expressed as

$$\Delta\epsilon^{(FM)} \equiv \delta\epsilon_\downarrow - \delta\epsilon_\uparrow + g\mu_B B_{\text{ext}}. \quad (4.7)$$

In particular, a superscript  $\mathcal{M}$  refers to a splitting contribution due to the *magnetization* and a superscript  $\mathcal{P}$  to a splitting due to the *polarization*. Concerning the terminology, see figure 4.8. A finite value of the magnetization [figure 4.8(a)] corresponds to the difference in the total number of spin-up and spin-down electrons and is defined as magnetization

$$\mathcal{M} \equiv \frac{n_\uparrow - n_\downarrow}{N_a}. \quad (4.8)$$

Here  $n_\sigma = \rho_0(D_0 + E_F \pm \Delta_{\text{St}}/2)$  is the number of spin- $\sigma$  electrons,  $E_F$  is the Fermi energy, and  $N_a$  the number of states per atom and spin orientation. This way the magnetization is described by a number between 0 and 1, and as intuition suggests, it is equal to 1 in the case that one spin subband is completely filled and the other one completely empty. The situation in figure 4.8(b) on the other hand shows a situation where the total numbers of spin-up and spin-down electrons are equal and the magnetization therefore is zero. What



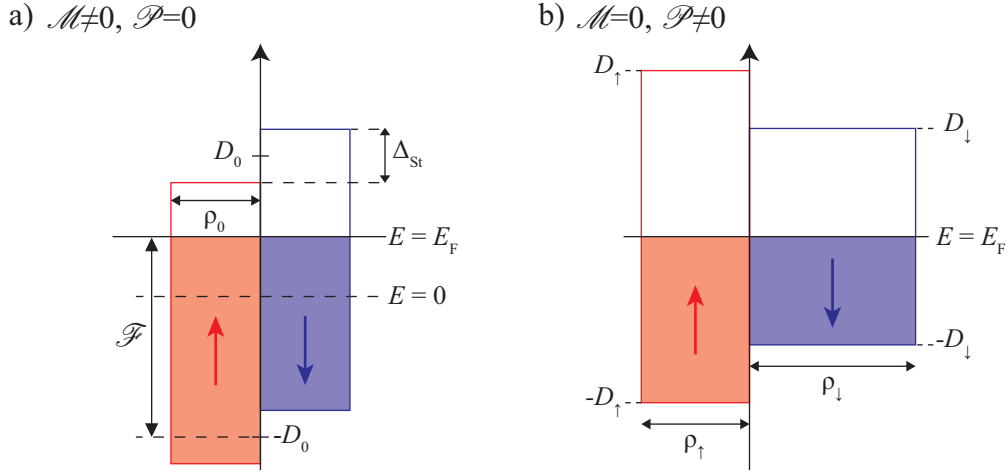


**Figure 4.8.:** Definition of the two central terms to describe the influence of ferromagnetic contacts. (a) *Magnetization*: The two bands with a bandwidth of  $2D_0$  are shifted by the Stoner splitting  $\Delta_{St}$  with respect to each other. The density of states in this case is assumed to be constant,  $\rho_{\uparrow} = \rho_{\downarrow} = \rho_0$ . The bands are filled up to a finite energy  $E$  which is described by the filling fraction  $\mathcal{F}$  (averaged over both spin directions). (b) *Polarization*: The densities of states at the Fermi level for the two spin directions are different,  $\rho_{\uparrow} \neq \rho_{\downarrow}$ . The total number of spin-up and spin-down particles are equal, meaning that the bandwidths are also different,  $D_{\uparrow} \neq D_{\downarrow}$ .

is not zero however is the polarization, which is expressed by the relative difference of the densities of states at the Fermi level for the two spin directions. It is written as

$$\mathcal{P} \equiv \frac{\rho_{\uparrow} - \rho_{\downarrow}}{\rho_{\uparrow} + \rho_{\downarrow}}. \quad (4.9)$$

#### 4.2.1. Polarization induced level renormalization

In the case of finite polarization and vanishing magnetization [see figure 4.8(b)], simple qualitative arguments can already provide an intuitive understanding. In order to determine the energy correction for a certain spin direction, the charge fluctuations for such a kind of band structure have to be summed. The two configurations that are compared in this case are sketched in figures 4.9(a) and (b). They differ in the position of the singly occupied level with respect to the Fermi level of the leads. Note that the level is still drawn to be spin degenerate before the fluctuations lift this degeneracy. In the schematics of the two dimensional stability diagram (Coulomb diamonds) which are shown in figures 4.9(c) and (d) the level positions in (a) and (b) correspond to gate voltages close to the left or close to the right degeneracy point, respectively. Accordingly the charge fluctuations taking place are different. Without loss of generality the density of states of the spin-down

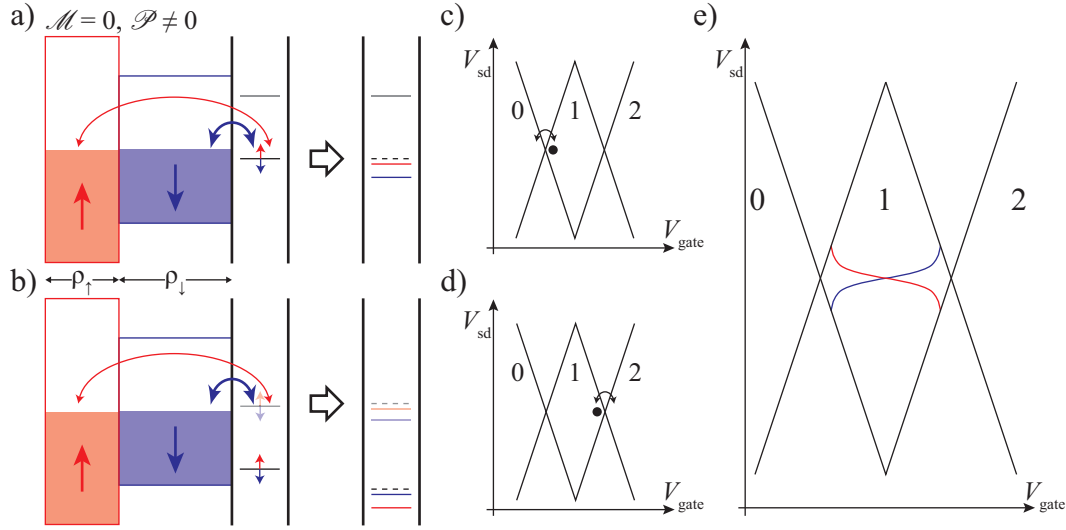


**Figure 4.9.:** This graphic shows how a finite polarization with zero magnetization leads to a spin-dependent renormalization of the quantum dot state. (a) With the occupied level slightly below the Fermi energy of the leads the charge number of the dot fluctuates between 1 and 0 [see (c)]. This results in lifting of the spin degeneracy in the depicted way. (b) Analogous situation as shown in (a) only that the charge number fluctuates between 1 and 2 [see (d)]. Again the spin degeneracy is lifted. (e) The gate dependent level renormalization carries over to a characteristic gate dependent position of the Kondo resonance (see text for details).

band is assumed to be larger than that of the spin-up band,  $\rho_{\downarrow} > \rho_{\uparrow}$ . For the situation depicted in figures 4.9(a) and (c) the fluctuations taking place can be summed up as

$$(i) \quad |1, \sigma\rangle \leftrightarrow |0\rangle$$

which means that the charge number of the dot fluctuates between one and zero. These fluctuations occur more frequently for that spin direction which finds the higher density of states in the leads to tunnel into, spin-down in this case. Thus the energy correction due to renormalization will be larger for the spin-down state compared to the spin-up state. This result is depicted in 4.9(a) to the right of the arrow (i.e. after the renormalization) by the fact that the blue line which corresponds to the spin-down state is lowered further than the red line with respect to the dashed line, the unperturbed level position.

For a gate voltage that corresponds to the vicinity of the right degeneracy point as shown in figures 4.9(b) and (d) the fluctuations will occur mostly between the singly and doubly occupied state. They can be summed up as

$$(ii) \quad |1, \sigma\rangle \leftrightarrow |2\rangle.$$

In this case it is again the spin-down level that will be renormalized to a lower energy due to the higher density of states of the spin-down band in the leads. There is however an

important difference to the previous case. If the virtually occupied state is predominantly spin-down due to the lower renormalized energy, the occupied state needs to be spin-up not to violate the Pauli principle. In other words the renormalization carries over to the state far below the Fermi level in such a way that the ground state is different from the situation described above, cf. figure 4.9(b) to the right of the arrow.

Summing up the observation for a gate voltage close to the left degeneracy point and that for close to the right degeneracy point, the total result is visualized in figure 4.9(e). The Kondo resonance displays a very characteristic gate dependent shape that mirrors the position of the two levels on the quantum dot with respect to each other. The splitting between the levels is largest close to each of the degeneracy points because the fluctuations giving rise to the renormalizations occur most frequently in this vicinity. At the electron-hole symmetric point in the center of the diamond both levels get renormalized by the same amount which results in a crossing of the Kondo resonance at zero bias. The fact that the blue line corresponding to the spin-down state is below the red one on the left side of the Coulomb diamond and above it on the right side indicates the change of ground state spin. This means that for this situation the ground state spin can be adjusted fully electrically via the gate voltage.

The detailed derivation of the quantitative expression for the energy correction in case of a finite polarization is based on a perturbative approach. Analogous to equation 4.7 the total energy difference between the corrected level energies  $\delta\epsilon_{\sigma}^{(\mathcal{P})}$  due to a finite polarization is denoted by

$$\Delta\epsilon^{\mathcal{P}} = \delta\epsilon_{\downarrow}^{(\mathcal{P})} - \delta\epsilon_{\uparrow}^{(\mathcal{P})}. \quad (4.10)$$

In the spirit of the qualitative understanding the correction can be calculated by summing up the possible electron- and hole-like fluctuations. For one spin direction, say spin-up, the correction due to these fluctuations can be written as

$$\delta\epsilon_{\uparrow}^{(\mathcal{P})} = \sum_{\substack{\omega > 0 \\ \sigma = \uparrow}} \frac{V^2}{\epsilon - \omega} + \sum_{\substack{\omega < 0 \\ \sigma = \downarrow}} \frac{V^2}{-(\epsilon + U) + \omega} \quad (4.11)$$

where the  $V^2$  in the numerator describes the energy independent tunneling between leads and quantum dot. Just as in equation 4.6 the first term describes tunneling events of the spin-up electron on the dot into empty ( $\omega > 0$ ) states of the spin-up band ( $\sigma = \uparrow$ ). The second term on the other hand describes events where the dot is virtually occupied with an additional electron from the occupied states ( $\omega < 0$ ) of the spin-down band ( $\sigma = \downarrow$ ). The denominator in both cases is the difference between the energies of the final and initial state. The charging energy  $U$  reflects the fact that the dot is occupied with an additional electron during these fluctuations. The sums can be rewritten as integrals

$$\delta\epsilon_{\uparrow}^{(\mathcal{P})} = \rho_{\uparrow} V^2 \int_0^{D_0} \frac{d\omega}{\epsilon - \omega} + \rho_{\downarrow} V^2 \int_{-D_0}^0 \frac{d\omega}{-(\epsilon + U) + \omega} \quad (4.12)$$

$$= \frac{\Gamma_{\uparrow}}{\pi} \ln \left| \frac{\epsilon}{D_0 - \epsilon} \right| - \frac{\Gamma_{\downarrow}}{\pi} \ln \left| \frac{D_0 + \epsilon + U}{\epsilon + U} \right| \quad (4.13)$$

which makes the resemblance to equation 4.6 even more obvious.<sup>1</sup>

The only difference to equation 4.6 is that the terms  $[1 - f(\omega)]$  and  $f(\omega)$  in the numerators of equation 4.6 are very simple in the present case. For the given limits of the integration  $f(\omega) = 1$  and  $[1 - f(\omega)] = 1$ , respectively. Note that without loss of generality here the Fermi level is assumed to be at  $E_F = 0$ . For the present case of a flat (energy independent) band the perturbation  $\rho_{\sigma} V^2$  was replaced by  $\Gamma_{\sigma}/\pi$ . The analogous result follows for the second spin direction, which can be written as

$$\delta\epsilon_{\downarrow}^{(\mathcal{P})} = \frac{\Gamma_{\downarrow}}{\pi} \ln \left| \frac{\epsilon}{D_0 - \epsilon} \right| - \frac{\Gamma_{\uparrow}}{\pi} \ln \left| \frac{D_0 + \epsilon + U}{\epsilon + U} \right|. \quad (4.14)$$

With equation 4.10 the total correction due to charge fluctuations for a band structure with finite polarization and zero magnetization is given by

$$\Delta\epsilon^{(\mathcal{P})} \simeq \frac{1}{\pi} (\Gamma_{\uparrow} - \Gamma_{\downarrow}) \ln \left[ \frac{\epsilon + U}{|\epsilon|} \right]. \quad (4.15)$$

With the definition of the polarization  $\mathcal{P} = (\rho_{\uparrow} - \rho_{\downarrow})/(\rho_{\uparrow} + \rho_{\downarrow})$  and  $\Gamma = \Gamma_{\uparrow} + \Gamma_{\downarrow} = \pi(\rho_{\uparrow} + \rho_{\downarrow})V^2$  finally the end result for the correction due to spin-dependent charge fluctuation at finite polarization can be written as

$$\boxed{\Delta\epsilon^{(\mathcal{P})} = \frac{\mathcal{P}\Gamma}{\pi} \ln \left[ \frac{\epsilon + U}{|\epsilon|} \right]}. \quad (4.16)$$

Note that the energy independent but spin dependent coupling in this case can be parametrized by the polarization  $\mathcal{P}$  as  $\Gamma_{\uparrow(\downarrow)} = 1/2\Gamma(1 \pm \mathcal{P})$ . So, since  $\Gamma_{\sigma} = \pi\rho_{\sigma}V^2$ , the spin dependence of  $\Gamma_{\sigma}$  for technical reasons can be absorbed in a spin dependent tunneling matrix element  $V \rightarrow V_{\sigma} = V\sqrt{1/2(1 \pm \mathcal{P})}$ . This allows to treat the leads essentially as unpolarized.

---

<sup>1</sup>Note that we assume  $D_{\uparrow} = D_{\downarrow} = D_0$  for the calculation. Since the bandwidth is in any case much larger than both charging energy  $U$  and level position  $\epsilon$ , a difference between  $D_{\uparrow}$  and  $D_{\downarrow}$  will not influence the result.

### 4.2.2. Magnetization induced renormalization

In analogy to the just discussed case of finite *polarization* also the situation of finite *magnetization*  $\mathcal{M}$  and zero *polarization*  $\mathcal{P}$  is first going to be described qualitatively. Later, when the description is going to become more quantitative, reasonable assumptions are made. These assumptions are that the bandwidth  $D_0$  and the Stoner splitting  $\Delta_{\text{St}}$  both are much larger than the energy of the quantum dot level and the charging energy,

$$\Delta_{\text{St}}, D_0 \gg |\varepsilon|, \varepsilon + U.$$

Both assumptions are well met in realistic situations. The magnetism of typical band ferromagnets such as Fe, Co, and Ni is mainly related to electron correlations in the spatially strong confined  $d$  bands. The strong spatial confinement by virtue of the uncertainty principle makes the bands rather wide in terms of energy. Typical bandwidths are on the order of several eV, and the value for the Stoner or exchange splitting of the bands in pure Nickel can for instance be found in [94] to be 300 meV. At the composition of the ferromagnetic alloy that is used in the present experiment with a Nickel content of 70% no considerable deviations from these values are expected. The energy of the quantum dot state  $\varepsilon$  with respect to the Fermi energy  $E_F$  however is on the order of a few meV at most, and the same holds for the charging energy  $U$ . This essentially means that the position of the level with respect to the band edges does not matter for the size of the effect, suggesting a gate voltage independence of this contribution.

The frequency of charge fluctuations can be compared for the two different spin directions by considering a schematic picture as shown in figures 4.10(a) and (b). For the exemplary case of a spin-up electron on the quantum dot the fluctuations taking place can once again be summed up as

$$(i) \quad |1, \uparrow\rangle \leftrightarrow |0\rangle.$$

In these processes the spin-up electron tunnels off and back onto the dot. The second possible type of fluctuations that can renormalize the energy of the state on the quantum dot involve tunneling events of a spin-down electron abbreviated by

$$(ii) \quad |1, \uparrow\rangle \leftrightarrow |2\rangle.$$

The rate of fluctuations for the first process is determined by the number of *empty* states in the spin-up band of the leads while for the second process it is the number of *occupied* states in the spin-down band. The empty and occupied states of the corresponding spin band constitute the phase space available for charge fluctuations for a certain spin orientation. This phase space is schematically indicated by the hatched areas in figure 4.10(a). Analogously, for the opposite spin direction, spin-down in this example, the charge fluctuations are depicted in 4.10(b). In this case the fluctuations that occur can be written as  $|1, \downarrow\rangle \leftrightarrow |0\rangle$  and  $|1, \downarrow\rangle \leftrightarrow |2\rangle$ . The rate at which these fluctuations can occur is set by the

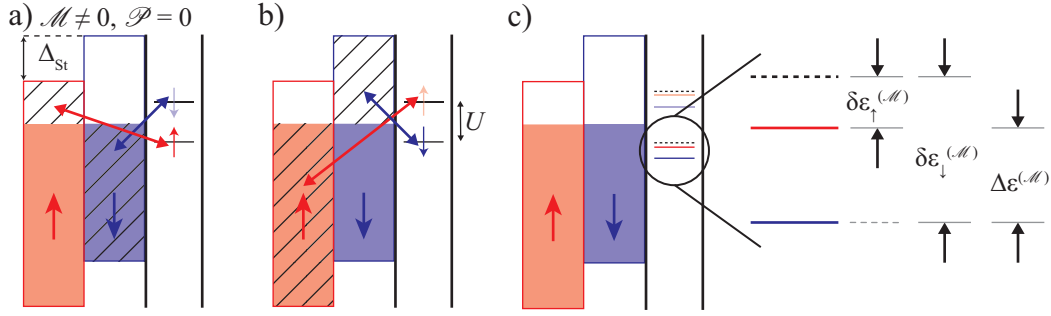


**Figure 4.10.:** Schematic tunneling induced renormalization in the case of  $\mathcal{M} \neq 0$  and  $\mathcal{P} = 0$ . (a) Charge fluctuations for a spin-up electron occupying the quantum dot. The hatched area indicates qualitatively the size of the phase space available for fluctuations. (b) Analogous situation for a spin-down electron on the quantum dot. Note that the hatched area in this case is larger than in (a), meaning that the phase space for the fluctuations is larger. This increases the energy by which the level is renormalized. (c) Resulting level structure on the quantum dot after renormalization. The close up shows the correction  $\delta\epsilon_{\uparrow}^{(\mathcal{M})}$  for the spin-up state and the correction  $\delta\epsilon_{\downarrow}^{(\mathcal{M})}$  for the spin-down state. The difference  $\Delta\epsilon^{(\mathcal{M})}$  between these two corrections is the level splitting.

number of *empty* states in the spin-down band of the leads together with the number of *occupied* states in the spin-up band. The pictorial size of the phase space for this spin direction is again indicated by the hatched areas in figure 4.10(b). The finite Stoner splitting  $\Delta_{\text{St}}$  renders the size of the two phase spaces in Fig. 4.10(a) and (b) to be different. A different size of the phase space mean essentially more frequent fluctuations and through that a different correction. This results in a lower renormalized energy for one spin direction compared to the other, as is shown schematically in figure 4.10(c). The energy correction that is induced by a finite magnetization  $\mathcal{M}$  it is labeled with a superscript  $(\mathcal{M})$ , the spin dependence by an index  $\sigma = \uparrow / \downarrow$ . The difference of the two corrections which gives the effective splitting of the levels is denoted by

$$\Delta\epsilon^{(\mathcal{M})} = \delta\epsilon_{\downarrow}^{(\mathcal{M})} - \delta\epsilon_{\uparrow}^{(\mathcal{M})}. \quad (4.17)$$

For a quantitative analysis we once more consider figure 4.8(a). For the sketched band structure the number of electrons with spin-up is given by  $n_{\uparrow} = \rho_0(D_0 + E_F + \Delta_{\text{St}}/2)$  and analogously the number of spin-down electrons by  $n_{\downarrow} = \rho_0(D_0 + E_F - \Delta_{\text{St}}/2)$ . With this the expression for the magnetization can be rewritten as

$$\mathcal{M} = \frac{n_{\uparrow} - n_{\downarrow}}{N_a} = \frac{\Delta_{\text{St}}}{2D_0}. \quad (4.18)$$

Note that  $N_a$  denotes the number of states per atom *and* spin orientation and is equal to the “area” of one spin band, i.e.  $2\rho_0 D_0$  [compare figure 4.8(a)]. The fluctuations

renormalizing for example a spin-up state can be summed up as

$$\delta\epsilon_{\uparrow}^{(\mathcal{M})} = \sum_{\substack{\omega > E_F \\ \sigma = \uparrow}} V^2 \frac{1}{\epsilon_0 - \omega} + \sum_{\substack{\omega < E_F \\ \sigma = \downarrow}} V^2 \frac{1}{-(\epsilon_0 + U) + \omega}, \quad (4.19)$$

where the tunnel matrix element  $V^2$  describes the perturbation by charge fluctuations. Note that in this case the Fermi energy is not simply taken to be at 0 as was done for the purely polarized case. The level energy  $\epsilon$  with respect to the Fermi energy  $E_F$  then can be expressed by the level energy with respect to 0 as  $\epsilon_0 \equiv \epsilon + E_F$ . This equation again reflects very intuitively what has been said in the qualitative discussion leading up to this point. The first term incorporates fluctuations of the spin-up ( $\sigma = \uparrow$ ) electron with an energy  $\epsilon_0$  from the dot into empty states ( $\omega > E_F$ ) of the leads. The second term sums up the fluctuations of a spin-down ( $\sigma = \downarrow$ ) electron from the filled states ( $\omega < E_F$ ) of the leads onto a dot state at an energy  $\epsilon_0 + U$ . The charging energy  $U$  reflects the fact that the dot is occupied with an additional electron during these fluctuations. Replacing the summation again by an integration this can be rewritten as

$$\begin{aligned} \delta\epsilon_{\uparrow}^{(\mathcal{M})} &= \rho_0 V^2 \left( \int_{E_F}^{D_0 - \frac{\Delta_{St}}{2}} \frac{d\omega}{\epsilon_0 - \omega} + \int_{-D_0 + \frac{\Delta_{St}}{2}}^{E_F} \frac{d\omega}{-(\epsilon_0 + U) + \omega} \right) \\ &= \frac{\Gamma}{2\pi} \left[ \ln \left| \frac{\epsilon_0 - E_F}{D_0 - \frac{\Delta_{St}}{2} - \epsilon_0} \right| - \ln \left| \frac{D_0 - \frac{\Delta_{St}}{2} + \epsilon_0 + U}{\epsilon_0 + U - E_F} \right| \right]. \end{aligned} \quad (4.20)$$

Here the density of states  $\rho_0$  is equal for both spin directions, so the tunneling matrix element  $V^2$  expressed in terms of the coupling strength  $\Gamma$  in this case simply reads

$$\Gamma \equiv \pi(\rho_{\uparrow} + \rho_{\downarrow})V^2 = 2\pi\rho_0 V^2. \quad (4.21)$$

Similarly, the perturbative correction due to magnetization for a spin-down electron on the dot can be expressed as

$$\delta\epsilon_{\downarrow}^{(\mathcal{M})} = \frac{\Gamma}{2\pi} \left[ \ln \left| \frac{\epsilon_0 - E_F}{D_0 + \frac{\Delta_{St}}{2} - \epsilon_0} \right| - \ln \left| \frac{D_0 + \frac{\Delta_{St}}{2} + \epsilon_0 + U}{\epsilon_0 + U - E_F} \right| \right]. \quad (4.22)$$

and as defined in equation 4.17 the total splitting  $\Delta\epsilon^{(\mathcal{M})}$  is given by

$$\begin{aligned} \Delta\epsilon^{(\mathcal{M})} &= \delta\epsilon_{\downarrow}^{(\mathcal{M})} - \delta\epsilon_{\uparrow}^{(\mathcal{M})} \\ &= \frac{\Gamma}{2\pi} \ln \left[ \frac{(D_0 - \frac{\Delta_{St}}{2} - \epsilon_d^0)(D_0 - \frac{\Delta_{St}}{2} + \epsilon_0 + U)}{(D_0 + \frac{\Delta_{St}}{2} - \epsilon_0)(D_0 + \frac{\Delta_{St}}{2} + \epsilon_0 + U)} \right] \\ &= \frac{\Gamma}{2\pi} \ln \left[ \frac{(D_0 - \frac{\Delta_{St}}{2} - \epsilon - E_F)(D_0 - \frac{\Delta_{St}}{2} + \epsilon + U + E_F)}{(D_0 + \frac{\Delta_{St}}{2} - \epsilon - E_F)(D_0 + \frac{\Delta_{St}}{2} + \epsilon + U + E_F)} \right]. \end{aligned} \quad (4.23)$$

Note that at this point the expression still contains the level position as  $\varepsilon$  and such still predicts a dependence on gate voltage. Up to this point the same expressions can already be found in literature, see e.g. [53]. More detailed understanding can be reached by remembering the assumptions from the beginning of this section. The value of the bandwidth  $D_0$  and of the Stoner splitting  $\Delta_{\text{St}}$  as well as additionally the size of the, in this case finite, Fermi energy are much larger than  $\varepsilon$ , i.e. in detail

$$D_0, \Delta_{\text{St}}, |E_{\text{F}}| \gg |\varepsilon|, \varepsilon + U.$$

This allows to replace the parameters in equation 4.23 by accessible ones and to reduce the equation to a considerably simpler form,

$$\begin{aligned} \Delta\varepsilon^{(\mathcal{M})} &\simeq \frac{\Gamma}{2\pi} \ln \left[ \frac{(D_0 - \frac{\Delta_{\text{St}}}{2} - E_{\text{F}})(D_0 - \frac{\Delta_{\text{St}}}{2} + E_{\text{F}})}{(D_0 + \frac{\Delta_{\text{St}}}{2} - E_{\text{F}})(D_0 + \frac{\Delta_{\text{St}}}{2} + E_{\text{F}})} \right] \\ &= \frac{\Gamma}{2\pi} \ln \left[ \frac{(D_0 - \frac{\Delta_{\text{St}}}{2})^2 - E_{\text{F}}^2}{(D_0 + \frac{\Delta_{\text{St}}}{2})^2 - E_{\text{F}}^2} \right]. \end{aligned} \quad (4.24)$$

Using equation 4.18 to express the Stoner splitting  $\Delta_{\text{St}}$  in terms of the magnetization  $\mathcal{M}$  and defining  $\xi \equiv \frac{E_{\text{F}}}{D_0}$  this can be even more concisely written as

$$\Delta\varepsilon^{(\mathcal{M})} \simeq \frac{\Gamma}{2\pi} \ln \left[ \frac{(1 - \mathcal{M})^2 - \xi^2}{(1 + \mathcal{M})^2 - \xi^2} \right]. \quad (4.25)$$

The parameter  $\xi$  can be expressed by the filling fraction  $\mathcal{F}$ , defined as

$$\mathcal{F} \equiv \frac{\text{number of electrons}}{\text{number of states}} = \frac{2\rho_0 D_0 + 2\rho_0 E_{\text{F}}}{2\rho_0 2D_0} = \frac{1}{2}(1 + \xi). \quad (4.26)$$

With this the final expression for the tunneling induced exchange splitting for finite *magnetization* and zero *polarization* contains no appearance of the level position any more and reads

$$\Delta\varepsilon^{(\mathcal{M})} \simeq \frac{\Gamma}{2\pi} \ln \left[ \frac{(1 - \mathcal{M})^2 - (2\mathcal{F} - 1)^2}{(1 + \mathcal{M})^2 - (2\mathcal{F} - 1)^2} \right]. \quad (4.27)$$

Note that equation 4.27 shows that the amount of the splitting is not mainly determined by the Stoner splitting  $\Delta_{\text{St}}$ , expressed by the magnetization  $\mathcal{M}$ , but rather by the coupling strength  $\Gamma$ . The dependence on  $\mathcal{M}$  is only logarithmic and thereby very weak.

### 4.2.3. Parabolic bands in literature

A very detailed discussion of these renormalization processes with the distinction that parabolic bands instead of flat bands were used is given in reference [53]. In equation (24)



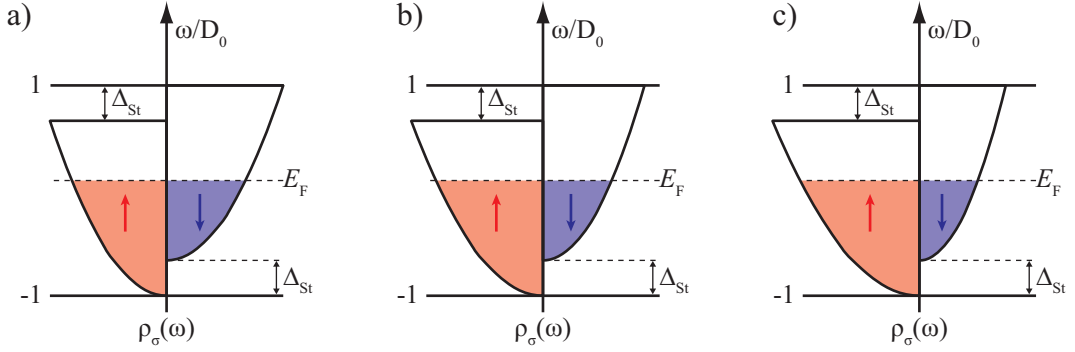


**Figure 4.11.:** Reproduced and adapted from [53]. Parabolic density of states for a constant Stoner splitting, a value of  $\Delta_{St} = 0.3D_0$  was assumed, and an additional spin asymmetry  $Q$  of (a) 0.0, (b) 0.1, and (c) 0.3 (see eq. 4.28 for the exact definition of the band structure parameters  $Q$  and  $D_0$ ).

the authors consider an arbitrary density of states in the leads of the form

$$\rho_\sigma(\omega) = \frac{1}{2} \frac{3\sqrt{2}}{8} D_0^{-3/2} (1 + \sigma Q) \sqrt{\omega + D_0 + \sigma \Delta/2} \quad (4.28)$$

which allows to model the band structures depicted in figure 4.11. The difference in this case, compared to the flat band model, is that there is no parameter set that shows a purely polarized case. All band structures display a finite Stoner splitting of an assumed size  $\Delta_{St} = 0.3D_0$  where  $D_0$  is the bandwidth. The spin asymmetry at  $E_F$ , i.e. the polarization, is accounted for by the parameter  $Q$ . With equation 4.28 the definition of the polarization given in equation 4.9 then reads

$$\mathcal{P} \equiv \frac{\rho_\uparrow - \rho_\downarrow}{\rho_\uparrow + \rho_\downarrow} = \frac{\left[ (1+Q) \sqrt{E_F + D_0 + \frac{\Delta_{St}}{2}} - (1-Q) \sqrt{E_F + D_0 - \frac{\Delta_{St}}{2}} \right]}{\left[ (1+Q) \sqrt{E_F + D_0 + \frac{\Delta_{St}}{2}} + (1-Q) \sqrt{E_F + D_0 - \frac{\Delta_{St}}{2}} \right]}. \quad (4.29)$$

Note, that even for  $Q = 0$  due to the parabolic shape of the bands and the finite Stoner shift, there is already a difference of the DOS for different spin directions at the Fermi level.

By taking this band structure the authors of the corresponding reference could calculate via numerical renormalization group methods the spectral function  $\Sigma_\sigma \Gamma_\sigma A_\sigma(\omega)$  which is shown in figure 4.12. The spin resolved conductance follows from the spectral function via

$$G_\sigma = \frac{e^2}{\hbar} \frac{2\Gamma_{s,\sigma}\Gamma_{d,\sigma}}{(\Gamma_{s,\sigma} + \Gamma_{d,\sigma})} \int_{-\infty}^{\infty} d\omega A_\sigma(\omega) \left[ -\frac{\partial f(\omega)}{\partial \omega} \right]. \quad (4.30)$$

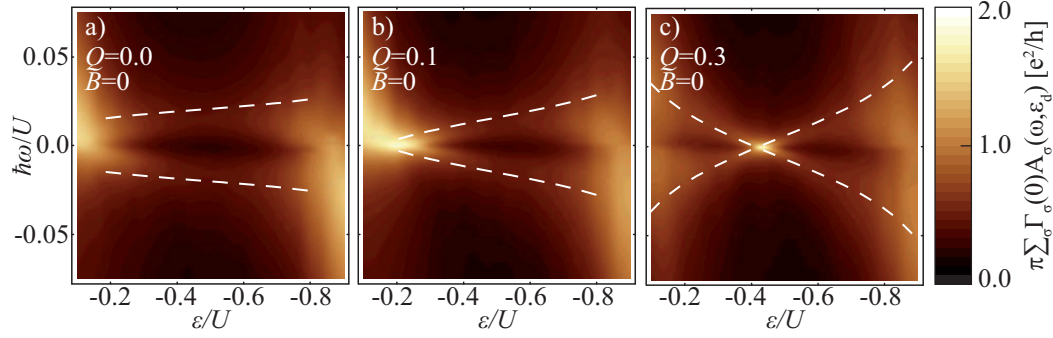


**Figure 4.12.:** Spectral function plotted versus the effective gate potential  $\varepsilon/U$  and the effective energy  $\omega/U$ . (a) For  $Q = 0$ , i.e. low polarization, the splitting is roughly independent of gate voltage. (b) At  $Q = 0.1$ , the splitting is strongly gate dependent but no compensation of the splitting is achieved. (c) For even higher  $Q = 0.3$ , the splitting is again strongly gate voltage dependent. This time at a particular gate voltage the splitting is compensated. Reproduced and adapted from [53] for the band structures shown in figure 4.11.

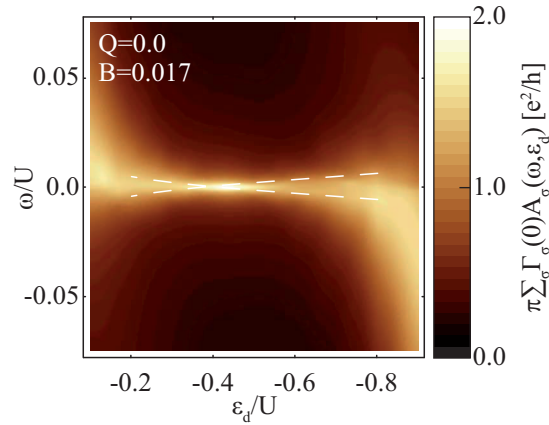


**Figure 4.13.:** Spectral function analogous to figure 4.12(a), this time however an external field is applied. For this specific band structure the result is a central resonance with a very small gate voltage dependence indicated by the dashed white lines. Note that, indicated by the dashed white lines, there is again a finite gate voltage dependence visible due to the finite spin polarization that is present because of the parabolic bands even though  $Q = 0$ .

The total conductance then is the sum of the conductances for each spin direction.

In addition to investigating the transport properties of a Kondo quantum dot coupled to ferromagnetic leads with different band structures in zero external field, the authors of Ref. [53] also model the effect of an external field. The effect of an external field was again

investigated for the three kinds of band structure that were discussed before. Figure 4.13 shows the result of this modeling for the case of the band structure shown in figure 4.11(a).

It is seen that at the specifically chosen field value the previous two resonances merge into one apparent resonance. The weak gate voltage dependence that was observed for this type of band structure in figure 4.12(a) is now not easily seen any more due to the compensation. The finite width of the conductance peaks makes them overlap so that the slope in terms of gate voltage dependence is indicated by the dashed white lines in figure 4.13.

All discussed level shifts are only observable by spectroscopy in the case that Kondo correlations occur. These deliver a sufficiently sharp resonance to resolve the small level shifts and especially the finite splitting. With equations 4.16 and 4.27 all necessary tools for quantifying the experimental results are available.

## 5. Sample fabrication and experimental methods

After the importance of geometrical length scales has been stressed already on plenty occasions during the introductory parts of this work, this chapter provides a short overview of the steps that led to the mesoscopic samples that have actually been measured. The process can be divided into three steps which are nanotube growth, nanotube localization, and electron beam lithography including metallization and lift-off. After completion of these steps the samples are usually characterized electronically at room temperature in a probe station and bonded in a chip carrier that can be mounted into the sample holder of a cryogenic setup. One of the already mentioned advantages of chemical vapor deposition, the process that generated the tubes for the present investigation, is scalability. This has been put to use here, meaning that the tubes that were measured have been produced in a single growth run on a large piece of substrate [95].

### 5.1. Sample fabrication

This section briefly summarizes the steps towards a typical sample that was used for transport measurements. Detailed process parameters are given in appendix A.

#### 5.1.1. Wafer material

Appropriate wafer material has to provide the possibility to electrostatically influence the potential of the device. This is realized by using a highly doped silicon wafer with an insulating silicon oxide top layer. The insulating layer is generated via thermal oxidation. For the samples in this work a typical oxide thickness of 300 nm was used. The relative permittivity of silicon oxide has a value of  $\epsilon_r \simeq 3.9$ . If electrically and mechanically connected to the conducting bottom plate of a chip carrier by e.g. silver epoxy paint, a voltage  $V_{\text{gate}}$  can be applied to the silicon substrate. It will thereby act as a back gate for the device on top analogously to a capacitor plate. Indeed, the basic model that is used to describe the action of the back gate on the quantum dot relies on the capacitance between a cylinder (modeling the nanotube quantum dot) and a plate (modeling the substrate).

The material is then cut into pieces of typically  $4\text{ mm} \times 4\text{ mm}$ . Alternatively, if the process parameters are well controlled, a scaled up process with chip sizes of  $16\text{ mm} \times 16\text{ mm}$  is also possible. In the latter case a total of 16 chips are processed at the same time. The nanotubes used in the present work were the result of such a scaled up production run where the deposition of the catalysts, the nanotubegrowth and the definition of the alignment markers were all done by L. Herrmann [95].

### 5.1.2. Single wall nanotubes

Carbon nanotubes were grown by chemical vapor deposition (CVD). The recipe used for the growth process dates back to the work by Kong et al. [24]. The details of the recipe can be found in the appendix.

For later alignment of the desired structures to the actual position of the nanotube a grid of reference points, so called alignment marks, is required. For that purpose the highly doped p++ silicon wafer is coated with the e-beam lithography (EBL) resist polymethyl methacrylate (PMMA). This synthetic polymer is sensitive to the electron beam in the sense that the polymer chains are split in smaller chain lengths which increases the solubility by solvents like methyl isobutyl ketone (MIBK) or isopropyl alcohol. This type of resist is called positive. In the opposite case of a negative resist, the exposed areas are insensitive to the developer and all the non exposed resist is dissolved.

Depending on the temperature stability of the material that is used for the markers this step can be done either before or after the CVD growth of the nanotubes. In the present case, the alignment markers were made of gold, which provides good contrast under the electron microscope but which also severely deforms under the influence of the high temperatures during the growth process. This makes the markers sometimes hard to interpret and in extreme cases dissolves them completely. If the markers are structured afterwards however, the already grown nanotubes will be exposed to PMMA one additional time which increases the degree of contamination of the nanotubes. Hence, the ideal strategy is to pattern the markers beforehand with a material that does not melt at the temperatures during growth. Good experiences have been made with e.g. a small layer of gold on a temperature stable chromium base or alternatively platinum on a sticking layer of tungsten. A typical example of alignment markers is shown in figure 5.1. Such an array allows to uniquely identify the position of the nanotube. Each  $4\text{ mm} \times 4\text{ mm}$  chip has four groups of four such arrays so that potentially 16 nanotube positions can be referenced, cf. figure 5.1.

The next step is to structure an array of catalyst droplets. This catalyst dissociates the gas later during the growth process, i.e. the carbon nanotubes are in most cases growing out of these catalyst dots. The catalyst is a mixture of fine grained metal compounds like for instance  $0.05\text{ mmol}/15\text{ mg}/15\text{ ml Fe(NO}_3)_3 \cdot 9\text{H}_2\text{O}/\text{alumina}$  brought into suspension in methanol. In order to restrict the growth to desired positions, the catalyst accordingly

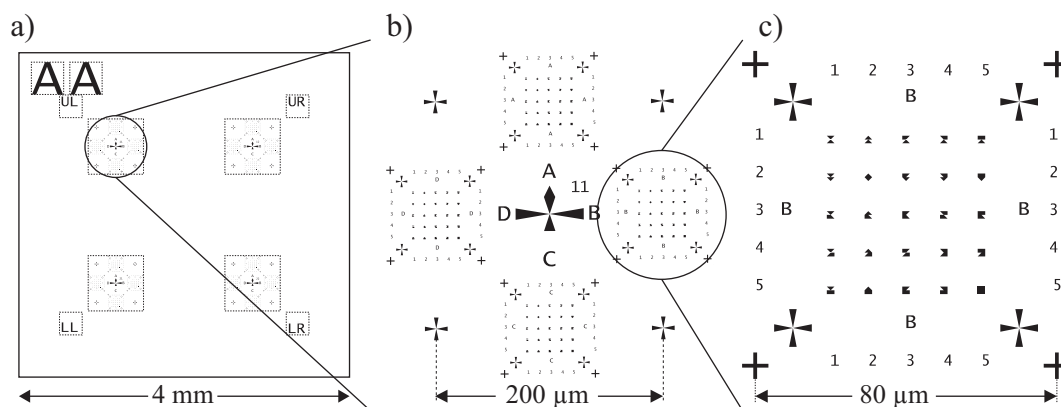


**Figure 5.1.:** This figure shows the typical pattern of alignment marks that has been used for referencing the position of the nanotube. (a) The black frame here indicates typical sample dimensions. (b) One of the four groups of areas referenced by alignment marks. (c) Close up of one of the alignment mark areas. Each symbol is unique, allowing to locate the absolute position also if only a small fraction of the total array is visible.

has to be supplied only at these desired points again by EBL. After developing, the result in this case is a pattern of holes where the bare substrate is exposed. This pattern of holes in the resist is used to structure an array of catalyst droplets. The catalyst suspension is brought onto the sample with a pipette and ideally adheres to the exposed substrate forming small droplets. After application, the sample is left in air for the solvent to evaporate. A lift-off step removes the residual PMMA and only leaves the predefined pattern of catalyst dots. Afterwards the sample can be heated to, e.g., remove potential residues of the catalyst solvent.

Subsequently the sample is put into a CVD furnace which consists of a quartz glass tube about 1.5 m long that has a high power heat source surrounding it over a length of roughly 40 cm in the center. At one end of the tube an airtight feedthrough allows different gases to stream in. At the other end these gases are exiting into a venting system. For each type of gas a separate gas flow rate can be set by mass flow controllers. The specific details of the gas composition, flow rates, and temperatures differ slightly from recipe to recipe. The sample is heated up in a flow of inert gas like Argon to roughly 900 °C, at which a feedstock of carbon is provided, most commonly by methane. At 900 °C catalytic decomposition of methane outweighs pyrolysis, providing atomic carbon rather than amorphous. This step is carried out over typically 10 min, after which the sample cools down, yet again in a flow of inert gas.

Now the samples are placed into an electron microscope where they are checked for successful carbon nanotube growth. In the event that there are nanotubes that have grown out from the catalysts, particularly long and straight ones are selected. With the least possible amount of exposure to the electron beam two or three images of each nanotube and

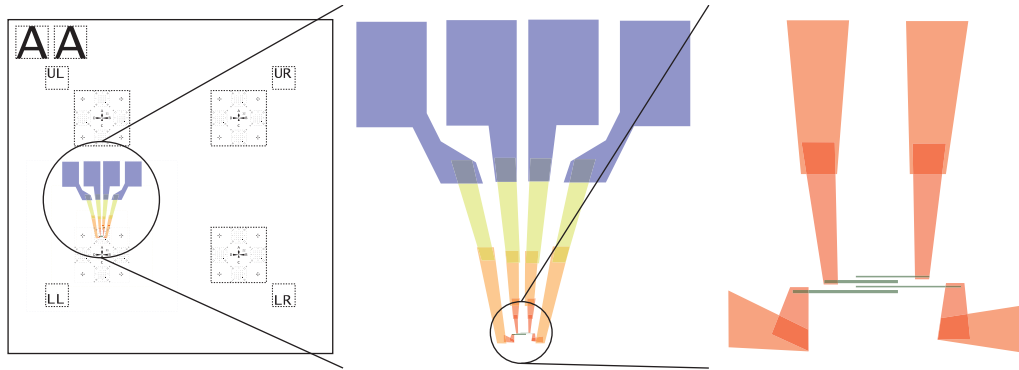


**Figure 5.2.:** This figure shows a typical structure as it was designed in eDraw<sup>TM</sup>. Different colors denote different layers that are used to set appropriate current values for the electron beam during the lithography process. The layer colored in ■ constitutes what will later be used as bonding pad, i.e. as an anchor point for the aluminum wires that are ultrasonically bonded to the structure. All the layers from ■ to ■ form what is called the leads. The actual contacts are shown in ■. This is the only part of the structure that consists of ferromagnetic material.

its surrounding at different magnifications are recorded. These images can afterwards be imported into the structure design suite for the lithography system.

### 5.1.3. Sample design

The SEM images of the selected tube and the nearest alignment markers are imported into eDraw<sup>TM</sup>. This way the position of the selected tube with reference to other structures can be evaluated easily and the leads and contacts can be designed accordingly. The actual design process is done by manually assembling the structure from polygons [cf. figure 5.2]. Already at this stage different elements of the structure can be placed into different layers. This will later allow to set appropriate current values of the electron beam during the lithography so that the larger elements of the structure will also be written in a reasonable amount of time.

The next step in this workflow is to import the structures into the actual lithography control software eLitho<sup>TM</sup>. In there the previously determined doses of exposure and the alignment steps for each constituent of the structure are set. The values used for the present samples are given in the appendix A. The alignment procedure normally consists of three steps during each of which an image at increasing magnification is recorded. After each step at least three, but normally four points are identified in the image. The corresponding points have previously also been marked in the design file and can therefore now be used to determine the absolute position of the nanotube with respect to the electron beam. For an exact adjustment it is important to that the last repositioning image has been recorded



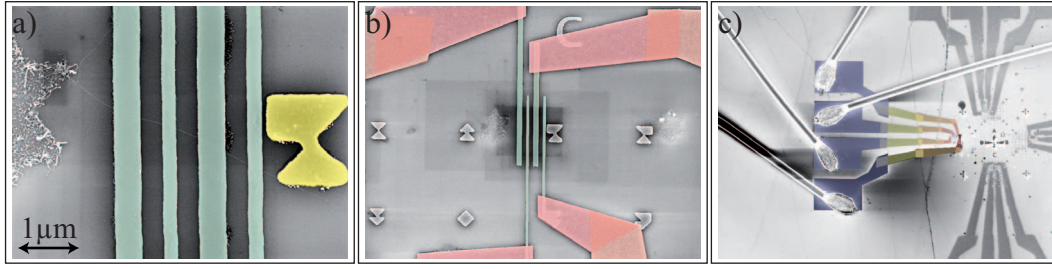


**Figure 5.3.:** (a) Close-up of an electron microscope picture of one of the samples that were used for transport experiments in this work. On the left a catalyst structure can be distinguished from which clearly a thin white line sets off diagonally across the picture. This single wall carbon nanotube is contacted by four ferromagnetic contacts (green) of different widths and an approximate distance of 300 nm. On the very right one of the alignment markers (yellow) is visible. (b) Larger overview with the gold leads contacting the green ferromagnetic contacts. At this magnification more alignment marks can be seen that are building up a grid to which nanotubes and contacts are referenced. (c) Fully contacted and bonded sample.

with the same magnification as the corresponding writing step. With the lithography file ready the sample is mounted into the electron microscope after being coated with a layer of polymethyl methacrylate (PMMA).

In total this coating and writing procedure has to be done twice because the last part of the structure in contact with the nanotube is going to be made of a ferromagnetic material. As the domain configuration in the contact should not be influenced by the leads, these were made of a nonmagnetic material, Au in the present case. Both materials are evaporated thermally in a high vacuum chamber. The gold layer had a 5 nm Titanium sticking layer underneath and itself a thickness of about 40 nm to 50 nm. The layer thickness of PdNi was on the order of 50 nm. The oscillating quartz crystal for measuring the deposited material thickness in the system in which the evaporation was carried out was only calibrated for Nickel so the actual layer thickness may deviate.

The magnetic properties of the contact material will be discussed in the following section of this chapter. Each evaporation process was completed by a standard lift-off step in warm isopropyl alcohol during which redundant parts of the metal were removed by dissolving the residual PMMA underneath.

The following step is to test and select the individual devices in terms of quality and functionality. This is necessary because as mentioned before, on every chip there are potentially 16 devices each of which is fabricated to have four electrodes. This would lead to a total of 64 necessary connections which is impossible with the standard chip carriers that are used in the low temperature setup. They provide only a maximum of 20 connections. Because of complications during bonding and thermal voltages between coaxial and standard cables typically a maximum of 15 connections are established. Typically



only two or three devices have been wire bonded in the present case which have to be preselected by room temperature characterization using a probe station. This process introduced an additional risk of damaging the samples, e.g. in terms of gate leakages. Still it has proven to be the quickest way to scan a large amount of samples and select the most promising ones. In case of big contact resistances the nanotube contacts can be annealed. For this also the CVD oven is used, as it provides stable temperatures and a well-defined atmosphere. In the present case the method of choice was to heat the samples to 300 °C in a flow of Argon, resulting in an overall resistance decrease. Once the devices have been selected they are glued into a chip carrier with silver paste. To increase the quality of the interface between chip and chip carrier the bottom side of the wafer can be scratched with a diamond cutter leading to clean, unoxidized interfaces. The electrical connection between chip carrier and sample is then established by wire bonding with aluminum wire [cf. figure 5.3(c)].

## 5.2. Properties of the ferromagnetic alloy $\text{Pd}_{0.3}\text{Ni}_{0.7}$

For the present experiment we require a material where both the spin imbalance and the coupling strength to the nanotube are as high as possible. The expression spin imbalance in this context sums up two signatures of magnetism at the same time, the magnetization  $\mathcal{M}$  and the polarization  $\mathcal{P}$ , both already discussed in chapter 4. This combination of high transparency and simultaneously high spin imbalance are known to be very well met by the alloy of palladium and nickel [12]. Measurements using an external field to control the magnetization of the contacts and by that proving the spin filtering effect of ferromagnetic leads have already been successfully demonstrated [10, 13, 96]. A material used for these experiments often has been PdNi, which has shown a clear tunnel magnetoresistance (TMR) in several experiments [12]. One example of such a measurement is displayed in figure 5.4.

Palladium has excellent wetting properties on carbon nanotubes. Its high work function results in the absence of a Schottky barrier between the metallic contacts and the potentially semiconducting nanotubes [97]. In addition to that, palladium is a paramagnet which only very closely does not fulfill the Stoner criterion for being a ferromagnet. This criterion determines whether ferromagnetic order develops or not. The argumentation leading up to the criterion starts by realizing that in the vicinity of, e.g., a spin-up electron other spin-up electrons are driven away due to Pauli exclusion. This lowers the effective charge density around this electron and is known as exchange hole. Due to the lower charge density the Coulomb potential of the atoms is screened less efficiently and the energy of the spin-up electron is reduced. The size of the reduction of the energy is described by the Stoner

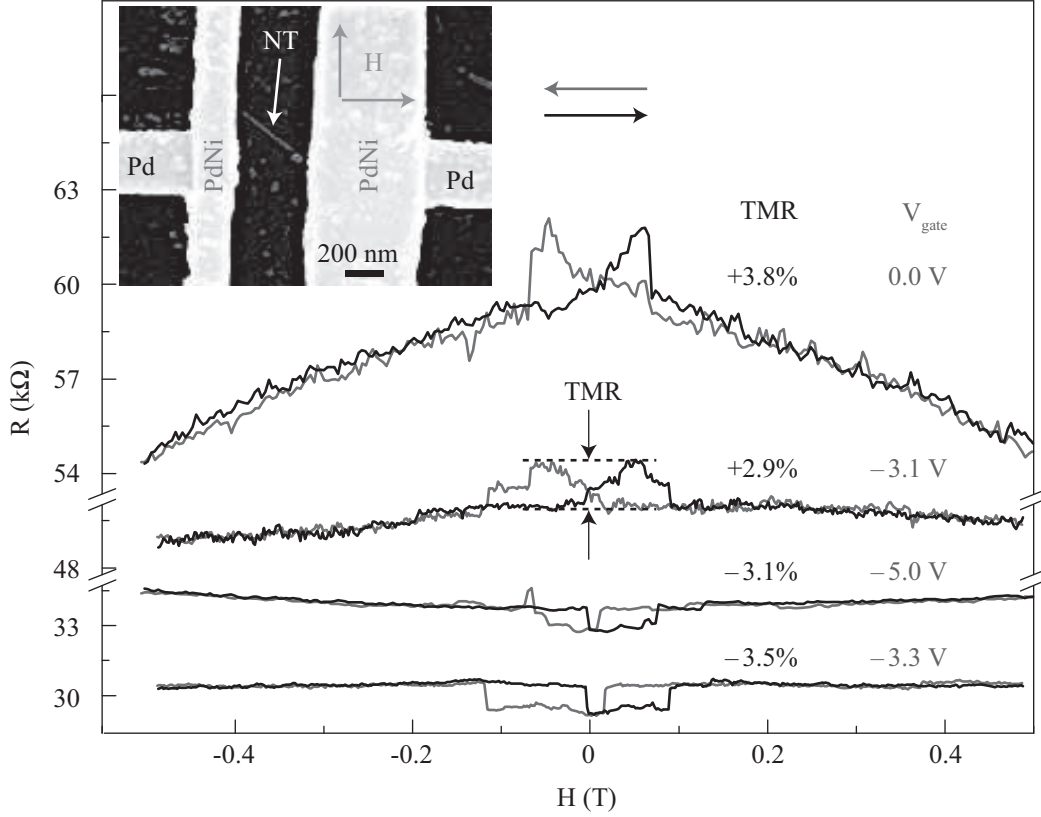


**Figure 5.4.:** Successful demonstration of spin-valve effects in carbon nanotubes with PdNi contacts from literature. The tunnel magnetoresistance (TMR), which is defined as the relative difference between the high and low resistive state as indicated in the figure, varies in size and even sign as a function of the gate voltage  $V_{\text{gate}}$ . The image has been taken with slight adaptations from [10]

parameter  $I$ . For the two spin bands the energy correction can be formulated as

$$\begin{aligned} E_{\uparrow}(\vec{k}) &= \tilde{E}(\vec{k}) - IR/2 \\ E_{\downarrow}(\vec{k}) &= \tilde{E}(\vec{k}) + IR/2. \end{aligned} \quad (5.1)$$

In this expression  $\tilde{E}(\vec{k}) = E(\vec{k}) - I(n_{\uparrow} + n_{\downarrow})/2N$ . The number of atoms is denoted as  $N$  and the parameter  $R = (n_{\uparrow} - n_{\downarrow})/N$  is the relative excess of one spin direction. With this the condition for ferromagnetism ( $R > 0$ ) can be formulated as

$$-1 - \frac{I}{N} \sum_{\vec{k}} \frac{\partial f(\vec{k})}{\partial \tilde{E}(\vec{k})} > 0. \quad (5.2)$$

Evaluating this for  $T = 0$  and expressing the density of states per atom and spin direction as  $\tilde{\rho}(E_F) = \frac{V}{2N} \rho(E_F)$ , this can be converted into the Stoner criterion

$$\tilde{\rho}(E_F)I > 1. \quad (5.3)$$

With a small amount of ferromagnetic material, such as nickel, palladium can be driven into the ferromagnetic state at low temperatures [98]. The actual composition of  $\text{Pd}_{0.3}\text{Ni}_{0.7}$  in the present case consists of a rather large amount of nickel - to ensure that the magnetic properties prevail - and only a comparably small amount of palladium for the wetting properties. It should be mentioned that there has been a discussion about the exact magnetic properties of this material for a considerable time now [56, 57, 99, 100] which in some sense has found its conclusion now in the extensive investigation of [58].

The main result from this work is that the macroscopic magnetization behaves more complicated than naively expected. As an example, for thin mesoscopic stripes with typical dimensions of  $d = 50\text{ nm}$ ,  $l = 5\text{ }\mu\text{m}$ , and  $w = 100\text{ nm}$  to  $900\text{ nm}$  it was shown that there is a uniaxial anisotropy *perpendicular* to the long axis. The domain structure that has been found in, e.g., magnetic force microscopy measurements is such that the magnetization alternates in stripes along the long axis of the strip. The exact domain structure seems to depend on the substrate on which the alloy is deposited. Strain building up between the deposited structures and the substrate during the condensation does not relax equally along the defined structure.

Magnetic fields present during the evaporation alter the final domain structure considerably. All these points are potential reasons for the difficulty to reproduce results when measuring the tunneling magnetoresistance.

The main results of work presented here in this thesis however are not relying on an exact evaluation of the micromagnetic structure of the sample but rather on generic parameters that define the band structure. Three parameters of the ferromagnetic alloy are of central importance, the magnetization  $\mathcal{M}$ , the polarization  $\mathcal{P}$ , and the filling fraction of the bands  $\mathcal{F}$ , cf. equations 4.27 and 4.16. The magnetization as defined in chapter 4 will be derived from experimental investigations. The polarization of  $\text{Pd}_{0.3}\text{Ni}_{0.7}$  is a parameter that varies strongly throughout the literature. Depending on the method of determining the polarization the given values range from roughly 10% to more than 20% [13, 96]. In addition, for estimating the polarization *ab initio* calculations were performed by S. Mankovsky. The experimental results of this work will later be used to estimate the order of magnitude of the polarization  $\mathcal{P}$  and compare it to the numerical values and those from literature. The *ab initio* calculations also allow a determination of the filling fraction as will be shown below.

Our starting point for determining the magnetization is the investigation by J. C. Ododo in the early 1980s [57]. For a nickel concentration of 70% ( $c = 70$ ) the bulk magnetization or average magnetic moment per atom is given in Ref. [57] as

$$\bar{\mu} = 0.324(c - 2.72)^{0.14} \frac{\mu_B}{\text{atom}} = 0.584 \frac{\mu_B}{\text{atom}}, \quad (5.4)$$

where  $\mu_B = 5.788 \times 10^{-5} \text{ eV T}^{-1}$  is the Bohr magneton. Recalling the definition of the

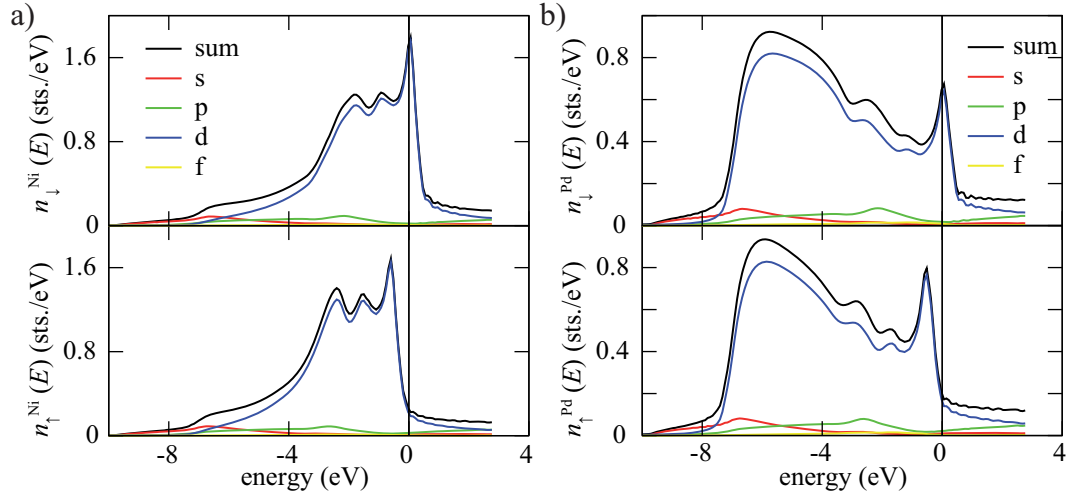


**Figure 5.5.:** Ab-initio calculations (SPR-KKR-ASA) of the band structure of (a) nickel in  $\text{Pd}_{0.3}\text{Ni}_{0.7}$  and (b) palladium in  $\text{Pd}_{0.3}\text{Ni}_{0.7}$ . The upper part of each panel shows the number of states versus energy for the spin-down band while the lower one shows the same for the spin-up band. The images clearly reflect that the dominant contribution to magnetism stems from the  $d$ -bands. S. Mankovsky, private communication.

magnetization as it was given in equation 4.18,

$$\mathcal{M} = \frac{n_{\uparrow} - n_{\downarrow}}{N_a},$$

we can infer the magnetization from equation 5.4. Since the effective magnetic moment per atom is given equation 5.4 in units of the Bohr magneton, the prefactor 0.584 has to result from the different numbers of electrons with up and down spins, i.e.  $n_{\uparrow} - n_{\downarrow}$ , meaning that this factor only needs to be divided by  $N_a$  to get the value of the magnetization.

The magnetic order of band ferromagnets such as Ni is mainly governed by correlation effects in the narrow  $3d$ -bands. Since the number of states for a  $d$ -band is 10 the number of states per atom and spin is simply 5. As a side note, although the magnetization has its origin within the  $d$ -subbands, the electrons from that band do not contribute to the transport due to their strong spatial confinement. It is rather the  $s$ -electrons that carry the transport current. Their finite spin polarization comes from exchange effects with uncompensated magnetic moments of the localized  $d$ -electrons [53]. This allows to conclude a value for the magnetization which is

$$\boxed{\mathcal{M} = \frac{0.584}{5} = 0.117.} \quad (5.5)$$

The literature value of  $0.584 \mu_B/\text{atom}$  can be backed up by measurements of the magnetic moment with a superconducting quantum interference device (SQUID). Such measurements have been carried out within the diploma thesis of Daniel Steininger in the group

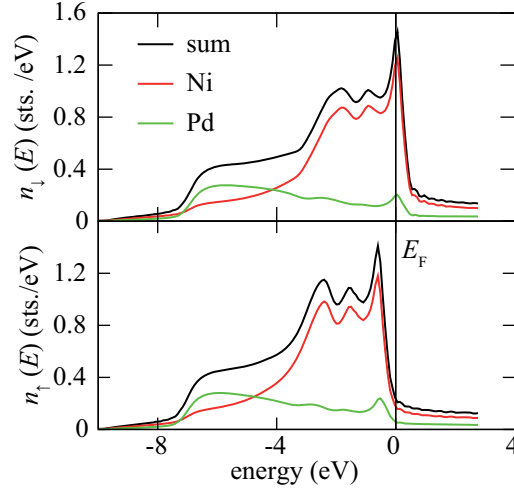


**Figure 5.6.:** Combined band structure for  $\text{Pd}_{0.3}\text{Ni}_{0.7}$ . The number of states as a function of the energy is shown for both spin directions separately.

of Prof. Christoph Strunk in cooperation with the magnetic research group of Prof. Christian Back [101]. The result of this SQUID measurement was an absolute value for the magnetic moment of

$$\mu = 2.5 \times 10^{-5} \text{ emu} = 3.5 \times 10^{-8} \text{ A m}^2.$$

The volume of the material for which this magnetic moment was measured amounts to  $V = 54 \times 10^3 \mu\text{m}^3$ . With this the magnetization can be inferred by dividing the magnetic moment  $\mu$  by  $V$  which results in a value of

$$M = \frac{\mu}{V} = 463 \times 10^3 \text{ A m}^{-1}.$$

Expressing this in terms of the Bohr magneton  $\mu_B$  yields

$$M = 463 \times 10^3 \text{ A m}^{-1} = \mu_B \cdot 4.98 \times 10^{22} \text{ cm}^{-3}.$$

Taking the average density of the  $\text{Pd}_{0.3}\text{Ni}_{0.7}$  alloy as

$$0.3\rho_{\text{Pd}} + 0.7\rho_{\text{Ni}} = 8.5 \times 10^{22} \text{ atoms/cm}^3$$

this can be converted into a magnetization or a magnetic moment per atom. The final result is then

$$M = 0.586 \frac{\mu_B}{\text{atom}}.$$

This is in excellent agreement with the literature value, which is going to be taken as the value for the magnetization for the later quantitative comparisons between the numerical model and the experiments, cf. chapter 7.

Ni	DOS( $E_F$ )	NOS	$P_{\text{spin}}$	$\mu_{\text{spin}}$
s	0.2548	0.6530	0.0664	-0.0038
p	0.6005	0.7582	0.0739	-0.0210
d	24.3991	8.5606	-20.3647	0.7499
f	0.1290	0.0971	-0.0923	-0.0010
sum	25.3833	10.0688	-20.3168	0.7241

**Table 5.1.:** Numerical values resulting from ab initio calculations for nickel in  $\text{Pd}_{0.3}\text{Ni}_{0.7}$ . DOS( $E_F$ ) denotes the density of states at  $E_F$ , NOS the number of valence electrons at atom Ni,  $P_{\text{spin}}$  the spin polarization at  $E_F$ , and  $\mu_{\text{spin}}$  the spin magnetic moment. S. Mankovsky, private communication.

Pd	DOS( $E_F$ )	NOS	$P_{\text{spin}}$	$\mu_{\text{spin}}$
s	0.2129	0.5980	0.0537	-0.0056
p	0.5143	0.6593	0.0501	-0.0195
d	10.2643	8.4606	-6.4170	0.2487
f	0.1580	0.1216	-0.1120	-0.0016
sum	11.1495	9.8395	-6.4252	0.2220

**Table 5.2.:** Numerical values resulting from ab initio calculations for palladium in  $\text{Pd}_{0.3}\text{Ni}_{0.7}$ . Otherwise the notation is the same as in table 5.1. S. Mankovsky, private communication.

The second parameter that is required from the sample properties is the filling factor or filling fraction  $\mathcal{F}$  of the bands, i.e. the fraction of the band that is filled just as defined in figure 4.8 (a). Access to this value can be gained through ab-initio calculations. Such calculations for the desired composition of palladium and nickel have been carried out by S. Mankovsky. The results are summed up in figures 5.5 and 5.6 as well as in tables 5.1 and 5.2. The filling fraction corresponds to the number of valence electrons per one atom of nickel or palladium [cf. column labeled NOS in tables 5.1 and 5.2]. Again this is done for the  $d$ -band exclusively. The ratio of this number and the total number of states, 10 for the  $d$ -band, then determines the filling fraction. For the alloy, one has to account for the different material concentrations. In the case of  $\text{Pd}_{0.3}\text{Ni}_{0.7}$  the filling fraction is given by

$$\mathcal{F} = 0.3 \times \frac{8.46}{10} + 0.7 \times \frac{8.56}{10} = 0.853. \quad (5.6)$$

Finally with the same reasoning one can also use the values for the sum of the single band contributions in tables 5.1 and 5.2 to estimate a value of the polarization  $\mathcal{P}$ . The

parameter  $P_{\text{spin}}$  denotes the spin polarization at  $E_F$ ; forming the weighted sum of the two values for Pd and Ni one finds

$$\mathcal{P} = 0.3 \times (-6.43\%) + 0.7 \times (-20.32\%) = -16.2\%. \quad (5.7)$$

The minus sign indicates a peculiar property of  $\text{Pd}_{0.3}\text{Ni}_{0.7}$  that it inherits from pure nickel, namely that the density of states at the Fermi energy is larger for the minority spin. Note that also the spin magnetic moment  $\mu_{\text{spin}}$  from tables 5.1 and 5.2 can be used to once more derive a value for the overall magnetic moment which gives

$$\mu_{\text{spin}}^{\text{tot}} = 0.7 \times 0.7241 + 0.3 \times 0.222 = 0.573.$$

This value again agrees very well with both previously mentioned values from literature and from SQUID measurements.

### 5.3. Experimental methods

This section briefly summarizes the experimental methods necessary for the presented transport experiments in two parts. In chapter 3 low temperatures were mentioned as one of the crucial necessities to observe single electron tunneling in nanostructures, consequently the first part describes the equipment used to generate low temperatures. The second part of the present section describes the actual electrical scheme with which the transport measurements were carried out.

#### 5.3.1. Low temperatures

For the purpose of generating low temperatures a  $^3\text{He}/^4\text{He}$  dilution refrigerator of the type Air Liquide Minidil is employed. The cooling mechanism relies on the fact that there is an incomplete phase separation between  $^3\text{He}$  and  $^4\text{He}$  below  $T \approx 870 \text{ mK}$  in the sense that the content of  $^3\text{He}$  in  $^4\text{He}$  does not become zero even down to the lowest temperatures. While the  $^3\text{He}$ -rich phase eventually becomes pure  $^3\text{He}$ , it turns out that the minimal concentration of  $^3\text{He}$  in  $^4\text{He}$  is 6.6%. The actual cooling then is often compared to evaporative cooling, only that the evaporation does not take place from a liquid into a gaseous phase but from the  $^3\text{He}$ -rich liquid phase into the  $^3\text{He}$ -poor liquid phase. However, this only gives a crude picture of the real cooling mechanism which relies on the mixing enthalpy of two quantum liquids [102, 103].

In the state where there is already liquid mixture of  $^3\text{He}$  and  $^4\text{He}$  present, the operation principle is that  $^3\text{He}$  gas is pumped into the system from room temperature. Through several heat exchangers the gas is pre-cooled and finally condensed at about  $T \approx 1.5 \text{ K}$  by e.g. a Joule-Thomson expansion stage or a 1 K-pot. Through several more heat exchangers





**Figure 5.7.:** Photographs showing different views of the dilution refrigerator measurement setup. (a) Overview, showing the copper shield which completely surrounds the low temperature part. (b) Dewar with the dilution system inserted. (c) Dilution system without vacuum shields.



and flow impedances the now liquid  $^3\text{He}$  enters the *mixing chamber* such that it is added to the pure  $^3\text{He}$  phase that floats on top of the heavier  $^4\text{He}$ -rich phase or, from point of view of the  $^3\text{He}$ , the diluted phase. Another tube connects this diluted phase with the *still* where the concentration of liquid  $^3\text{He}$  is less than 1%. The still is heated to a temperature at which  $^3\text{He}$  and  $^4\text{He}$  have very different vapor pressures so that almost exclusively  $^3\text{He}$  evaporates; the typical concentration of  $^3\text{He}$  in the vapor above the diluted phase is  $> 90\%$ . This almost pure  $^3\text{He}$  gas is pumped away and re-enters the system at the starting point to complete the cycle. The fact that  $^3\text{He}$  is continuously extracted from the dilute phase together with the fact that the concentration of  $^3\text{He}$  in  $^4\text{He}$  can not decrease to below 6.6% causes  $^3\text{He}$  from the pure  $^3\text{He}$  phase in the mixing chamber to cross the phase separation line. This constant mixing of  $^3\text{He}$  and  $^4\text{He}$  creates cooling power.

The used system is completely shielded by a massive copper construction [see figure 5.7(a)] to prevent electromagnetic and acoustic noise. In order to lower also the noise level and the effective electron temperature as far as possible the electrical connections from room temperature are filtered and thermally anchored several times. The first filter stage is made up of  $\pi$ -filters at room temperature with an efficient attenuation for radio frequencies. Additionally, two sets of copper powder filters at  $T = 1\text{ K}$  and  $T = 100\text{ mK}$  provide a cutoff frequency around 500 MHz [see figure 5.7(c)].

The whole dilution system is fitted into a dewar with a sliding seal [see figure 5.7(b)]. The dewar is equipped with a superconducting magnet for fields up to 8 T. With this system typically bath temperatures of  $T = 25\text{ mK}$  can be reached. By mounting a Coulomb blockade thermometer in the sample holder the efficiency of the thermal filtering of the current lines could be tested and an effective electron temperature of 30 mK was estimated.

### 5.3.2. Transport measurements

The setup for electrical measurements is a straightforward two point geometry resistance measurement, i.e. two contacts to the nanotube are connected and current is measured as function of the applied bias voltage [cf. figure 5.8]. The reason for structuring four contacts, as shown in figure 5.3, is to increase the chance of a low resistance connection. This is, however, not a limitation, as a four point measurement is mainly beneficial when the sample resistance is on the same order as the resistance of the leads. In the case of Coulomb blockade, typical sample resistances are  $\gg 6\text{ k}\Omega$  and the resistance of the leads, which is on the order of  $\sim 100\Omega$ , can be neglected. One of the two connections is used to apply a bias voltage from a voltage source. In the present case a Yokogawa 7651 dc voltage source is connected through a voltage divider (typically  $\times 10^{-3} - 10^{-5}$ ) to one of the contacts. One of the neighboring contacts is then connected to a current to voltage amplifier, usually of the make DL Instruments 1211. Sensitivity and rise time of the amplifier are typically set to  $10^{-8}\text{ A V}^{-1}$  and 300 ms, respectively. The back-gate potential is set by connecting another Yokogawa 7651 dc voltage source through a high

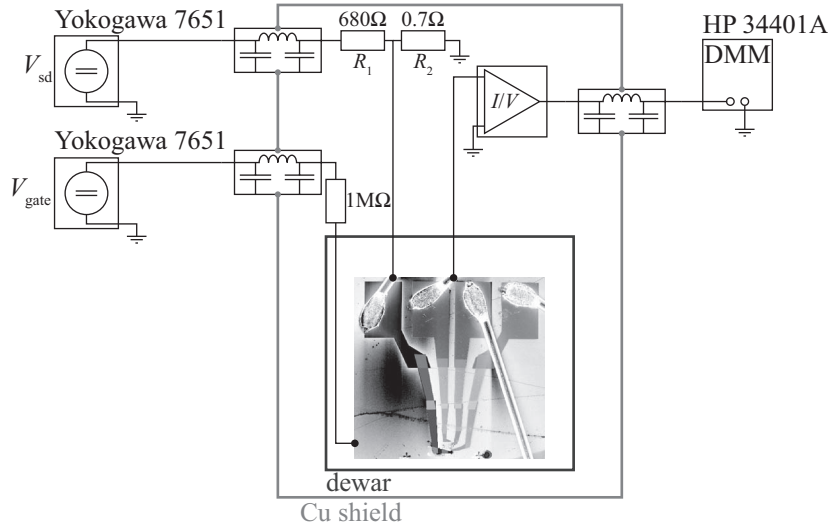


**Figure 5.8.:** Simplified measurement schematic. The Cu shield usually serves as anchoring point for all ground potentials. Connections are fed through the Cu shield by  $\pi$ -filters. The bias voltage  $V_{sd}$  is divided by a factor  $\sim 1000$ . The connection to the back gate is protected by a large resistor of typically  $1\text{ M}\Omega$ . The current through the device is converted by an amplifier into a voltage which is finally picked up by a digital multimeter.

resistor of typically  $1\text{ M}\Omega$ . The resistor is placed for protection of the sample from too high currents, e.g. in case of a shortcut through the gate oxide. Additionally, together with the lead capacitance it constitutes a low pass that attenuates high frequency interference.

Summing up, the quantity that is measured is the current  $I$  depending on, e.g., the gate voltage  $V_{gate}$ , the bias voltage  $V_{sd}$ , or the magnetic field  $B$ . Unless noted differently, the current is numerically differentiated with respect to the bias voltage to yield the differential conductance as a function of the gate voltage  $V_{gate}$  and the bias voltage  $V_{sd}$

$$G = G(V_{gate}, V_{sd})$$

or the differential conductance as a function of the magnetic field  $B$  and the bias voltage  $V_{sd}$  (magnetoconductance)

$$G = G(B, V_{sd}).$$

In order to get rid of spurious effects from ground loops every external control device is powered through a separate isolation transformer. The grounding scheme is as far as possible carried out as a “star network”. The main ground point is provided by the copper shield, and every device obtains its ground potential through a short connection to it. The copper shield itself is connected only to the main ground potential of the lab. All additional connections from pumps or meters are electrically isolated or ground-free.

The measurements are automated by controlling the instruments with a computer via the “general purpose interface bus” (GPIB). For this purpose Lab::VISA (now

Lab::Measurement), a suite of device drivers written in Perl was used. This suite was started in Munich by D. Schröder and adapted in Regensburg by A. Hüttel, D. Kalok, and F. Olbrich. A measurement is performed by running a simple Perl script that calls functions from the package, thereby, e.g., executing voltage sweeps and reading out multimeter values. The advantage of this method is that it is highly modular - any type of measurement can be freely designed by such scripts. An example for a simple  $I(V)$  measurement is listed and briefly explained in appendix B.

Before measurements are conducted at the lowest temperatures it is advisable to thoroughly test the samples already at room temperature in terms of the conductance through the device as well as potential leakage of the gates through the oxide. The sample is then glued into a chip carrier and mounted at the cold stage of the dilution refrigerator. At 4.2 K, before the  $^3\text{He}/^4\text{He}$ -mixture is injected, the same test routine is carried out again. These two sets of measurements can already contain valuable information about whether the device behaves metallic or semiconducting. If the conductance in terms of the gate voltage,  $G(V_{\text{gate}})$ , does not vary much over the accessible gate range the nanotube is assumed to be metallic; if a zero-conductance gap is observed, the nanotube is semiconducting. The results of these characterization measurements and all following experimental investigations will be discussed in the next chapters.

## 6. Electronic sample characterization

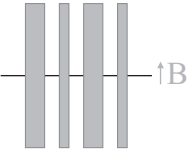
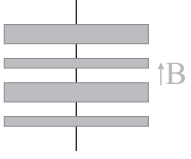
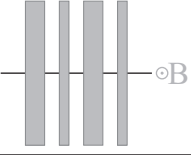
In this chapter an overview of the determination of important electrical properties of the samples is given. In the first section the level spectrum is derived from an evaluation of spectroscopy data and the values for the charging energy  $U$ , the level spacing  $\Delta$ , and the subband mismatch  $\delta$  are given. The second section deals with the estimation of the coupling strength between the nanotube and the leads as well as of the asymmetry between the coupling strength to source and drain contact.

### 6.1. Sample classification

In this brief section the different samples and measurement runs are shortly summarized. The measurements were performed on two samples, AC and BA, from two different preparation runs [cf. table 6.1]. The difference between the two samples is that the ferromagnetic alloy for sample AC was prepared in house in a custom built annealing oven with a mass ratio of 3 : 7 which, converted into a stoichiometric ratio, rather corresponds to  $\text{Pd}_{1-x}\text{Ni}_x$  with  $x = 0.8$  instead of  $x = 0.7$ . For sample BA a custom made pellet of alloy with the desired ratio was used for evaporation.

In the first measurement campaign sample AC was cooled down twice with a magnetic field orientation in the plane of the contacts and perpendicular to the tube axis. The second measurement campaign consisted of a total of three cool down runs of sample BA differing only in the orientation of the external field with respect to the sample plane. Two runs were carried out with an in-plane orientation while one had an out-of-plane orientation. In the in-plane situations the magnetic field was aligned parallel to the tube axis.

In the course of this work two more sets of samples have been produced. Sample AA before and sample BB after the two main samples mentioned above. Sample AA features pure nickel electrodes. Sample BB has only two contacts that are aligned parallel to the tube axis. This was thought to give the possibility to align the magnetic field in the direction of the easy axis of the contacts while still being perpendicular to the tube axis.

sample	cooldowns	field orientation
AC	2	
BA	2	
BA	1	

**Table 6.1.:** This table schematically shows the external field orientation relative to the carbon nanotube axis and the magnetic contacts for the different measurement runs and samples.

## 6.2. Determination of the level spectrum

The basic starting measurement is recording the conductance  $G$  versus the gate voltage  $V_{\text{gate}}$ . This allows to determine whether the specific nanotube is metallic or semiconducting. At lower temperatures where Coulomb blockade sets in, the gate traces allow to select regular areas with promising conductance. Additionally, the charging energy, the level spacing, and the subband mismatch can all be determined from such a zero bias gate trace of the conductance after a characteristic scaling parameter  $\alpha$  has been determined which allows to translate the gate voltage scale into an energy scale. Figures 6.1 and 6.2 show examples of such measurements. Note that these gate traces are recorded in dc with a small forward bias voltage. At the higher temperatures typically a bias value of 1 mV is used, while at lower temperatures the bias is chosen at about 50  $\mu\text{V}$ .

The conductance axes in figure 6.1 have been scaled to  $4e^2/h$  which is theoretically the highest possible value for a four channel conductor. This value is not nearly reached which is likely due to the interface resistance between electrodes and nanotube. In figure 6.1 the conductance of sample BA is measured over the whole experimentally accessible gate voltage range at different temperatures. At room temperature [figure 6.1(a)] the conductance only weakly depends on gate voltage. No band gap is observed, meaning that the tube is metallic. The inset of figure 6.1(a) shows an measurement of the current versus the

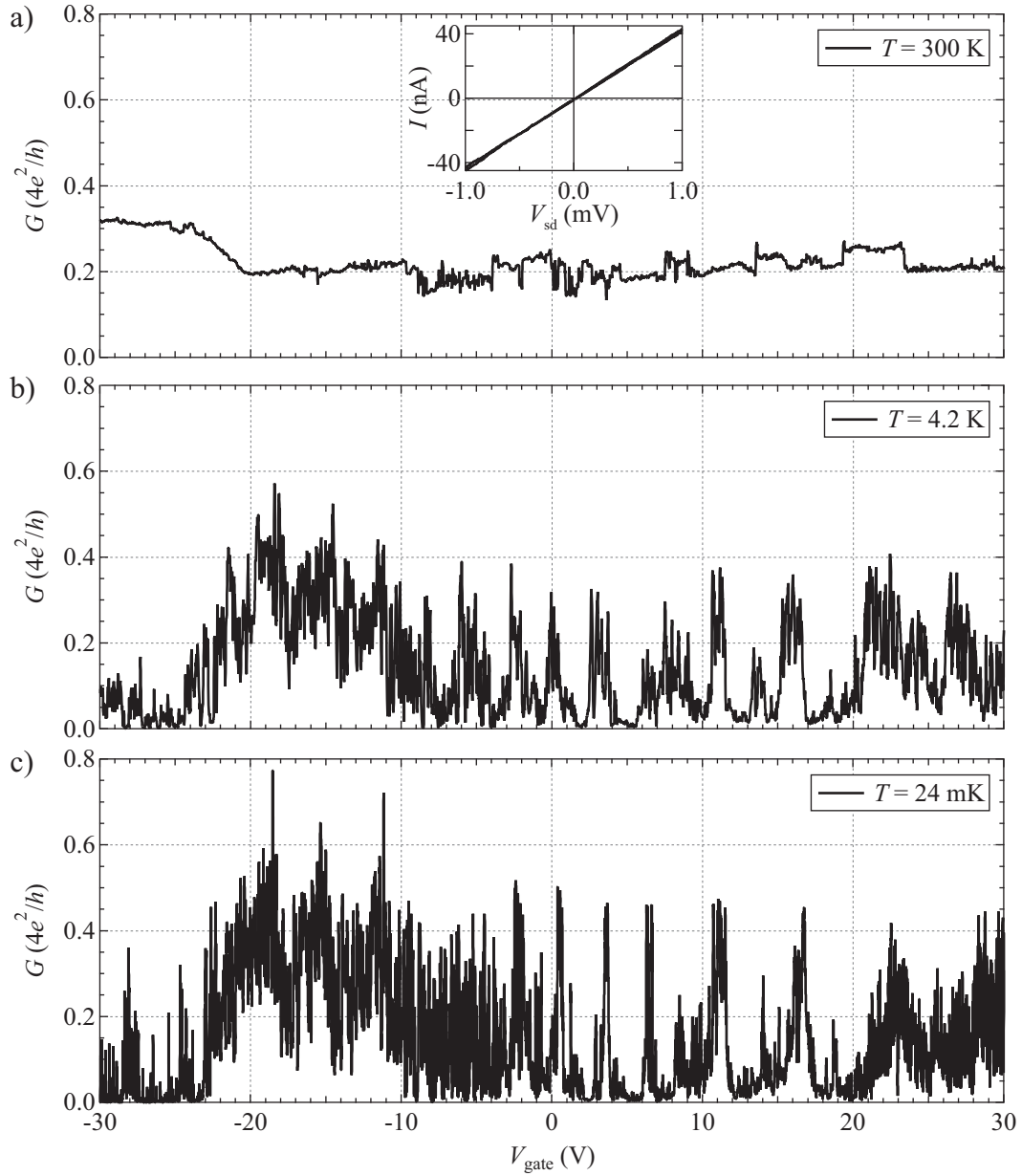


**Figure 6.1.:** Linear conductance versus gate voltage at different temperatures to characterize the sample. (a) Conductance versus gate voltage at  $V_{\text{sd}} \approx 0$  and room temperature. The inset shows the linear  $IV$ -characteristic at  $V_{\text{gate}} = 0$  which agrees with the conductance value that is shown. (b) Same data as in (a) at  $T = 4.2$  K. The conductance now displays clear signs of Coulomb blockade. (c) Same data as in (a) at  $T = 25$  mK. The small increase of the peak height compared to (b) possibly indicates the transition from temperature broadened to life-time broadened peaks (see text for details).

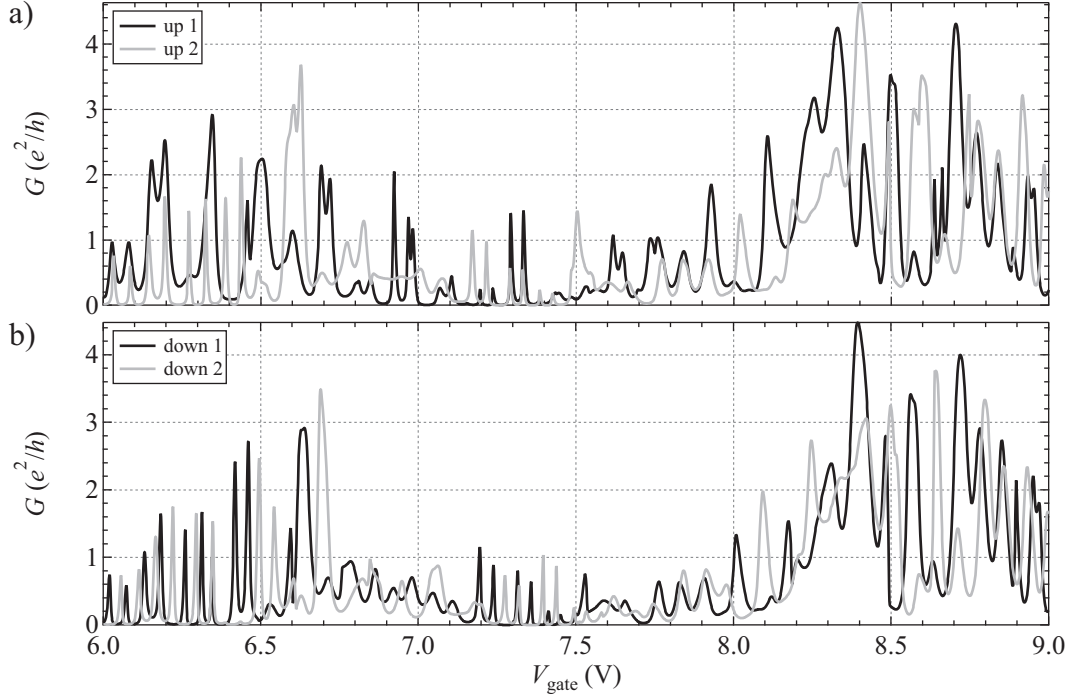


**Figure 6.2.:** Linear conductance at  $T = 25 \text{ mK}$  for  $V_{\text{gate}} = 6 \text{ V}$  to  $9 \text{ V}$ . (a) Conductance for two consecutive sweeps from  $V_{\text{gate}} = 6 \text{ V}$  to  $9 \text{ V}$  (i.e. “up-sweeps”). (b) Conductance for two consecutive sweeps from  $V_{\text{gate}} = 9 \text{ V}$  to  $6 \text{ V}$  (i.e. “down-sweeps”).

source-drain voltage at  $V_{\text{gate}} = 0$ . The value of the conductance determined from the inset is  $G \approx 80 \text{ nA} / 2 \text{ mV} = 40 \mu\text{S} \approx 0.25 \times 4e^2/h$ , agreeing well with the value read off from the gate trace. At lower temperatures in figures 6.1(b) and (c) the behavior of the conductance changes drastically. Already at  $T = 4.2 \text{ K}$  charging effects dominate the conductance and give rise to Coulomb oscillations. When the gate voltage is swept over such a wide range the Coulomb oscillations appear very irregular. This is among other things due to charge traps in the gate oxide and the fast variation of the gate potential which give rise to sudden jumps in the effective potential and hysteretic effects. The behavior of the conductance at base temperature,  $T = 25 \text{ mK}$ , of the system does not change much compared to the situation at  $4.2 \text{ K}$ . On this scale the most obvious change is the slight increase of the average peak height. This indicates the transition from temperature broadened ( $\hbar\Gamma \ll k_B T$ ) to life-time broadened quantum peaks ( $k_B T \ll \hbar\Gamma$ ), cf. equations 3.17 and 3.19.

Figures 6.2(a) and (b) show the conductance versus  $V_{\text{gate}}$  in a much smaller gate voltage range. The figure compares two consecutive sweeps from  $6 \text{ V}$  to  $9 \text{ V}$  with each other and at the same time with two sweeps in the opposite direction. While the traces already appear much more regular than when measured over the full gate voltage range, still considerable deviations between the single traces are observed. There is rarely a feature that can be



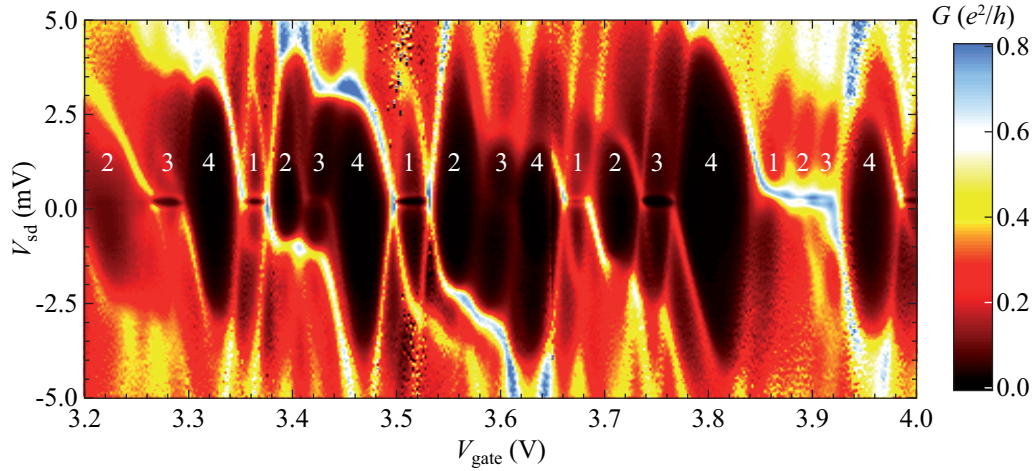


**Figure 6.3.:** Differential conductance versus gate voltage and source-drain voltage  $G(V_{\text{gate}}, V_{\text{sd}})$  for sample AC at  $T = 80$  mK. Regular charging according to the four fold symmetry is clearly visible. Numbers indicate the corresponding relative number of charges on the quantum dot. Note the recurring feature that the conductance for charge states 3 and 4 is weaker, indicating an overall weaker coupling of the corresponding part of the wave function.

found at approximately the same gate voltage position in all four traces. In the displayed example of figure 6.2(b) the voltage range from 7.2 V to 7.5 V shows potentially interesting and fairly regular peaks. Similar features are seen in the traces from the opposite sweep direction in (a). The method of choice now is to slowly restrict the gate voltage more and more approaching the desired range while always checking that the regular oscillations are still within the measured range. This should minimize sudden fluctuations of the gate potential by charge traps. This cautious procedure of course makes comparing different magnetic field orientations practically impossible, as changing the field orientation requires to fully warm up to room temperature to rotate the sample and then cool down again.

With such a gate voltage region selected the next step is to measure the differential conductance versus the gate voltage and the source-drain voltage,  $G(V_{\text{gate}}, V_{\text{sd}})$ . An example of such a stability diagram is shown in figure 6.3, displaying the well known pattern of Coulomb diamonds that was already introduced in chapter 3. In contrast to figure 3.6, however, here the differential conductance is plotted instead of the current. The steps of current every time a new transport channel becomes available show up as lines in this case.

This regular pattern allows to determine the characteristic electronic properties of the sample as already sketched in chapter 3. Before coming to the evaluation of the electrical parameters of the sample figure 6.3 already allows to state the main experimental observa-



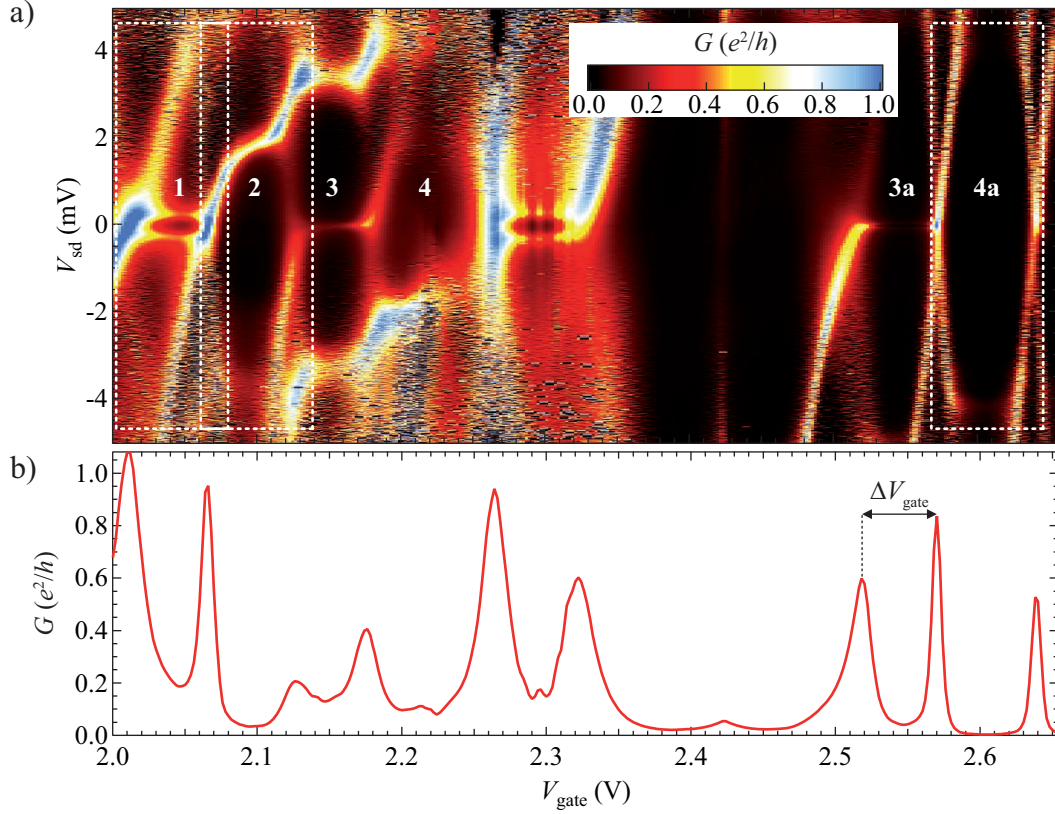


**Figure 6.4.:** (a) Differential conductance versus gate voltage and source-drain voltage  $G(V_{\text{gate}}, V_{\text{sd}})$  of sample BA at  $T = 25$  mK. The white dashed boxes indicate the Coulomb diamonds whose edge slopes have been used to determine the coupling capacitances. The charge state are labeled for later reference. (b) Zero bias gate trace  $G(V_{\text{gate}}, 0)$  of the same gate voltage region used to read off the widths of the Coulomb diamonds (i.e.  $\Delta V_{\text{gate}}$ ).

tions of this work. These are (i) a regular charging pattern, (ii) a four fold symmetry, (iii) a rather strong coupling, leading to broad resonance lines and a variety of higher order processes, (iv) a strong coupling asymmetry between the first two and second two oscillations within a group of four, and (v) the main feature of this investigation, lines of enhanced conductance at small, approximately constant bias values in every second Coulomb diamond. Observation (v) will be of central importance in the following chapter. It will be shown that these lines are conductance resonances brought about by a spin-1/2 Kondo effect, split due to the presence of ferromagnetic contacts. The Kondo effect allows to determine the amount of the underlying tunneling induced level splitting.

In the following we focus on the characterization of the nanotube level structure. Let us consider the charging diagram given in figure 6.4 (a). In an extension of the constant interaction model, there are five different parameters that determine the electronic properties

of a carbon nanotube quantum dot [28, 83, 104]. These five parameters are the charging energy  $U$ , the level spacing  $\Delta\epsilon$ , the sub-band mismatch  $\delta$ , the exchange energy  $J$ , and the excess Coulomb energy  $dU$  as sketched in figure 3.8 and explained in chapter 2.

To determine all five parameters, five distinct features, i.e. peaks in the conductance, in the charging diagram have to be evaluated. Three of these five conductance peaks are connected to ground state transitions and thus normally well visible in transport spectroscopy experiments. The other two are connected to excited states and are only observed in very clean and regular samples with comparably high tunneling barriers. High tunneling barriers in turn means, that transport is dominated by Coulomb blockade and the main feature of the underlying investigation, the Kondo effect, is absent. The energies of transitions involving certain excited states are connected to the values of  $J$  and  $dU$  used in the model explained in 2. In typical experiments these values are rather small compared to the other three (compare [28]). Consequently, we will assume  $J, dU \approx 0$  here due the fact that the coupling in the present situation is so strong that the line widths of the SET lines are too large to resolve the excited states. Thus, from the six expressions given in equation 3.26, only the four relations

$$\begin{aligned}\Delta\mu_1 &= U & \Delta\mu_2 &= U + \delta \\ \Delta\mu_3 &= \Delta\mu_1 & \Delta\mu_4 &= U + \Delta\epsilon - \delta\end{aligned}$$

remain. As seen in figure 3.8 the  $\Delta\mu_i$  are the heights of the separate Coulomb diamonds in terms of source-drain voltage  $V_{sd}$ . These values are often hard to read off from experimental data. This can be because of increasing noise level at higher bias voltages, or the complete absence of the tips because the bias window was chosen too small. However, the conversion factor  $\alpha_{gate}$  introduced in equation 3.25, directly provides the ratio of width (in  $V_{gate}$ ) and height (in  $V_{sd}$ ) of the CB diamonds. The trace  $G(V_{sd} = 0, V_{gate})$  is experimentally accessible and the width of the diamonds can be very accurately read off from the peak distance of the Coulomb oscillation when plotted as a line trace, see figure 6.4 (b). The conversion factor  $\alpha_{gate}$  for the group of Coulomb diamonds depicted in figure 6.4 follows from the slopes  $\lambda_s$  and  $\lambda_d$  as given in equations 3.23 and 3.24, respectively. Following equation 3.25 the results for  $\alpha_{gate}$  for the corresponding Coulomb diamond are summed up in table 6.2.

Note that for diamond “2” the value of the slopes can not be read off from the charging diagram as seen in figure 6.4. For that reason the same value as for diamond “1” was assumed. Due to the vicinity in terms of gate voltage this should be a valid approximation. The charge state labeled by “4” within the same group as the first two diamonds was unfortunately affected by a gate irregularity. Thus, the diamond labeled with “4a” in figure 6.4 was used to determine  $\Delta\mu_4$ . Since this charge state is separated from the others by a larger gate voltage range, the evaluation leading to  $\alpha_{gate}$  was repeated. The result was again obtained by taking the average of the two corresponding slopes and yielded a result of  $\alpha_{gate} = 0.185$ . With these values the distances between the resonances,  $\Delta V_{gate}$ , can now be attributed to energies. This results in

Charge State	$\lambda_s$	$\lambda_d$	$\alpha_{\text{gate}}$
“1”	3	-8.6	0.086
“2”	n/a	n/a	0.086
“4a”	1.9	-3.5	0.185

**Table 6.2.:** Observed CB diamond edge slopes and corresponding gate conversion factors (see text for details). Note that the separate values for  $\lambda$  are the mean values of the respective single slopes.

$$\begin{aligned}\Delta\mu_1 &= U = 4.3 \text{ meV} \\ \Delta\mu_2 &= U + \delta = 5.3 \text{ meV} \\ \Delta\mu_4 &= U + \Delta\varepsilon - \delta = 5.3 \text{ meV},\end{aligned}$$

and the fundamental electrical parameters can be determined as

$U = 4.3 \text{ meV}$
$\delta = 1.0 \text{ meV}$
$\Delta\varepsilon = 9.4 \text{ meV}$

for this specific case of nanotube and  $V_{\text{gate}}$  region.

### 6.3. Coupling strength and asymmetry

For the quantitative comparison between theory and experiment and especially for the numerical calculation of the density of states two additional parameters are required. These are the overall coupling strength  $\Gamma = \Gamma_s + \Gamma_d$  and the coupling asymmetry  $\Gamma_s/\Gamma_d$  between source and drain contact. Both quantities can be determined from stability diagrams as will be demonstrated below.

#### Coupling strength

At the low temperatures present in the dilution refrigerator the thermal broadening of the Fermi function in the leads that is given by the thermal energy  $k_B T = 8.617 \times 10^{-5} \text{ eV K}^{-1} \times 30 \text{ mK} \sim 2.5 \mu\text{eV}$  is very small. Thus it can be neglected and the only process that contributes to the observed width of the quantum dot levels is life time

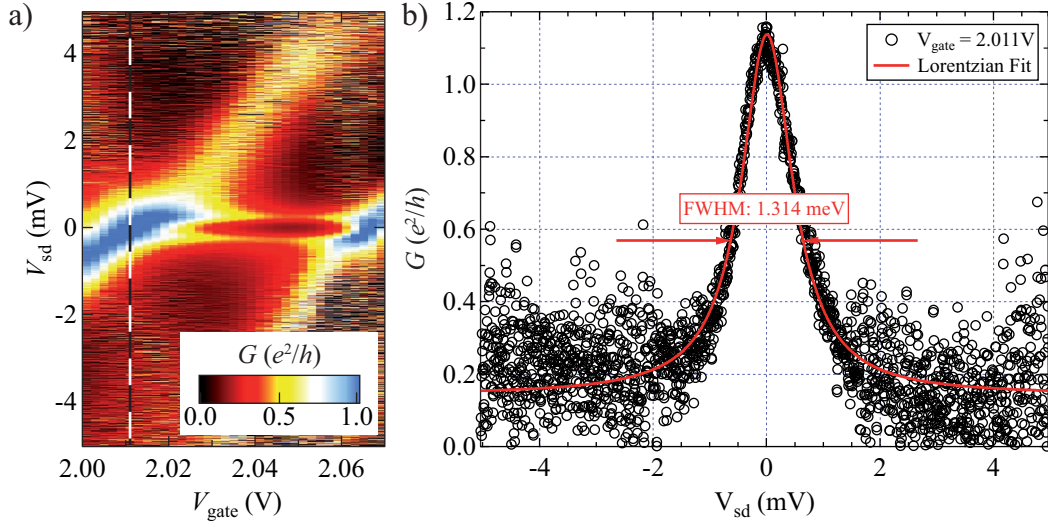


**Figure 6.5.:** (a) Differential conductance  $G(V_{\text{gate}}, V_{\text{sd}})$  again at the same resonance as in figure 6.4 (a); the black and white dashed line marks the gate voltage along which the trace of panel (b) is taken. (b) Conductance peak  $G(V_{\text{sd}})$  at constant  $V_{\text{gate}} = 2.011$  V, i.e. across the resonance point marked in (a). The trace can be fitted to high accuracy with a Lorentzian line shape with a FWHM of 1.3 meV.

broadening due to the tunnel coupling to the reservoirs. In this case the resonance has a Breit-Wigner, i.e. a Lorentzian, line shape given by

$$G_{\text{BW}}(\omega) = G_0 \frac{(\Gamma/2)^2}{(\Gamma/2)^2 + \omega^2} \quad (6.1)$$

where  $\omega$  is the distance from the resonance peak in terms of energy or source drain voltage. Note that in equation 3.18 the line shape was described as a function of the gate voltage. This is equally possible but introduces an additional complication because the width expressed as gate voltage has to be converted into an energy by the conversion factor  $\alpha_{\text{gate}}$ .

The determination of the coupling is shown in figure 6.5, done for the left degeneracy point of charge state “1” of figure 6.4 (a) by fitting it with a Lorentzian line shape. The fitting routine then readily delivers the parameters which set the shape of the Lorentzian. These are the x-coordinate of the peak as well as the FWHM  $2\omega$ . For the given example of figure 6.5 (a) the conductance peak is shown in figure 6.5 (b) together with the Lorentz fit that yields  $\Gamma = 1.3$  meV.

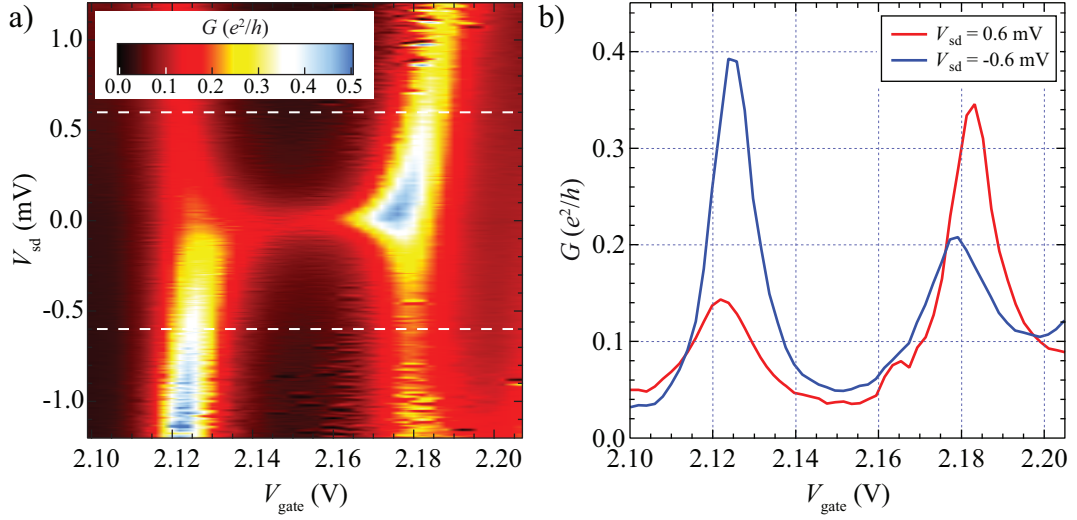


**Figure 6.6.:** (a) Zoom into the region marked as charge state “3” in figure 6.4(a). The asymmetry in the coupling between source or drain contact and the quantum dot, respectively is seen in the different brightness of the lines of enhanced conductance. (b) Conductance along the dashed lines at  $V_{sd} = \pm 0.6$  mV indicated in (a). The value of asymmetry can be estimated best by comparing the peak conductance between source and drain SET line (see text for details). Note that the conductance scale was changed compared to figure 6.4 in order to increase the contrast.

### Asymmetry

With the help of charge state 3 from figure 6.4(a) the determination of the coupling asymmetry is illustrated exemplarily. In chapter 3 and especially figure 3.6 it was shown that the border lines of the Coulomb diamonds can be attributed to the state on the dot being in resonance either with the Fermi level in the source or the drain contact. So, comparing the conductance on an SET line that is caused by a resonance of the dot state with the source contact to the conductance on an SET line which is caused by the resonance to the drain results in the ratio of the coupling strengths. This is demonstrated in figure 6.6 for the above mentioned charge state.

For the estimation of the asymmetry horizontal line cuts at constant source drain voltages are taken in steps of 100 mV as indicated by the dashed line in figure 6.6. The single peak values for each of the line cuts as well as their ratio are listed in table 6.3.

The resulting values illustrate that most of the ratios are reasonably close to 2, which is assumed as the asymmetry of the coupling in the present sample. It should not be concealed that this evaluation was done for just a single charge state. It will turn out however that the assumption allowed to successfully reproduce the experimental results by means of numerical calculations. This will be demonstrated in detail in chapter 7.

$V_{sd}$ (mV)	left peak ( $e^2/h$ )	right peak ( $e^2/h$ )	left/right	right/left
1.2	0.142	0.260	0.543	1.840
1	0.133	0.285	0.466	2.146
0.8	0.139	0.292	0.475	2.105
0.6	0.144	0.346	0.415	2.408
0.4	0.155	0.370	0.417	2.395
0.2	0.176	0.407	0.433	2.311
0	0.203	0.460	0.440	2.271
-0.2	0.265	0.269	0.984	1.016
-0.4	0.322	0.221	1.456	0.687
-0.6	0.393	0.208	1.887	0.530
-0.8	0.408	0.196	2.079	0.481
-1	0.406	0.286	1.422	0.703
-1.2	0.457	0.249	1.832	0.546

**Table 6.3.:** This table shows the ratios of the peak heights for the left and right single electron tunneling lines seen in figure 6.6. The peak values for the two peaks were compared for different values of source drain voltage  $V_{sd}$  and apart from some exceptions lie well in the vicinity of 2. The gray shaded entries indicate the reciprocal values.





## 7. The Kondo splitting and its magnetic field dependence

### 7.1. Splitting of the Kondo resonance

In this section the central experimental observation of this work will be focused on, i.e. the splitting of the Kondo resonance. In the second sections of chapter 4 the theoretically well described influence of magnetic contacts was summarized. To repeat this briefly, the magnetic contacts generate an exchange field by charge fluctuations. The specific scale and potential dependence on gate voltage of this exchange field is governed by the band structure of the ferromagnetic material that is used for the leads. For purely polarized leads with different densities of states at the Fermi energy the expectation is a gate dependent splitting of the levels that is reflected as a crossing of the two Kondo resonances in the center of the Coulomb diamond. For the opposite case of  $\mathcal{P} = 0$  and finite magnetization the expected splitting is practically gate independent for the assumptions explained in chapter 4.

Figure 6.3 of our experimental observations already showed the alternating appearance of a split conductance resonance in every second Coulomb diamond in a wide fraction of the monitored gate voltage range as also did figure 6.4(a). Figure 7.1 now zooms in on charge state “1” of figure 6.4(a).

Two nearly gate-independent lines of enhanced conductance are clearly visible in the Coulomb diamond. The main features, the nearly gate independent splitting and the absence of a crossing of the conductance resonances, allow to relate this image to the one shown in figure 4.12(a) and also the corresponding band structure shown in figure 4.11(a) in chapter 4. The close correspondence of figure 7.1 to figure 4.12(a) is a strong indication that a similar band structure is present. The band structure in figure 4.11 is mainly characterized by a finite Stoner splitting  $\Delta_{\text{St}}$  and only a small difference of the density of states  $\rho_{\sigma}$  for the different spin directions. In the specific case of figure 4.11(a) no extra spin asymmetry was added to the band structure ( $Q = 0$ ). The finite asymmetry is a consequence of the parabolic bands that were assumed. For our flat band model this situation corresponds to  $\mathcal{M} \neq 0$  and  $\mathcal{P} = 0$  and thus does not produce a finite spin asymmetry at the Fermi energy. The experimental observation indicates that the parabolic band structure delivers a more realistic result than simple flat bands. This means at the same time that



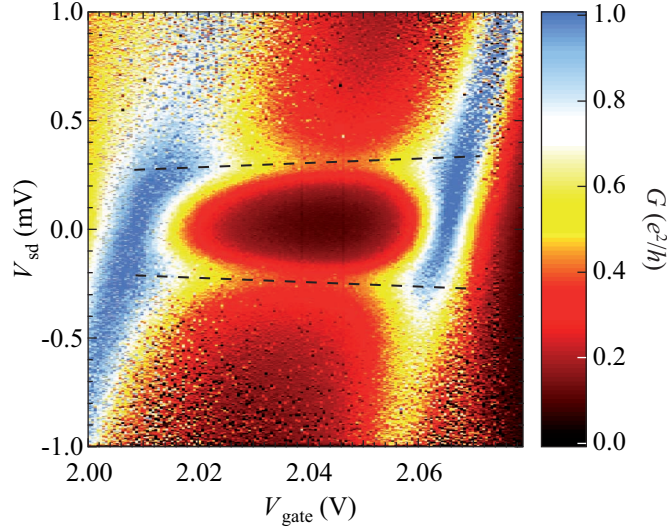


**Figure 7.1.:** Close up of charge state “1” from figure 6.4 sample BA). The observed splitting is clearly only weakly gate dependent and thus closely corresponds to panels (a) both in figure 4.12 as well as in figure 4.11.

for flat bands taking into consideration only the limiting cases  $\mathcal{M} \neq 0$  and  $\mathcal{P} = 0$  versus  $\mathcal{P} \neq 0$  and  $\mathcal{M} = 0$  does not suffice to fully describe the experimental situation. Nevertheless, for a quantitative comparison, the results from the flat band model presented in chapter 4 offer an intriguingly simple approach and thus will still be used for that purpose. This can always be justified by restricting the considerations to the electron-hole symmetric point at the center of the Coulomb blockade diamond where the contribution from a finite polarization to the tunneling induced level renormalization vanishes. Note that the gate voltage dependence of the conductance maxima appears to be very pronounced towards the degeneracy points. The exact position of the conductance resonance and with that also the definite gate voltage dependence is however hard to point at for these gate voltages. Approaching the degeneracy points the polarization induced level shift diverges logarithmically but at the same the Kondo temperature rises, leading to an increase of the width of the conductance peaks.

For the quantitative comparison between theory and experiment figure 7.2(b) shows again a larger  $V_{\text{gate}}$ -range from the same sample. It clearly displays another aspect from the theoretical premises in this experimental situation. At the end of chapter 4 it was emphasized that the size of the tunneling induced splitting is much stronger influenced by the coupling strength and only weakly, i.e. logarithmically, by the Stoner splitting. This becomes obvious when comparing the two split resonances in charge state “1” and “3a” shown in figure 7.2(b). If the splitting of the conductance resonance would be mainly an effect of the Stoner splitting in the leads, the observed splitting should not be so different. The same argument by the way excludes also an effect of an external field. For charge state

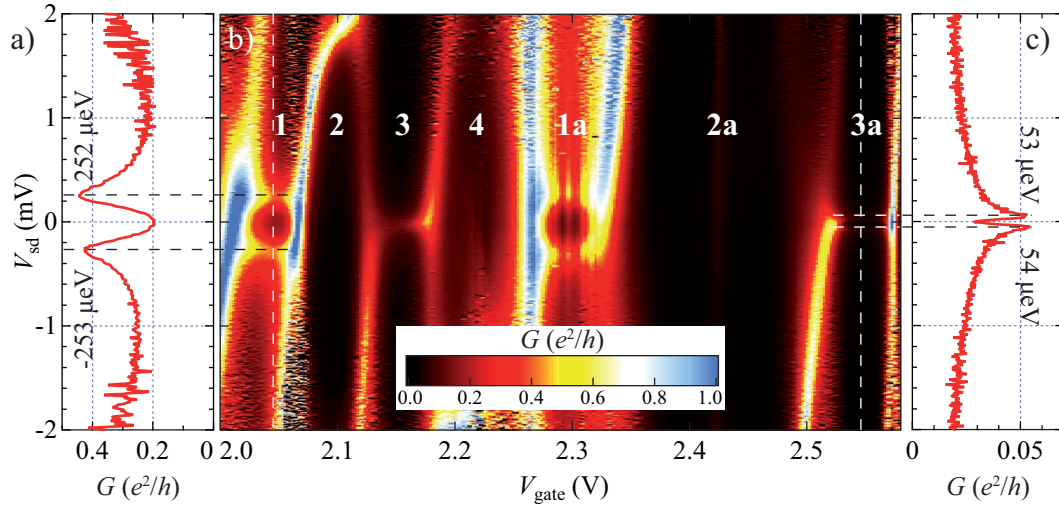


**Figure 7.2.:** (a) Trace of  $G(V_{sd})$  along the dashed white line through the center of Coulomb diamond “1” in (b), i.e. at  $V_{gate} = 2.044$  V. The position of the conductances peaks in terms of  $V_{sd}$  is marked. (b) Differential conductance  $G(V_{gate}, V_{sd})$  at  $T = 25$  mK as already shown in figure 6.4 (a). Conductance resonances appear in every second Coulomb diamond at small but finite bias values symmetric around zero. For the diamond labeled with “3” no splitting is visible. The splitting is much smaller for charge state “3a” compared to “1” and “1a”. (c) Trace of  $G(V_{sd})$  along the white dashed line through charge state “3”, i.e. at  $V_{gate} = 2.546$  V.

“3a” the coupling is much weaker, as can be seen from the value of the conductance at the degeneracy points as well as the brightness of the SET edge lines. The corresponding splitting of the Kondo resonance in this charge state hence is much smaller.

The exact distance of the resonance lines in  $V_{sd}$  can best be read off from line cuts along  $V_{sd}$  at constant  $V_{gate}$ . Such line cuts are shown in figure 7.2(a) and (c) for the charge states “1” and “3a”, respectively. Their position is indicated by the dashed white lines in figure 7.2(b). For resonance “1” the value of the experimentally observed splitting is

$$\Delta\epsilon_{exp} = 252\mu\text{eV} - (-253\mu\text{eV}) = 505\mu\text{eV}.$$

For the case of non-magnetic contacts, it was shown in chapter 4 that a magnetic field causes the zero bias conductance anomaly to split into two peaks at  $V_{sd} = \pm g\mu_B B/e$ . Assuming the splitting to be generated by an effective field, the size of the splitting in terms of  $V_{sd}$  can be related to a magnetic field scale. With a g-factor of  $g = 2$  for carbon nanotubes, the observed splitting of  $505\mu\text{eV}$  then yields an effective magnetic field value of

$$B = \frac{505\mu\text{eV}}{2 \times 2 \times 5.788 \times 10^{-5} \text{ eVT}^{-1}} \sim 2.18 \text{ T}.$$

The large size of this effective magnetic field is another indication, besides the fact that different splittings are observed for different charge states, that a stray field from the magnetic electrodes can be excluded as a source for the splitting. For electrodes of the present size and material typical stray field values of some tens of mT are expected.

Taking the value of the coupling strength  $\Gamma$  for charge state “1” that was inferred in chapter 6 as

$$\Gamma = 1.3 \text{ meV}$$

and the band structure information given in chapter 5 as

$$\mathcal{M} = 0.116 \text{ and } \mathcal{F} = 0.853$$

equation 4.27 yields as theoretical prediction for the renormalization-induced level splitting

$$|\Delta\epsilon^{(\mathcal{M})}| = \frac{1.3 \text{ meV}}{2\pi} \ln \left[ \frac{(1 - 0.116)^2 - (2 \times 0.853 - 1)^2}{(1 + 0.116)^2 - (2 \times 0.853 - 1)^2} \right] = 197 \mu\text{eV}. \quad (7.1)$$

With a splitting of the dot level of that size a conductance resonance due to Kondo correlations is expected at  $V_{\text{sd}} = \pm 197 \mu\text{V}$ , leading to a peak distance of

$$\Delta\epsilon_{\text{theo}} = 2 \times |\Delta\epsilon^{(\mathcal{M})}| = 394 \mu\text{eV}. \quad (7.2)$$

This agrees very well with the experimentally observed value of  $505 \mu\text{eV}$ . The same is true if the analogous evaluation is done for the weakly coupled resonance “3a”. With a coupling strength of  $\Gamma = 0.26 \text{ meV}$ , the results for this charge state then are

$$\Delta\epsilon_{\text{exp}} = 53 \mu\text{eV} - (-54 \mu\text{eV}) = 107 \mu\text{eV}.$$

and

$$\begin{aligned} \Delta\epsilon_{\text{theo}} &= 2 \times |\Delta\epsilon^{(\mathcal{M})}| \\ &= 2 \times \frac{0.26 \text{ meV}}{2\pi} \ln \left[ \frac{(1 - 0.116)^2 - (2 \times 0.853 - 1)^2}{(1 + 0.116)^2 - (2 \times 0.853 - 1)^2} \right] \\ &= 2 \times 39.4 \mu\text{eV} \\ &= 78.8 \mu\text{eV}. \end{aligned} \quad (7.3)$$

The agreement is of the same quality as for charge state “1”. The factor by which the prediction for the strong coupled case is off is  $505/394 = 1.28$  while that for the weak coupled situation is  $107/79 = 1.35$ . This shows that the analytic expression works equally well for charge states with profoundly different coupling strengths. The slight disagreement between theory and experiment can be related to the fact that the flat band structure assumption that led to equation 4.27 might be an oversimplification. However, the parameters of the band structure for the case  $\mathcal{M} \neq 0$  and  $\mathcal{P} = 0$  enter only with a logarithmic

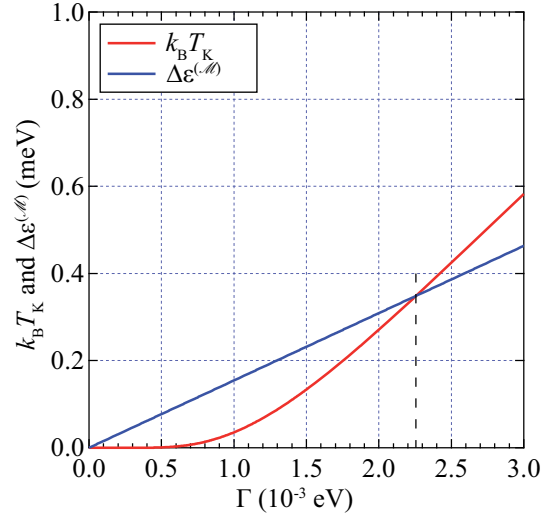


**Figure 7.3.:** Comparison between the absolute values of the Kondo temperature  $T_K$  and the exchange splitting  $\Delta\epsilon^{(\mathcal{M})}$  as predicted by the analytic formulas, cf. equations 4.2 and 4.27. It is immediately recognizable that below a coupling strength  $\Gamma$  of about 2.3 meV the exchange splitting is always larger than the Kondo temperature.

weight. The far more important parameter is the coupling strength, which can be determined from a Lorentz fit with an accuracy of  $\pm 20\%$  as demonstrated in chapter 6.

An exception from this otherwise very conclusive picture is seen in charge state “3” in figure 7.2 where the faint resonance that is seen, appears to be not split. Even additional line traces at constant  $V_{\text{gate}}$  through the center of this diamond did only show a single peak. Since the temperature at which the conductance was measured ( $25\text{ mK} \sim 2.2\text{ }\mu\text{eV}$ ) is smaller than any other energy scale in the problem it can not be that the appearance of a single resonance peak is due to temperature broadening. Then the only remaining logical explanation in principle would be that the Kondo temperature for this resonance is larger than the tunneling induced level splitting. This way the two Kondo peaks would overlap so much that they would appear as one. The relation between the involved energy scales can be summarized as  $k_B T < \Delta\epsilon^{(\mathcal{M})} < k_B T_K$ . The expressions that describe the Kondo temperature and the exchange splitting can be compared to reveal if this is possible. In chapter 4 these expressions were already given as

$$k_B T_K = \frac{\sqrt{\Gamma U}}{2} e^{\pi\epsilon(\epsilon+U)/\Gamma U} \quad (4.2)$$

and

$$\Delta\epsilon^{(\mathcal{M})} = \frac{\Gamma}{2\pi} \ln \left[ \frac{(1 - \mathcal{M})^2 - (2\mathcal{F} - 1)^2}{(1 + \mathcal{M})^2 - (2\mathcal{F} - 1)^2} \right]. \quad (4.27)$$

Adding the experimental parameters as determined in the previous chapters,  $U = 4.3 \text{ meV}$ ,  $\mathcal{M} = 0.116$ , and  $\mathcal{F} = 0.853$ , both expressions can be plotted as functions of  $\Gamma$ . This allows to determine graphically at which size of  $\Gamma$  one or the other energy scale dominates. The plot is shown in figure 7.3 displaying the crossing point of the Kondo temperature  $T_K$  and the exchange splitting  $\Delta\epsilon^{(\mathcal{M})}$  at a coupling strength of  $\Gamma \sim 2.3 \text{ meV}$ . This is consistent with the observation of the splitting in resonance “1” since the coupling strength there was estimated to be  $1.3 \text{ meV}$ . However, for even smaller coupling the situation does not change any more. The exchange splitting remains the dominant energy scale and should be observable. For a non-split resonance the energies should be related like  $\Delta\epsilon^{(\mathcal{M})} \lesssim k_B T < k_B T_K$  which means that the finite temperature overcomes the spin splitting but is still smaller than the Kondo temperature so that Kondo correlations are possible. As figure 7.3 shows, such a case is indeed possible for a coupling strength  $\Gamma > 2.2 \text{ meV}$ . However, the average amplitude of the SET lines for resonance “3” compared to “1” is clearly lower so that a higher coupling strength is unlikely. At the same time, also the temperature would have to lie between  $T_K$  and  $\Delta\epsilon^{(\mathcal{M})}$ . For the present set of parameters this would mean a temperature on the order of  $k_B T \sim 400 \mu\text{eV}$  or  $T \sim 4.6 \text{ K}$ , which is unreasonably high.

Two possible explanations remaining for the observation of the non split resonance in charge state “3” are experimental limitations that resulted in resolution problems or other factors limiting the size of  $\Delta\epsilon^{(\mathcal{M})}$ , that are not included in the simple model. However, still the question remains, why either of these speculated explanations should happen only for this specific resonance while, e.g., the one in state “3a” again is well resolved and shows a finite splitting.

## 7.2. Magnetic field dependence

It was already discussed that the size of the resonance line splitting can be translated into a magnetic field via the Zeeman effect. The typical range of magnetic fields that can be attributed to the observed splitting is on the order of  $1 \text{ T}$  to  $2 \text{ T}$ . This order of magnitude is well accessible with the magnet installed in the present low temperature setup. A field of the same size as the attributed effective field should be a distinct point in this field dependence. Note that, as has been pointed out before [see e.g. chapter 5], the orientation of the external magnetic field with respect to the nanotube axis or the contacts did not show a significant influence on the physical features. It is assumed that the magnetization of the contacts always points into the direction of the external field. However for completeness, the sample name can be connected to a specific field orientation via table 6.1.

The differential conductance for the same bias and gate voltage range as in figure 7.1, was measured for several values of an external field but identical bias and gate voltage range. The field in this case was applied parallel to the tube axis in plane with the contacts

(sample BA). The field value is increased in steps of 0.5 T. Already at the first finite field measurement, the contacts are expected to be fully magnetized along the direction of the external field. Coercive fields for this type of material lie typically in the range of 100 mT and in all the experimental data no clear hysteretic switching of the contacts was observed. In this field range also the band structure is not influenced significantly; a typical value of the Stoner exchange field for nickel of 300 meV corresponds to a field value in the range of 2000 T. It can be concluded that any effect of the field has to come from its effect on the level structure on the quantum dot.

In figure 7.4 the corresponding plots of the differential conductance at different field values are shown. From panel (a) to (d) the magnetic field increases in steps of 0.5 T. Comparing figure 7.4 (a) and (b), it is clearly visible that the splitting decreases with increasing field. At  $B = 2$  T in figure 7.4(e) the splitting is exactly compensated and only one conductance peak at  $V_{sd} = 0$  remains. This compensation of the splitting at  $B = 2$  T agrees well with the field value of  $\sim 2.18$  T that was attributed to the splitting in the previous chapter. In anticipation of the origin of the splitting, the field value at which the splitting is compensated will be referred to as  $B_{\text{exch}}$ . As was already mentioned and is visible in figure 7.4(f), at higher fields there is an overcompensation by the external field and the splitting reappears. This close relation between an external field and the splitting of the Kondo resonance is indicative of an explanation for the tunneling induced exchange field as an effective magnetic field. Note that in figure 7.4(e), at the compensation field, additional dotted and dashed lines indicate the contributions that result from a finite polarization of  $\mathcal{P} = 10\%$  for the dotted line and  $\mathcal{P} = 20\%$  for the dashed line. The lines were generated by plotting equation 4.16, i.e.

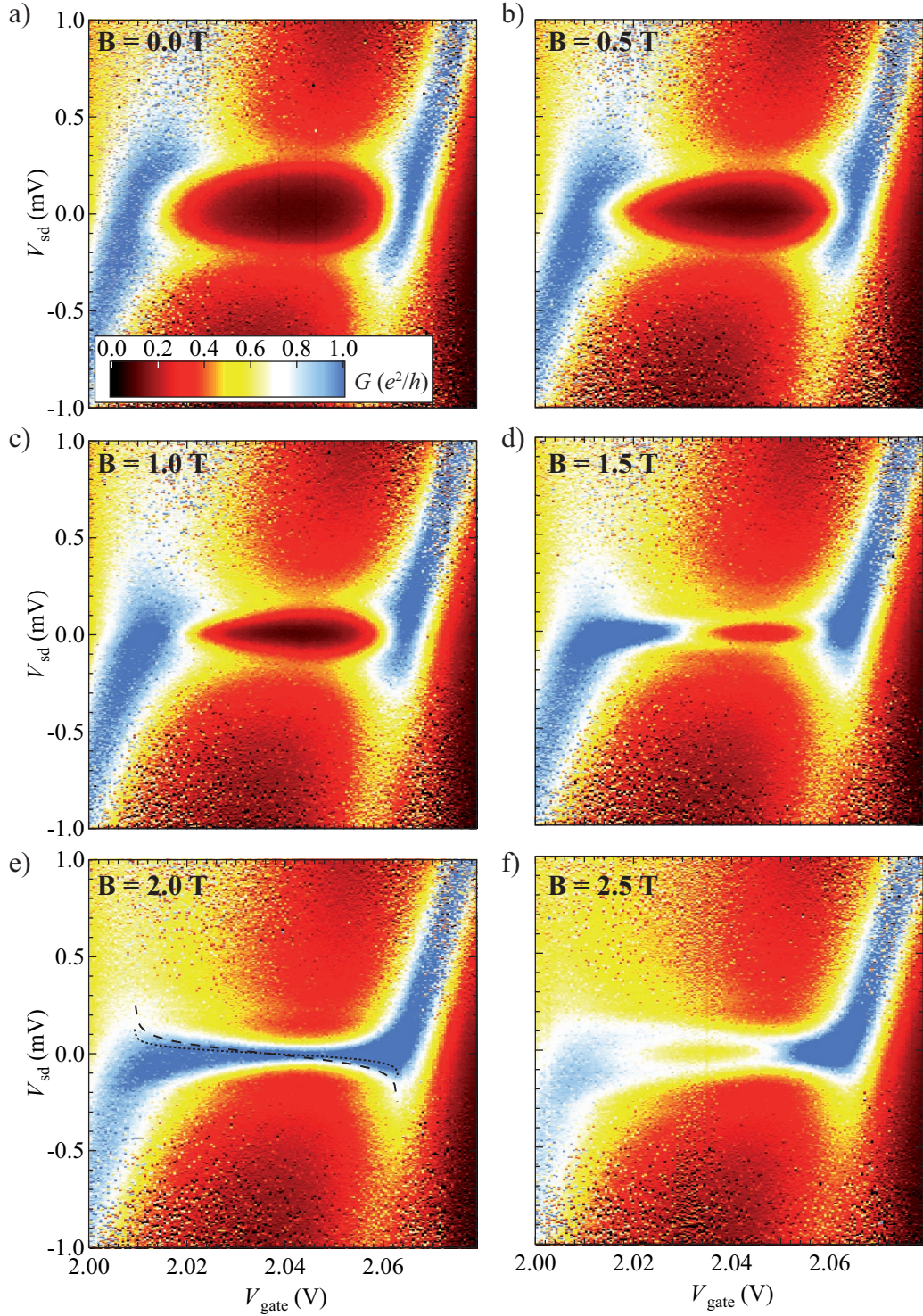
$$\Delta\epsilon^{(\mathcal{P})} = \frac{\mathcal{P}\Gamma}{\pi} \ln \left[ \frac{\epsilon + U}{|\epsilon|} \right],$$

for these values of  $\mathcal{P}$  and  $\Gamma = 1.3$  meV between  $\epsilon = 0$  and  $\epsilon = -U$ . This shows that the estimate of 16% for the polarization using the ab initio data in chapter 6 agrees well with our measurements. Since the external field in this case fully compensates the gate independent contribution from a finite magnetization  $\mathcal{M}$ , the only remaining contribution is the one from the polarization.

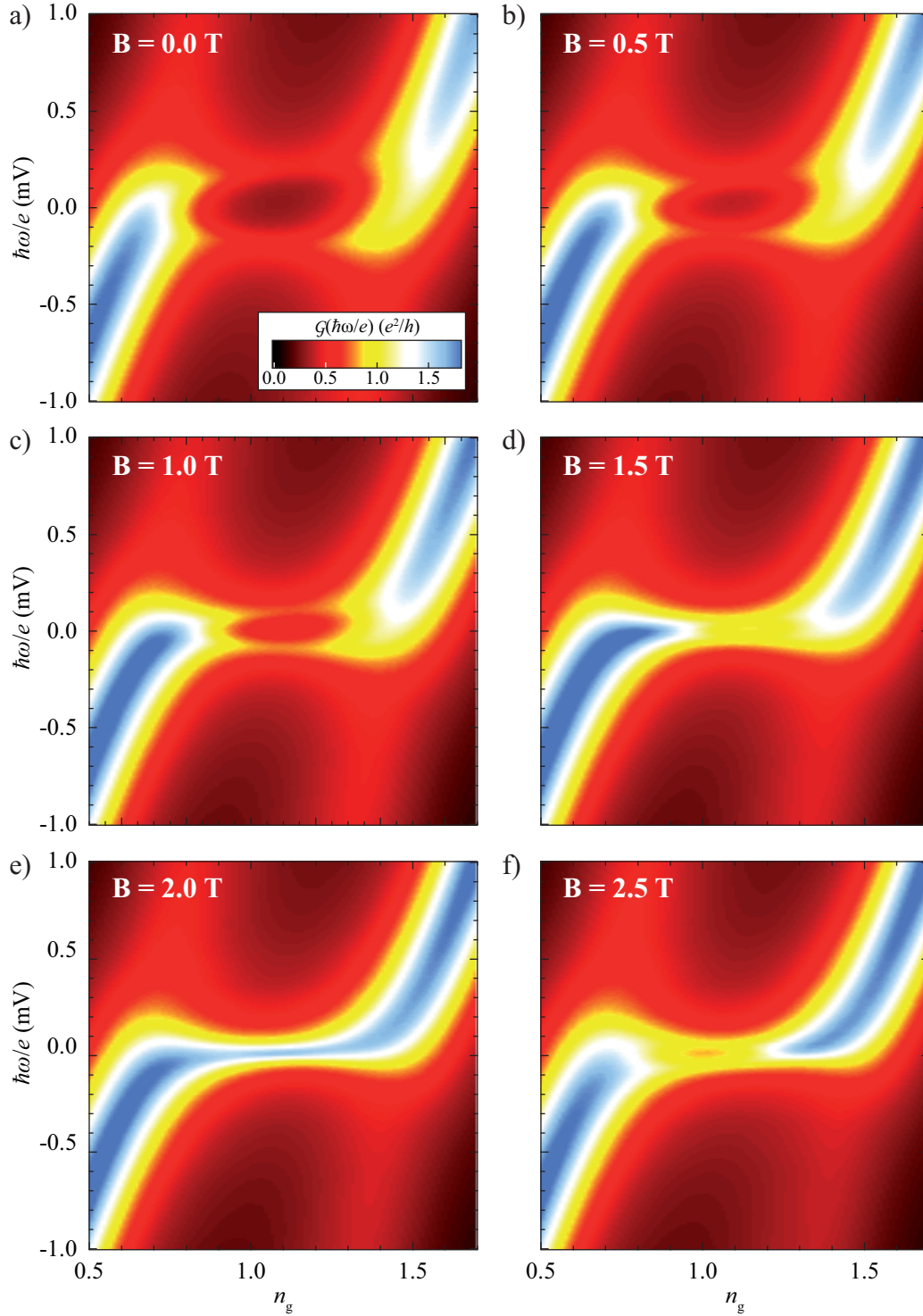
Note that the resemblance between figure 7.4(e) and figure 4.13 is already very good although the numerical calculations were not adapted to the exact experimental situation. The fundamental features, the full compensation of the splitting to a seemingly single resonance and a practically gate voltage independent splitting, were already seen in these earlier calculations. New calculations, carried out with the input of the present experimental parameters, were additionally done and show an even closer match between theory and experiment.

Figure 7.5 shows a numerical renormalization group calculation by I. Weymann as the exact analogue of figure 7.4. It displays the normalized equilibrium zero-temperature spectral function  $\mathcal{G} = \sum_{\sigma} \pi \Gamma_{\sigma}(0) A_{\sigma}(\omega)$  versus the frequency  $\hbar\omega/e$  and the dimensionless





**Figure 7.4.:** Evolution of the split conductance peaks in an external magnetic field for the same resonance as shown in figure 7.1. The plots show the differential conductance in linear color scale, as function of gate voltage  $V_{\text{gate}}$  and bias voltage  $V_{\text{sd}}$ . From (a) to (d) a magnetic field is increased in steps of 0.5 T from 0 T to 2.5 T. All measurements are recorded at a slightly elevated temperature of 100 mK. Note that the splitting is fully compensated in panel (e) for a field of  $B = 2$  T. The dashed and dotted lines in this panel indicate the expected contribution to level shifts from a finite spin polarization of  $\mathcal{P} = 10\%$  and  $20\%$ , respectively. At higher fields (d) the splitting is overcompensated by the Zeeman energy from the external field and increases again.



**Figure 7.5.:** Normalized equilibrium zero-temperature spectral function  $\mathcal{G} = \sum_{\sigma} \pi \Gamma_{\sigma}(0) A_{\sigma}(\omega)$  obtained using the parameters determined from the experimental data, see text. The horizontal axis is the dimensionless gate potential  $n_g = 1/2 - \varepsilon_d/U$ , the vertical axis is the scaled frequency  $\hbar\omega/e$  such that it can be compared to its experimental analogue, the bias voltage.



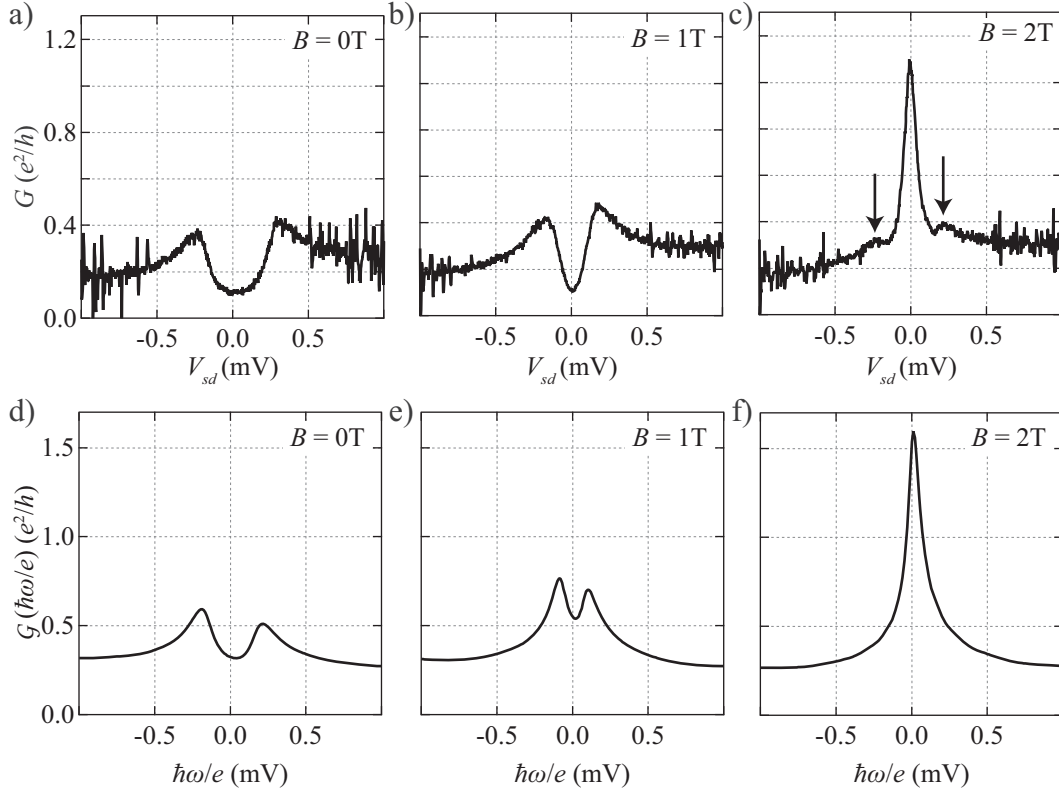


**Figure 7.6.:** Line traces of the conductance respectively the spectral function through the center of the corresponding panels in figure 7.4 and 7.5. (a) to (c) Differential conductance versus  $V_{sd}$  at  $B = 0\text{ T}$ ,  $1\text{ T}$ , and  $2\text{ T}$ . In (c) the two arrows mark two shoulder features appearing at either side of the central maximum at finite fields. (d) to (f) Spectral function versus  $\hbar\omega/e$  at the same finite fields as (a) to (c).

gate potential  $n_g = 1/2 - \varepsilon/U$ . Note that, although the vertical axis is given in units of mV, the quantity that is calculated is an equilibrium quantity. The dimensionless gate potential is expressed such that it runs from  $\varepsilon = 0$  to slightly above  $\varepsilon = -U$ . Thus the electron-hole symmetric point is at  $n_g = 1$  corresponding to  $\varepsilon = -U/2$ . The agreement between figure 7.4 and figure 7.5 is striking. Not only does the theory reproduce the qualitative features, also the size of the compensation field and the exact same slight gate voltage dependence are matched. Note that the calculations were done for a single lead Anderson model with the DOS shown in figure 4.8(a), but with  $\rho_\uparrow \neq \rho_\downarrow$ . The effective value assumed for the polarization was  $\mathcal{P} = 10\%$ . Also an asymmetry between source and drain coupling of 2 as estimated from the experimental data, cf. chapter 6 was assumed in the numerics. This then even reproduces the pattern of weak and strong single electron tunneling lines as observed in the experiment.

In figure 7.6 the experimental and theoretical results for the conductance and the spectral

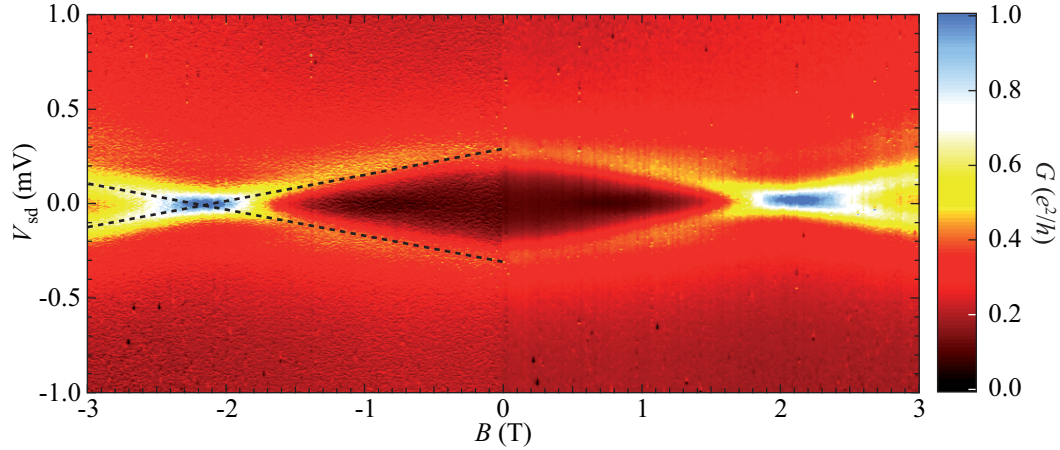


**Figure 7.7.:** Differential conductance versus magnetic field  $B$  and source drain voltage  $V_{sd}$  for a fixed gate voltage  $V_{gate} = 2.044$  V corresponding to the center of the charge state shown in figure 7.4 (a). The two parts of the image for positive and negative magnetic fields were stitched together and result from two separate measurements. The dashed lines indicate the expected slope for  $V_{sd} = (g\mu_B/e)B$  with  $g = 2$ .

function can be compared directly by means of line traces through the center of the corresponding plots in figures 7.4(a), (c), and (e) as well as figures 7.5(a), (c), and (e). The finite background conductance from which the Kondo peak emerges is caused by a superposition of the logarithmic decay of the Kondo effect from the dominant level and cotunneling contribution from other levels. The numerical data reproduces the general line shape of the measured peaks as well as the evolution of their splitting with good agreement.

In panel (c) of figure 7.6, an additional feature of the measurement is marked by the black arrows. At values close to the compensation field small side maxima or shoulders of the main peak appear. A possible explanation for these additional peaks is discussed in chapter 9.

As the final measurement in this chapter, figure 7.7 shows the full evolution of the splitting in the center of Coulomb diamond “1” for a magnetic field range of  $-3$  T to  $3$  T. Starting from zero field the splitting is first compensated in either direction until the compensation at a field  $B_{exch} \sim 2$  T is reached. At this point the two high conductance lines representing the split Kondo resonance merge. At even higher absolute field values the exchange field is overcompensated by the external field, leading again to a separation of the conductance peaks. The linear evolution of the peak splitting is indicated by the dashed white lines that display a slope of  $g\mu_B/e$  for  $g = 2$ , exactly what is expected from the Zeemann effect.

The fact that the conductance enhancement due to Kondo correlations is found again at zero bias voltage for finite fields, indicates that the tunneling induced level splitting is exactly compensated and coherent spin flip processes can again occur at zero extra energy.

This motivates the assumption that the tunneling induced exchange field is completely analogous to an external field, which is further confirmed by the considerations of the scaling properties in the following chapter.

## 8. Scaling properties

In this chapter a fundamental feature of Kondo physics is tested, namely *universal scaling*. In chapter 4 it was already briefly mentioned that the temperature dependence of the normalized Kondo conductance shows a universal behavior if the temperature is scaled by the Kondo temperature, i.e.  $G(T/T_K)/G(T=0)$  is universal for any Kondo quantum dot. The semi-empirical expression for the conductance was already given in equation 4.1.

Besides the temperature dependence, universal scaling is theoretically also expected for the magnetoconductance, i.e. the dependence of the conductance on the magnetic field. In this case the magnetic field needs to be scaled by, what we call, a Kondo field  $B_K$  summing up all relevant parameters in one quantity. Theoretically this scaling is expected [see figure 8.1] but we are only aware of a single experimental work that looked at the magnetic field scaling [105]. To our knowledge, so far no experimental investigation of these universal scaling properties in the presence of ferromagnetic leads was conducted.

### 8.1. Scaling as a function of temperature

The property of universal scaling of the temperature dependence is so generic that it has often been used in observations of potential Kondo correlations both in semiconductor as well as carbon nanotube based quantum dots to attribute the observed conductance enhancements to the Kondo effect via their temperature dependence [41, 43].

As expressed at the end of the previous chapter, the observation that the splitting of the Kondo conductance is compensated in a certain finite magnetic field can be seen as an equivalence of external field and exchange field. If the Kondo effect is fully restored at zero bias for finite fields, it should also be possible to observe the well known universal scaling of  $G(T)/G(T=0)$  at this field value. Figure 8.2 shows a charge state for which the temperature dependence was measured at a finite magnetic field of  $B = 1$  T. For a comparison, figure 8.2(a) shows the conductance map at base temperature and zero field. The plot is not centered around  $V_{sd} = 0$  but rather shows an asymmetric bias range, in order to include an additional conductance resonance appearing at higher voltages. This resonance is probably a result of higher order tunneling events, so-called inelastic cotunneling. The corresponding excited states are often orbital excitations. In this case the position of the peak at  $V_{sd} \approx 1.2$  mV and the subband mismatch, i.e. the distance to the next orbital state,  $\delta \approx 1$  meV as determined in chapter 6, fit reasonably well.

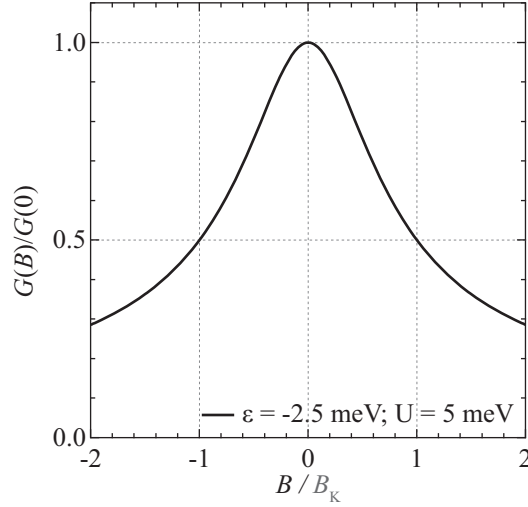


**Figure 8.1.:** Exemplary numerical renormalization group calculation for the magnetic field dependence of the Kondo conductance. In analogy to the temperature dependence, the scaling parameter  $B_K$  is defined such that  $G(B = B_K)/G(B = 0) = 1/2$ . Here the level position is  $\varepsilon = -2.5$  meV and the charging energy is  $U = 5$  meV (calculations done by I. Weymann).

In figure 8.2(b) the same charge state as in (a) is shown at a finite field of  $B = 1$  T. The splitting is compensated and only a sharp central resonance remains (cf. chapter 7). This central peak is labeled by “1” for later reference. The cotunneling resonance is also still present and it has not been influenced by the presence of magnetic field. This is logical since the magnetic field was applied perpendicular to the carbon nanotube and should not influence the orbital degrees of freedom. In figure 8.2(c) line cuts at constant gate voltage along the center of the Coulomb diamond in (b) are shown at different temperatures. The height of peak “1” decreases with increasing temperature while peak “2” remains unchanged, showing the fundamentally different nature of the effects leading to these conductance resonances. The detailed temperature dependence for peak “1” is shown in figure 8.3(a). A fit to these points with the semi-empirical formula 4.1 for the spin-1/2 Kondo conductance yields a very good result over the whole available temperature range.

In figure 8.3(b) the scaled data points are shown together with a fit curve that is the result of simply plotting the scaled conductance. Although from a single set of data no conclusion about universality can be drawn, figure 8.3(b) demonstrates how accurately the fit describes the data points as well as the expected scaled behavior. The plot levels off exactly at 1, so  $G(T = 0) = 0.43(e^2/h)$  as resulting from the fit describes the zero temperature value of the conductance very well. Furthermore the value of  $G(T = T_K)/G(T = 0)$  is almost exactly 0.5 as expected from equation 4.1 if plotting the scaled parameters [90]. As equation 4.1 has seen numerous experimental validations, an agreeing fit for the tem-

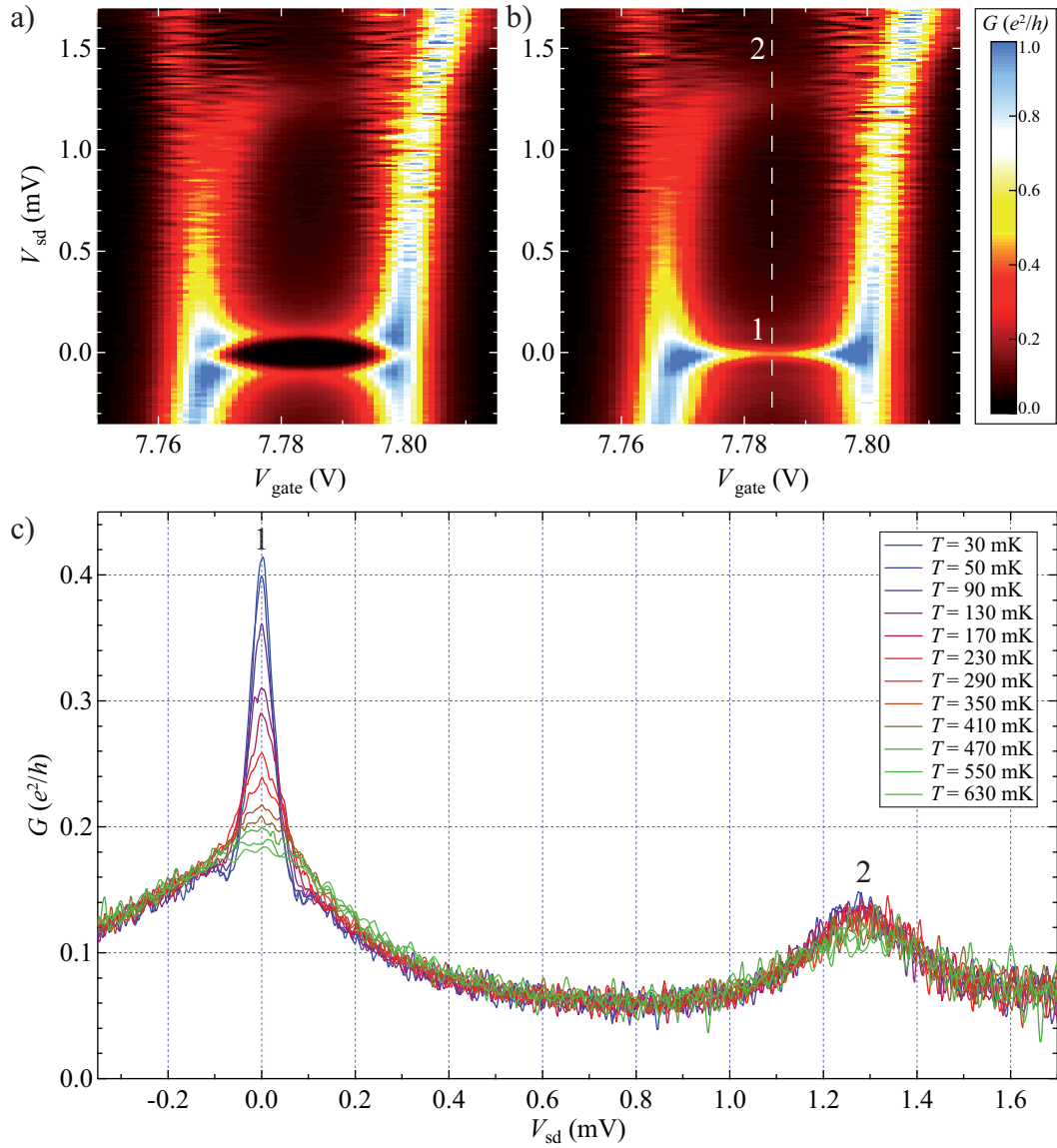


**Figure 8.2.:** (a) Color scale plot of the conductance as a function of  $V_{\text{gate}}$  and  $V_{\text{sd}}$  at  $T = T_{\text{base}}$  and  $B = 0$  T. Apart from the central split resonance another conductance resonance at higher positive bias can be seen. (b) Same measurement as shown in (a), now at  $B = 1$  T. The splitting of the Kondo resonance is completely compensated (peak 1). Note that neither the position nor the shape of peak 2 has changed. (c) Temperature dependence of the conductance along the dashed line in panel (b). The Kondo peak shows a strong temperature dependence while peak 2 is not changing significantly.

perature dependence of the conductance enhancement is seen as a strong indication that the underlying physics is dominated by Kondo correlations.

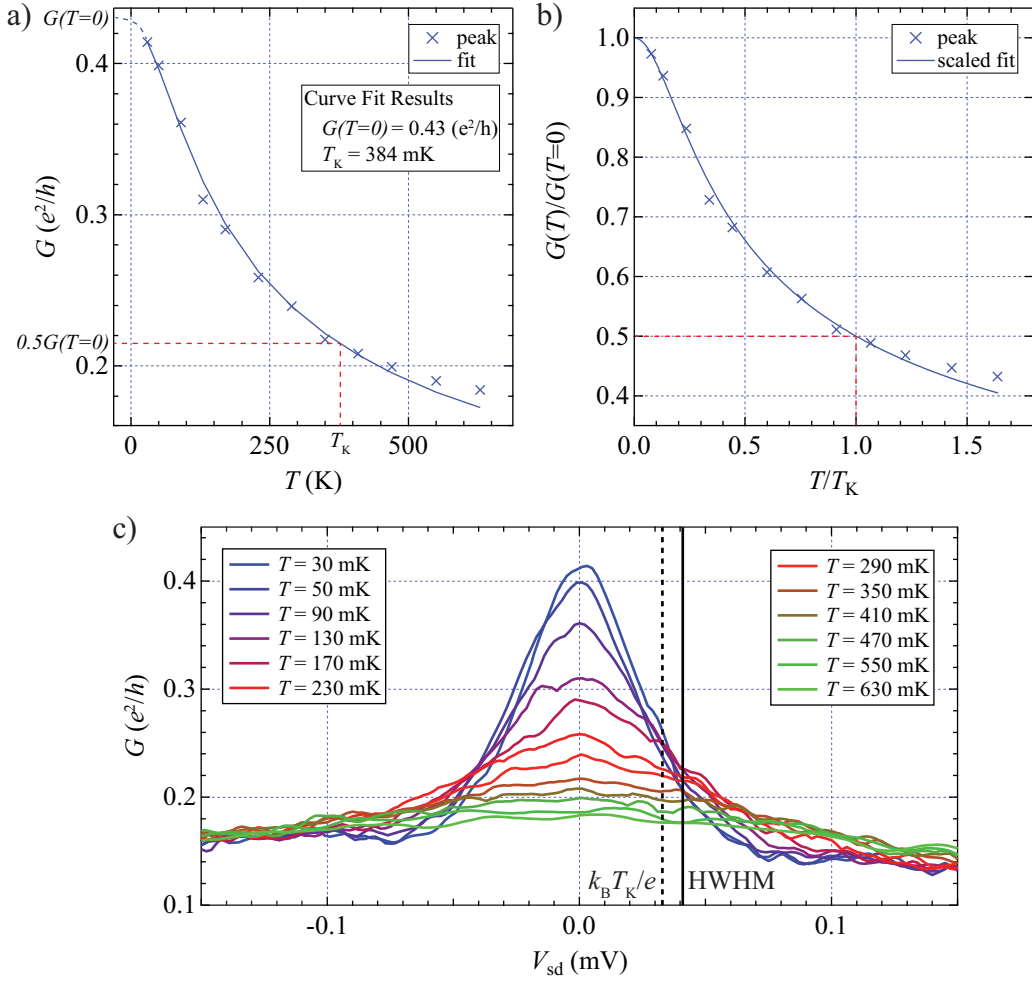


**Figure 8.3.:** (a) Maximum values of the conductance traces shown in figure 8.2(a) versus the temperature. Also shown is the result of a fit of the empirical temperature dependence [eq. 4.1] to the data points. The resulting fit parameters are  $T_K = 384 \text{ mK}$  and  $G(T = 0) = 0.43 e^2/h$ . (b) Same data as in (a) plotted on the scaled axes. In all cases, a linear scaling has been chosen for the temperature axis as fit for the range  $0 < T \lesssim 3T_K$ . (c) Temperature dependent line traces as shown in figure 8.2(c). The energy that corresponds to  $T_K$  is marked by the dashed vertical black line. Note that it is not equal to the half width at half maximum (HWHM) which is marked by the solid vertical black line.

In the following part of this section we give an account of the temperature dependence of two resonances at zero field. Although we do not expect universal behavior in this situation, the observations are still instructive. Figure 8.4(a) and 8.4(c) show two-dimensional color scale plots of the differential conductance  $G(V_{\text{gate}}, V_{\text{sd}})$ , both measured at zero external field and base temperature. In figs. 8.4(b) and 8.4(d) line traces of the differential conductance  $G(V_{\text{gate}}=\text{const.}, V_{\text{sd}})$  at the center of each CB region of (a) and (c) at different

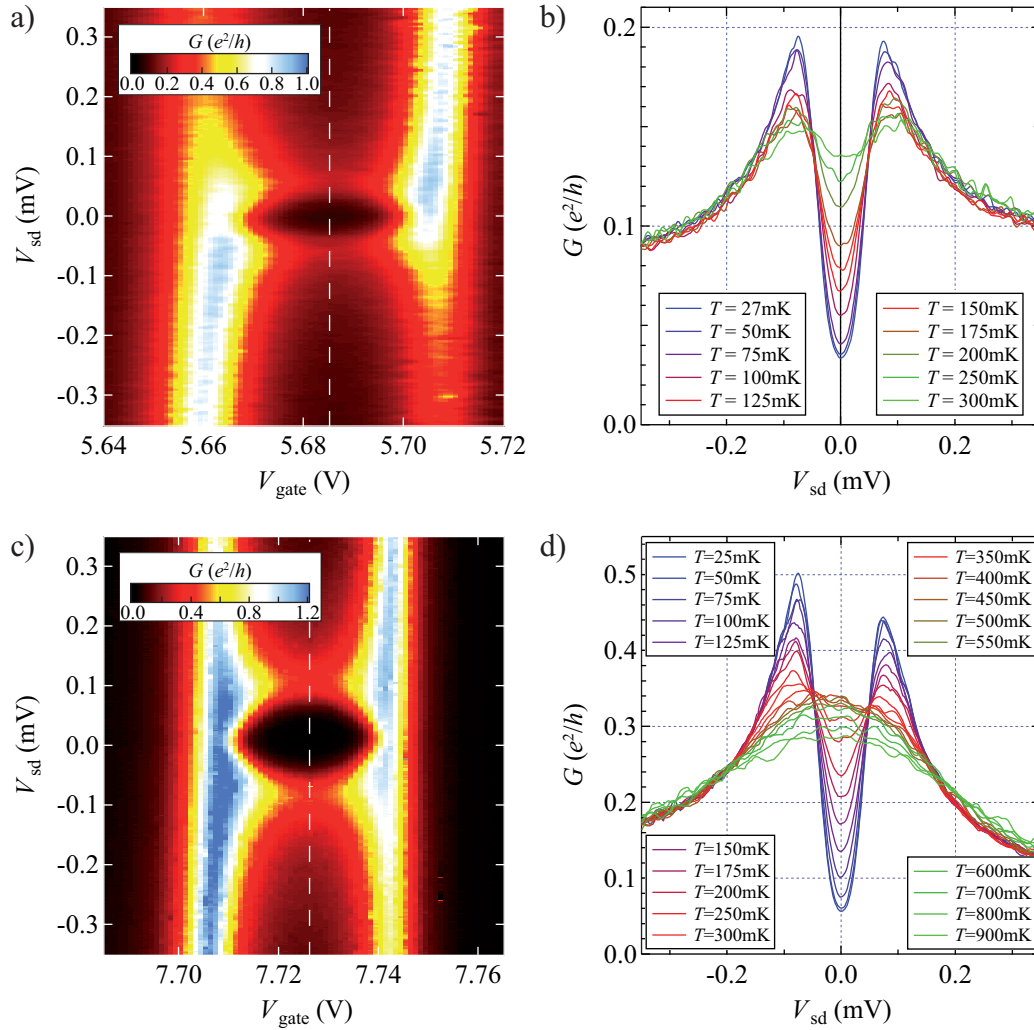


**Figure 8.4.:** (a) and (c) Color scale plot of the differential conductance as a function of  $V_{\text{gate}}$  and  $V_{\text{sd}}$  at  $T = 25$  mK and  $B = 0$  T for sample BA. The two panels display different charge states; for both additionally also the temperature dependence of the conductance along the dashed line was measured. (b) and (d) Temperature dependence of the conductance along the dashed lines in (a) and (c), measured at  $V_{\text{gate}} = 5.688$  V and  $V_{\text{gate}} = 7.755$  V respectively. The apparent difference of the gate voltages in (a) and (c) and the values where the line traces were measured result from a small drift in the effective gate potential typically occurring over the course of one or two days.

temperatures are displayed. The offset between the voltage values at which the line traces were recorded and the apparent center of the charge states is due to a slow drift of the gate potential. From these curves the peak height both for the left and right peak is extracted. The conductance values at the peaks are plotted versus the temperature in figures 8.5(a)



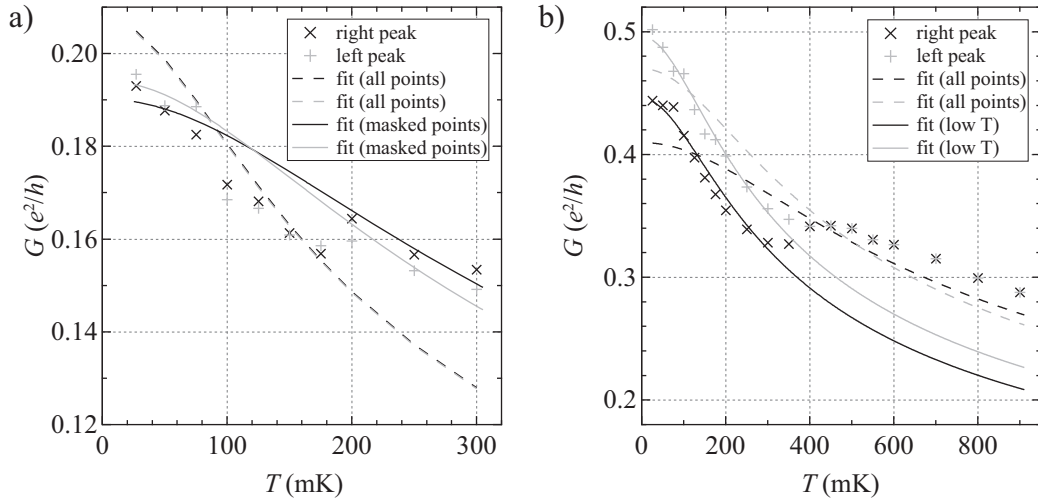


**Figure 8.5.:** (a) Peak values of the conductance from fig. 8.4(b) for  $V_{\text{gate}} = 5.688$  V, both for the left and right peak in the split case. The dashed and solid lines are fits to either right or left peak value taking into account all the data points or just a subset, respectively (see text). (b) Same evaluation as panel (a) for  $V_{\text{gate}} = 7.755$  V. At the higher temperatures  $T > 400$  mK only one peak remains. The temperature dependence changes considerably at this point.

and 8.5(b), together with resulting fits to different portions of the data. In one case all data points were taken into account for the fit. In a second try the fits were tweaked by not taking into account the points that deviated strongest. The results of the fitting procedures for all points as well as for a subset of data points are shown in table 8.1. The most obvious observation in figure 8.5 is that in both cases the conductance peaks do in fact vary strongly with temperature. In the first case, for  $V_{\text{gate}} = 5.688$  V, the temperature dependence shows an irregularity for  $T = 75, 100, 125$ , and  $150$  mK. The conductance for these values appears disproportionately lower than compared to both lower and higher temperature values. The exact reason for this effect is unclear but it makes fitting the data with a single temperature dependence very unreliable. These are consequently also the points that were masked for a potentially improved fitting result.

The situation appears even more intricate for the temperature dependence in the case of  $V_{\text{gate}} = 7.755$  V. From a temperature of about  $T = 350$  mK on upwards the peak height has decreased so much, and at the same time the width has increased, so that no peak separation but only one apparent peak remains. After the merging of the peaks obviously only the height of the central peak is read off for retrieving the data points in figure 8.5(b).

It is clearly visible in figure 8.5(b) that the behavior of the conductance changes drastically from the point on where only one apparent peak remains. To put the effect into perspective one can have a look at the value of the temperature at which this transition occurs - in figure 8.5(b) from 350 mK to 400 mK.

peak	parameter	all points	sel. points	$V_{\text{gate}}$
right	$T_K(\text{mK})$	985.88	1026	5.688 V
left		832.19	862.1	
right	$G_0(e^2/h)$	0.18589	0.19022	
left		0.18968	0.19419	
right	$T_K(\text{mK})$	1797.8	779.3	7.755 V
left		1174.6	735.81	
right	$G_0(e^2/h)$	0.40982	0.44556	
left		0.47002	0.49609	

**Table 8.1.:** Parameters resulting from a numerical fit of the universal Kondo conductance function,  $G(T) = G_0/[1 + (2^{1/s} - 1)(T/T_K)^2]^s$  with  $s = 0.22$ , to the experimental data of Fig. 8.5. Values are given for both peaks separately either taking into account all or just a selected subset of data points (see text for details).

The size of the splitting in zero field, as has already been argued in chapter 7, can be converted to a field value via the Zeeman effect. Here, the splitting in terms of energy is almost exactly  $\Delta V_{\text{sd}} = 150 \mu\text{eV}$  which corresponds to an effective field of  $B_{\text{eff}} = 0.65 \text{ T}$ . Translated into a temperature according to equation 4.5, it corresponds to roughly

$$\Delta\epsilon/k_B = 37 \mu\text{eV}/k_B \simeq 400 \text{ mK}. \quad (8.1)$$

This is in very good agreement with the temperature scale at which the above mentioned transition occurs. This essentially means that the Kondo correlations which are suppressed at zero energy since the spin-degeneracy of the quantum level is lifted by the tunneling induced effective field [cf. figure 4.3(d) and (e)] are re-established at zero energy because oscillations between the two spin directions become possible again due to the elevated temperature. From this background it is not surprising that these two distinct parameter regimes can not be fitted with a single temperature dependence. Indeed both traces, the left and the right peak points for  $V_{\text{gate}} = 7.755 \text{ V}$ , can be fitted quite well when the fit is restricted to the data points for the lowest few temperatures, see Fig. 8.5(b). This however is not possible when the full range is taken into account. It might seem like these arguments are a bit too artificially trying to contradict the potentially satisfying fit results of figure 8.5. However, seeing that several combinations of  $T_K$  and  $G_0$  result in more or less satisfying fitting results, there is a certain ambiguity in the choice of these parameters. Also, the considerations done in the context of figure 7.3, further support the low reliability of the fits in zero field. Would the Kondo temperature really reach values of  $\sim 750 \text{ mK}$  - according to the fit to selected points - or even  $\sim 1200 \text{ mK}$  to  $1800 \text{ mK}$  - according to the fit to all points -  $k_B T_K$  would be in fact larger than  $\Delta\epsilon$ . This means

in turn that the width of the Kondo resonance would be so large that only a singly peak would be observed. Since clearly two peaks are observed, the level splitting has to be at least of the same size as the Kondo temperature.

For the second example at  $V_{\text{gate}} = 5.688 \text{ V}$ , the splitting amounts to almost exactly  $\Delta V_{\text{sd}} = 150 \mu\text{eV}$  which corresponds to  $B_{\text{eff}} \sim 0.7 \text{ T}$ . The investigated temperature range for this specific charge state unfortunately ends at  $T = 300 \text{ mK}$ .

To conclude this discussion about the temperature dependence, it should be mentioned that a universal scaling is only expected for a situation where the sample is definitely in the Kondo regime. The general description of a single localized state connected to electron reservoirs by tunnel junctions is delivered by the Anderson model. This model has several regimes that are parametrized by  $\tilde{\epsilon} \equiv \epsilon/\Gamma$  [90]. Only for  $\tilde{\epsilon} \ll -0.5$  the system is said to be in the Kondo regime. For  $-0.5 \lesssim \tilde{\epsilon} \lesssim 0$  the system is said to be in the mixed-valence regime where a deviation from the universal scaling behavior is expected. However, taking typical experimentally determined parameters for the sample at hand, the charging energy amounts to roughly  $E_C \approx 5 \text{ meV}$ . Lets assume an occupation of the dot with  $4N + 1$  or  $4N + 3$  electrons as necessary for the spin-1/2 Kondo effect. The size of the Coulomb diamonds belonging to these charge states, in the easiest case, is  $U$ . Being at the center of the Coulomb diamond means that the level position is at half the addition energy,  $U$  in this case, so  $\epsilon \approx -2.5 \text{ meV}$ . The coupling strength is on the order of  $1 \text{ meV}$ . This means that a good estimate for  $\tilde{\epsilon}$  is  $\tilde{\epsilon}_0 \approx -2.5 \ll -0.5$  and so the sample should definitely be in the Kondo regime and universal scaling should be observed.

## 8.2. Scaling as a function of magnetic field

Up to this point it was shown that a proper fit to the empirical formula [eq. 4.1] can only be achieved when investigating the temperature dependence of a quantum dot with ferromagnetic leads at a finite external field of the appropriate size to compensate the tunneling induced exchange field. This is already a strong indication that universal scaling behavior is recovered when quantities are measured relative to zero effective field  $B_{\text{eff}} = B - B_{\text{exch}} = 0$ , where  $B_{\text{exch}}$  is the tunneling induced exchange field and  $B$  the externally applied field.

Several charge states have been investigated in terms of their magnetoconductance. An external magnetic field poses, just as a finite temperature does, an energy scale on which the conductance depends. For the Kondo effect in quantum dots with normal leads it is known that the magnetoconductance at zero temperature also shows a universal scaling behavior. In other words,  $G(B)/G(B=0)$  versus  $B/B_K$ , where  $\tilde{G}(B_K) = 1/2$ , is independent of the specific charging energy  $U$ , coupling strength  $\Gamma$ , or the actual level position  $\epsilon$  (i.e. the gate voltage). If the above considerations are correct, the same scaling behavior should also be seen in the presence of ferromagnetic contacts, with the reference point

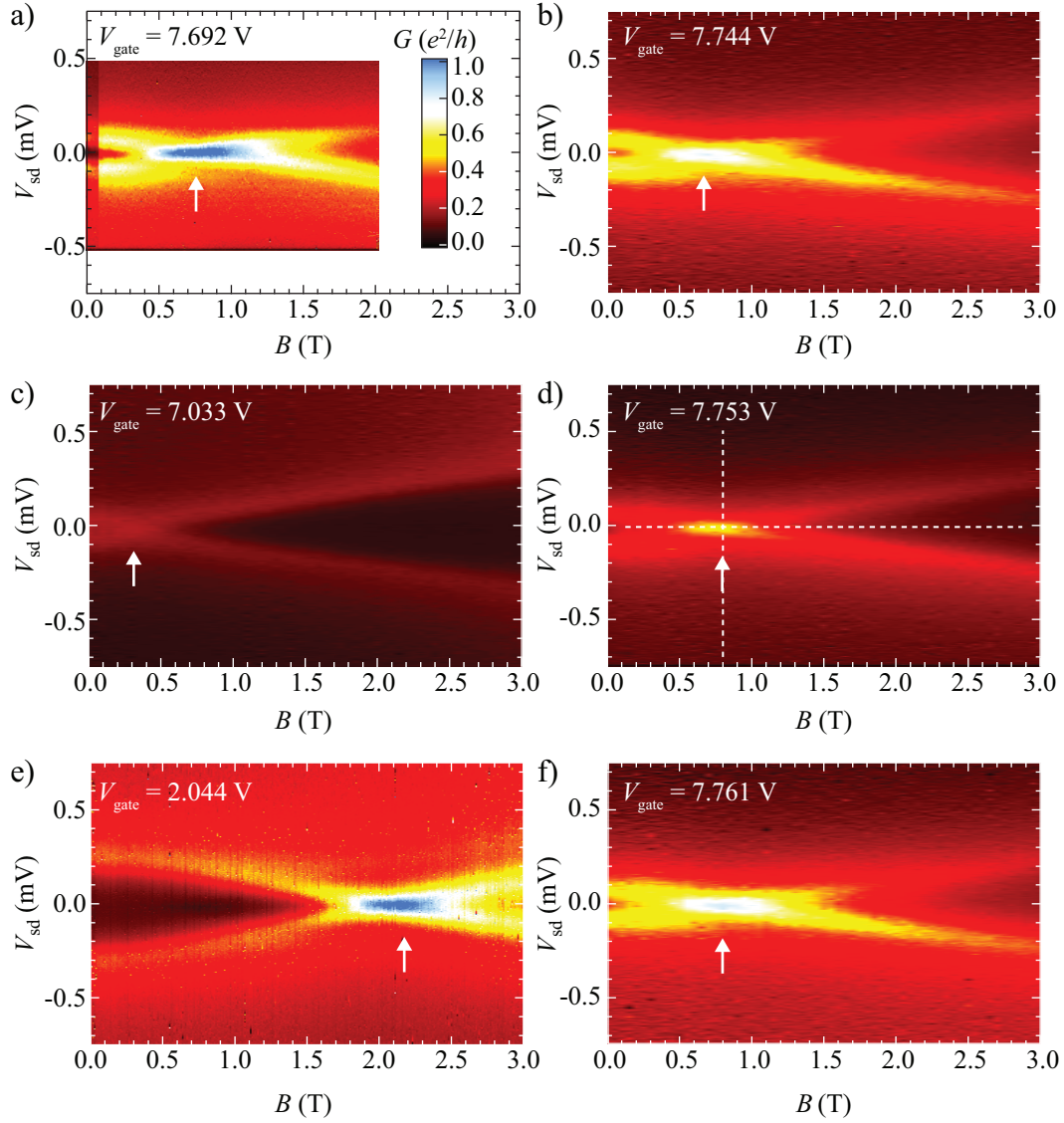


**Figure 8.6.:** Differential conductance as function of source drain voltage  $V_{sd}$  and magnetic field  $B$  for six different gate voltage values  $V_{gate} = 7.692$  V(a),  $7.744$  V(b),  $7.033$  V(c),  $7.753$  V(d),  $2.044$  V(e), and  $7.761$  V(f). Note that the color scale shown in (a) applies to all plots. The plots shown in (b), (d), and (f) are from the same Coulomb blockade region at positions  $\epsilon/U = -1/4$ ,  $-1/2$ , and  $-3/4$ . The white arrows indicate the value of the tunneling induced exchange field  $B_{exch}$ . In panel (d) the white dashed lines indicate the positions of the traces for fixed  $V_{sd}$  and fixed  $B$  that are referenced in the text.

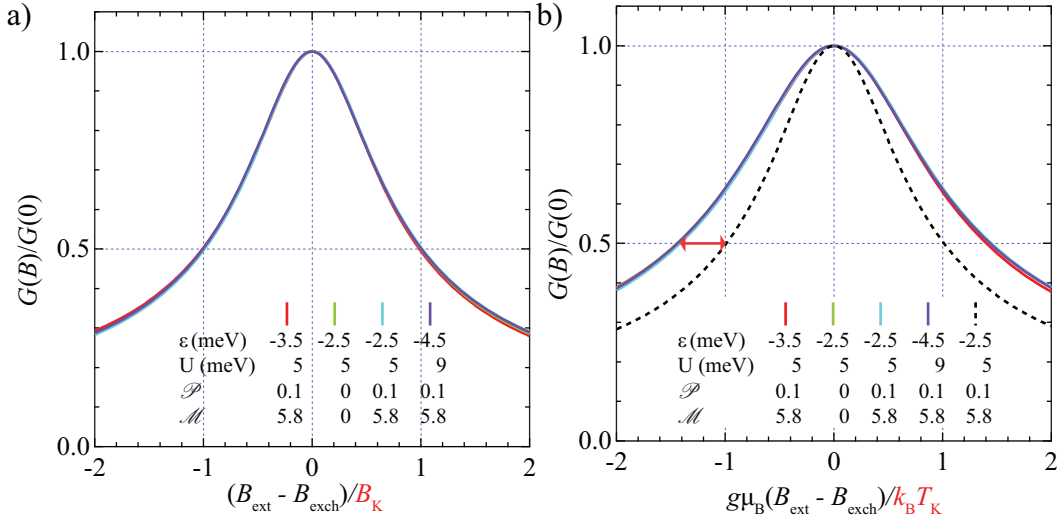


**Figure 8.7.:** (a) Numerical results for the scaling of the conductance versus the magnetic field, for different values of the characteristic parameters  $\epsilon$  (level position),  $U$  (charging energy),  $\mathcal{P}$  (polarization), and  $\mathcal{M}$  (magnetization). The scaling parameter in this case was the *Kondo field*  $B_K$  (see text). Note that the HWHM is then by definition 1. The non-magnetic case was included in the considerations and is plotted as the green curve. The scaling collapse is of such high quality that the curves are virtually indistinguishable. (b) Numerical scaling result if the scaling parameter is taken to be the *Kondo temperature*  $T_K$ . As elaborated in the text, the value of  $k_B T_K$  is a factor 1.4 smaller than  $g\mu_B B_K$ , seen in the fact the the HWHM is wider by precisely this value (see red double arrow). The dashed line corresponds to the cyan line from panel (a) and was added to illustrate the difference between  $B_K$  and  $T_K$ .

zero effective field:

$$G(B_{\text{eff}})/G(B_{\text{eff}} = 0) \quad \text{vs} \quad g\mu_B B_{\text{eff}}/k_B T_K. \quad (8.2)$$

In figure 8.6 the differential conductance is plotted versus the source drain voltage and the magnetic field,  $G(V_{\text{sd}}, B)$  for different charge states of different samples. The splitting at zero field is reduced when the field is increased until it is compensated at a field value characteristic for the particular charge state. The compensation field is marked by a white arrow in each panel of figure 8.6. From these plots the zero bias conductance is extracted as indicated by the dashed white line in figure 8.6 (d). This specific example is displayed in figure 8.8. Here both the compensation field  $B_{\text{exch}}$  and the conductance at the compensation field  $G(B_{\text{exch}})$  can be read off.

From the theoretical side, the question of interest is whether the scaling behavior for the magnetoconductance can be recovered in the presence of a tunneling induced exchange field. Before this question can be answered one has to consider that there are different

Fig. 8.6	$V_{\text{gate}}$ (V)	$B_{\text{exch}}$ (T)	$G(B_{\text{eff}} = 0)$ ( $e^2/h$ )	$B_K$ (T)
(a)	7.692	0.75	1.085	0.72
(b)	7.744	0.7	0.800	0.72
(d)	7.753	0.8	0.547	0.55
(f)	7.761	0.8	0.807	0.77
(e)	2.044	2.15	1.070	0.55
(c)	7.033	0.3	0.209	0.58

**Table 8.2.:** Summary of parameters extracted from line traces analogous to figure 8.8 from the color maps in figure 8.6.  $B_K$  denotes the Kondo field value that results from manually scaling the field axis to make the experimental data coincide with the NRG curve (see text for details).

ways of determining the Kondo temperature or rather the *Kondo energy scale*. So far only the temperature dependence of the conductance was investigated. In this case, for  $V_{\text{sd}} = 0$  and  $B = 0$ , the *Kondo temperature*  $T_K$  is defined as the temperature value where  $G(T = 0)/G(T = T_K) = 1/2$ . Similarly a Kondo energy scale can be defined by taking the value of source drain voltage  $V_K$  where  $G(V = 0)/G(V_K) = 1/2$  for  $T \simeq 0$  and  $B = 0$ . This was already indicated by the solid line in figure 8.3(c), while the dashed line in the figure corresponded to the value for  $T_K$ . Via NRG calculations the expected ratio between these two values is determined as  $eV_K/k_B T_K \sim 2$  [106]. In the experiment the values are  $k_B T_K = 33 \mu\text{eV}$  and  $eV_K \approx 41 \mu\text{eV}$ , giving only a ratio of 1.3. However, already the fact that  $eV_K$  is larger than  $k_B T_K$  should be seen as a positive indication. Due to the absence of further temperature measurements unfortunately no additional tests for this prognosis could be made.

There is yet another way to define a Kondo energy scale, which becomes available when investigating the dependence of the conductance on a magnetic field. In analogy to the previous two cases one can define a *Kondo field*  $B_K$  by the relation  $G(B_{\text{eff}} = 0)/G(B_{\text{eff}} = B_K) = 1/2$ . Note that the magnetoconductance trace here in the presence of ferromagnetic leads has to be shifted by the amount of the tunneling induced exchange field  $B_{\text{exch}}$  in order to refer to  $B_{\text{eff}} = 0$  rather than simply  $B = 0$ . The corresponding scaling collapse for this situation as expected from NRG calculations is shown in figure 8.7(a) for different sets of parameters  $\varepsilon$ ,  $U$ ,  $\mathcal{P}$ , and  $\mathcal{M}$ . The quasi perfect scaling collapse shows impressively that from the theoretical side unquestionably universal scaling, i.e. local spin symmetry, is recovered even in the presence of magnetization or spin polarization in the contacts when a finite external field is applied to compensate the tunneling induced exchange field.

NRG theory predicts a ratio of  $g\mu_B B_K/k_B T_K \sim 1.4$ . This ratio is indicated by a red double arrow in figure 8.7 (b) where the scaling result is shown when the effective magnetic field



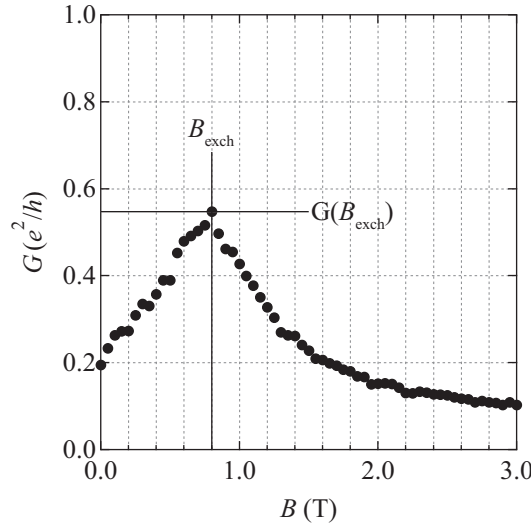


**Figure 8.8.:** Differential conductance versus magnetic field along the horizontal dashed line in figure 8.6 (d). Such a plot is generated for every gate voltage shown in 8.6 which allows to extract the tunneling induced exchange field, here  $B_{\text{exch}} \approx 0.8 \text{ T}$ , and the peak conductance, here  $G(B_{\text{exch}}) \approx 0.55 e^2/h$ .

is scaled by the *Kondo temperature*  $T_K$  rather than the *Kondo field*  $B_K$  as was done in 8.7 (a). Besides the scaling itself, this ratio is a second test that can be performed for the magnetoconductance due to the fact that several charge states were investigated.

Coming back to the experimental data, in figure 8.8 an exemplary zero bias magnetoconductance trace is shown for the gate voltage  $V_{\text{gate}} = 7.753 \text{ V}$ , which corresponds to the conductance along the white dashed line in figure 8.6 (d). The position of the conductance peak can be easily read off as  $B_{\text{exch}} \approx 0.8 \text{ T}$ . The same is true for the conductance value at the peak which is  $G(B_{\text{exch}}) \approx 0.55 e^2/h$ . These values were extracted for each of the magnetoconductance color maps displayed in figure 8.6 and are listed in table 8.2.

With the respective field value the conductance traces for each of the charge states can be shifted by the tunneling induced exchange field, resulting in an effective field axis. Figure 8.9(a) displays the raw data as extracted. The next step is to scale all the traces to the same height by dividing the data by the respective peak conductance value. The result of this operation is shown in figure 8.9(b) together with one of the coinciding NRG curves from figure 8.7(a). The deviation from the theory curve is still substantial. The corresponding *Kondo field*  $B_K$  is now determined by scaling the x-axis of each of the experimental traces separately such that the data points coincide optimally with the theoretical curve. This procedure of graphical fitting is equivalent to what is commonly done when fitting the temperature dependence to the semi empirical equation, with the only difference that there is no such equation for the case of the magnetic field dependence.

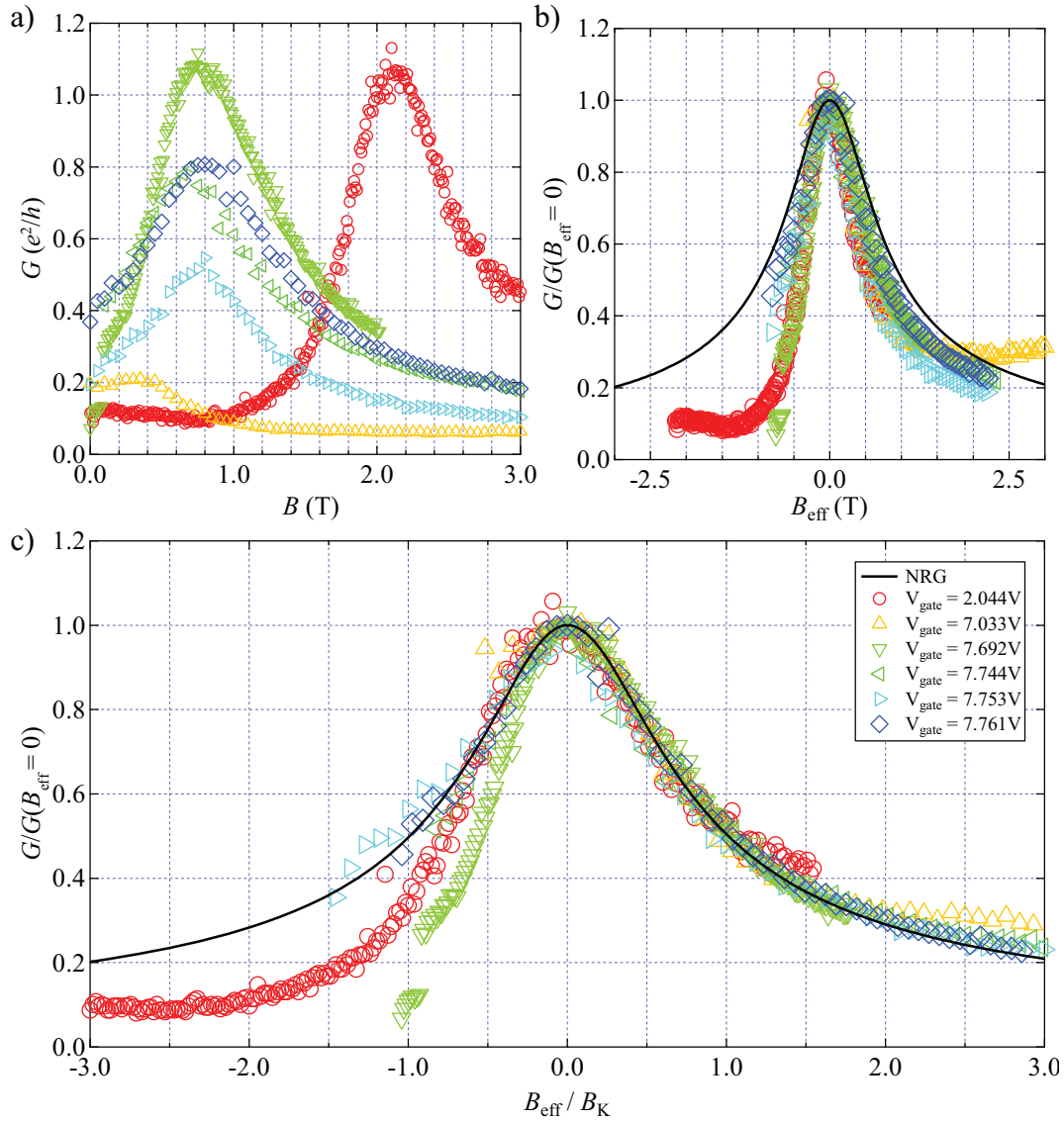


**Figure 8.9.:** Visualization of the single steps towards universal scaling of the experimental data. Note that the legend of panel (c) is the same for panels (a) and (b), with the only exception that the NRG data was omitted in the first panel. (a) Unscaled conductance versus external magnetic field  $B$ . (b) Scaled conductance versus effective magnetic field, together with a curve of the numerical data that was already displayed in figure 8.7(a). (c) Final scaling result. Each set of experimental data points was scaled by its appropriate *Kondo field*  $B_K$  (see text for details).

The resulting values for  $B_K$  were already given in table 8.2 and are repeated in table 8.3 together with the resulting energy values - if the magnetic field is translated into a Zeeman energy - and the corresponding temperature values.

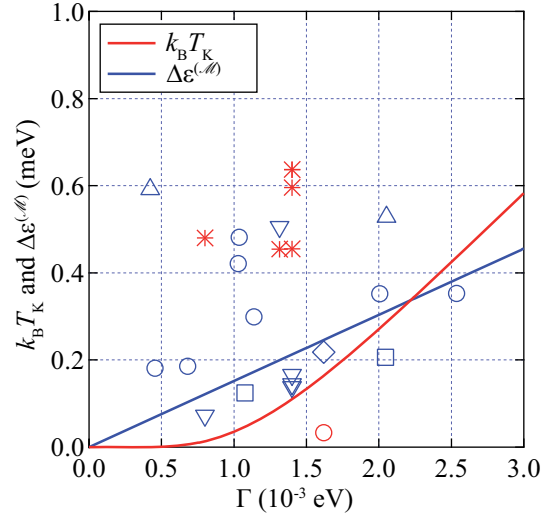


Figure 8.9(c) shows the main result of this whole chapter. The theoretically predicted scaling behavior of  $G(B_{\text{eff}}, V_{\text{sd}} = 0, T \simeq 0)$  is a central aspect of Kondo correlations which only appears in the case of local spin symmetry. Showing that the Kondo effect reappears at zero bias in finite field  $B_{\text{ext}} = B_{\text{exch}}$  and scales in the expected way, demonstrates or even proves that the tunneling induced exchange field can be considered physically equivalent to an externally applied field. This is not to be confused with a mere stray field effect generated by the presence of the magnetic contacts. Such a field would be on the order of  $\lesssim 100\text{mT}$ , while the observed field scale in the present case is on the order of 1 Tesla.

This being said, also the obvious shortcomings of the scaling collapse need to be addressed. The scaling does not work equally well for all investigated charge states. Note that  $B_K$  in all cases was chosen such that the data points at *positive* effective field values, i.e. right of the compensation point, agree best with the numerical curve. This is justified by the fact that it should be done consistently for all examples and in most cases the amount of available data above the compensation field exceeds that below.

One exception from having more data points below than above  $B_{\text{eff}} = 0$  is the case of  $V_{\text{gate}} = 2.044\text{V}$  which indeed shows a strong asymmetry of the scaling collapse. This apparent asymmetry would decrease if the fitting was done so that the full field range is optimally fit. The case of  $V_{\text{gate}} = 7.692\text{V}$  behaves similarly. There, more data points are available for positive effective field values (to which it is fit), but still an even stronger asymmetry appears is seen in the deviation from the NRG curve at negative effective fields. The key to this asymmetry may therefore lie in similarities of these two cases. Looking at figure 8.6 one realizes that these two charge states by far display the highest overall conductance. This could indicate the presence of elastic cotunneling events that can in principle already set in in the linear regime. A contribution from such tunneling events is not included in the present model and may be able to explain the deviations as they are mainly observed for the case of high conductance. The observation that the conductance for negative effective fields is lower than predicted by the NRG calculations seems to contradict this speculation. However, would the scaling be done such that the data points at negative fields coincided with the universal curve, the points positive effective fields would lie above the NRG data.

At this stage, with access to several Kondo energy scales, i.e.  $k_B T_K$  or  $g\mu_B B_K$ , as well as data for the level splitting induced by charge fluctuations for a number of different charge states, the analytical expressions, equation 4.1 and equation 4.27, that were already plotted in figure 7.3 can be compared to experimental data. Such a comparison is shown in figure 8.10. The solid lines are plots of the just mentioned equations analogous to figure 7.3. Note that certain assumptions were made to produce these plots. For the Kondo temperature equation 4.1 was evaluated at the center of the charge state, i.e. at  $\varepsilon = -U/2$ , for a charging energy of  $U = 4.3\text{meV}$ . Assuming equal charging energies for different samples and gate voltage areas is certainly not justified, but the following discussion is rather meant to be a qualitative one rather than a quantitative one. The plot



**Figure 8.10.:** Comparison between the theoretical expressions for the Kondo temperature  $k_B T_K$  (cf. equation 4.1) and the level splitting  $\Delta\epsilon^{(\mathcal{M})}$  and the corresponding experimentally observed values and their dependence on the coupling strength  $\Gamma$ . The theoretical curves (solid lines) were already shown in figure 7.3. The experimental data points for  $\Delta\epsilon^{(\mathcal{M})}$  (open blue symbols, different symbols correspond to different samples) are taken from a variety of samples and charge states at the center of the corresponding Coulomb diamond. The coupling strength was determined as described in chapter 6. Note that the star symbols for the Kondo temperature are results of dividing  $g\mu_B B_K$  by 1.4. The open red circle is the Kondo temperature as determined in figure 8.3 (see text for details).

for the level splitting  $\Delta\epsilon^{(\mathcal{M})}$  was done using the values for  $\mathcal{M}$  and  $\mathcal{F}$  as given in chapter 5. For different samples also these values might fluctuate due to small changes in the actual composition of the alloy.

The symbols in figure 8.10 are showing the experimentally determined parameters. They can be attributed to the theoretical curves by their color. The different shapes of the open blue symbols indicate different samples or charge states from which these values were derived. The two different shapes of the red symbols discriminate the way in which the Kondo temperature was determined. The open red circle is the value as determined by the temperature dependence of the conductance at finite field as described in the first section of the present chapter, cf. figure 8.3. The values shown as red asterisks were determined by dividing the Kondo energy  $g\mu_B B_K$  as given in table 8.3 by 1.4 [106].

The first thing to be recognized in figure 8.10 is that the experimental data points are in the right order of magnitude compared to the analytical expressions. The rather strong scatter should not distract from this fact. This is again a very good result of the rather simplified assumptions of a flat band structure and a single Anderson impurity model as was already stressed in the context of figure 7.2. Another agreement with the general understanding

$V_{\text{gate}}$ (V)	$B_K$ (T)	$g\mu_B B_K/k_B$ (K)	$g\mu_B B_K$ ( $\mu\text{eV}$ )	$V_K$ ( $\mu\text{eV}$ )	$V_K/B_K$
7.692	0.72	0.967	83.38	52	0.623
7.744	0.72	0.967	83.38	78	0.936
7.753	0.55	0.739	63.69	74	1.162
7.761	0.77	1.034	89.17	97	1.088
2.044	0.55	0.739	63.69	76	1.193
7.033	0.58	0.779	67.16	202	3.008

**Table 8.3.:** Summary of scaling results. The value of  $B_K$  is extracted by scaling the effective field axis. The third and fourth column contain this value expressed as a temperature and an energy, assuming  $g = 2$ . The fifth column shows the HWHM of the  $G(V_{\text{sd}}, B_{\text{eff}} = 0, T \approx 0)$  traces shown in figure 8.11. In the last column the ratio  $V_K/B_K$  is given, for which theoretically expected values range from 1.4 to 1.8. The agreement is not perfect but well in the right order of magnitude for most cases (see text for details).

can be seen in the fact that basically all experimental data points lie left of the crossing point of the theoretical curves. This means, in a range of coupling strengths where the splitting is expected to be larger than the Kondo temperature, i.e. observable in transport experiments, as is the case. Note that the values indicated by the asterisks are indirect results for the Kondo temperature, i.e. they were derived from the magnetoconductance data as described above. An apparently far more trustworthy value of the Kondo temperature indicated by the red circle in figure 8.10 is achieved by the direct fit of the temperature dependence. The counterpart to this Kondo temperature is the level splitting indicated by the open blue diamond. For this pair of values, determined for the same charge state, it is indeed the case that the level splitting is found to be larger than the Kondo temperature.

As a final consistency check for the applied theory, the predicted ratio between  $B_K$  and  $V_K$  is tested. From detailed analysis of the Anderson model by means of numerical renormalization group techniques, the ratio between the *Kondo field* and the *Kondo voltage* can be determined to be between 1.37 and 1.79 [106]. For this test, the HWHM of the conductance versus bias voltage at zero effective field,  $G(V_{\text{sd}}, B_{\text{eff}} = 0)$ , is determined. The plots in figure 8.11 show these traces for the same gate voltages that were already displayed in figure 8.6 as indicated by the dashed white line in panel (d) figure 8.6. The figure already displays the most obvious weaknesses of this evaluation. Some peaks are considerably asymmetric and especially the example shown in 8.11 (b) is so shallow that the HWHM value is hard to extract. Nevertheless, for a qualitative test, the resulting values of this investigation are still listed in the second to last column of table 8.3 together with the *Kondo field*  $B_K$  in different units. Additionally in the last column of table 8.3 the resulting ratios  $V_K/B_K$  are given. Generally it can be stated that the overall agreement is satisfactory. The deviation is in no case larger than an order of magnitude. The strongest deviations are

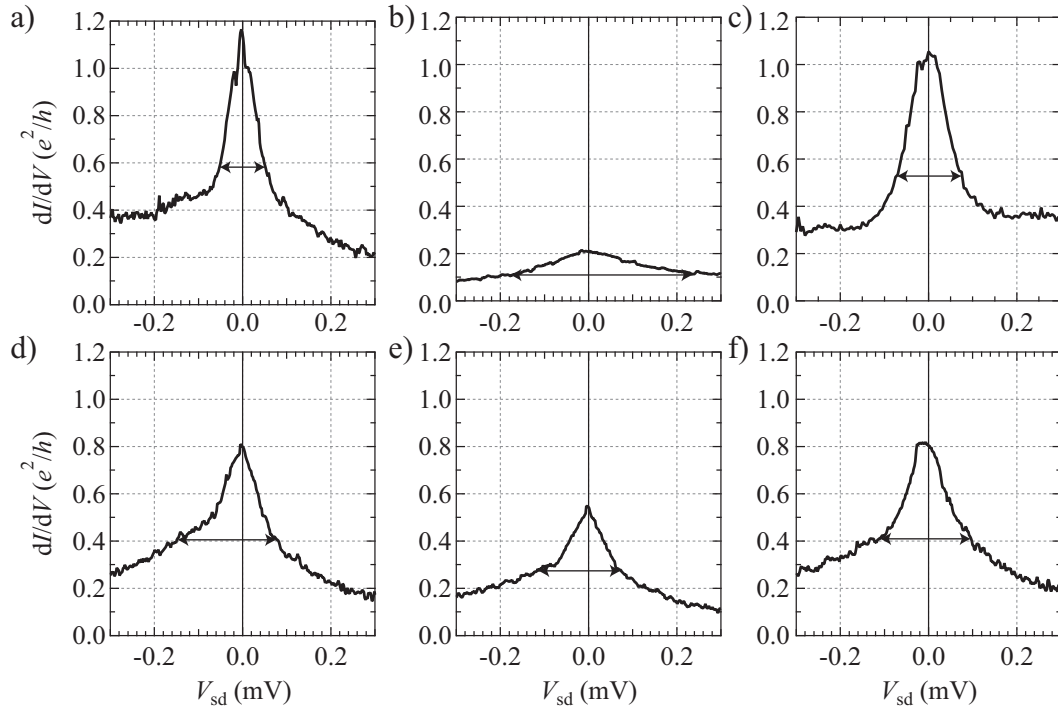


**Figure 8.11.:** Conductance line traces for constant magnetic field values as indicated by the vertical dashed white line in figure 8.6 (d). The magnetic field values for each of the panels corresponds to the size of the tunneling induced exchange field  $B_{\text{exch}}$  for the respective charge state. The separate panels correspond to (a)  $V_{\text{gate}} = 7.692 \text{ V}$ ,  $B = 0.75 \text{ T}$ ; (b)  $V_{\text{gate}} = 7.033 \text{ V}$ ,  $B = 0.3 \text{ T}$ ; (c)  $V_{\text{gate}} = 2.044 \text{ V}$ ,  $B = 2.15 \text{ T}$ ; (d)  $V_{\text{gate}} = 7.744 \text{ V}$ ,  $B = 0.7 \text{ T}$ ; (e)  $V_{\text{gate}} = 7.753 \text{ V}$ ,  $B = 0.8 \text{ T}$ ; and (f)  $V_{\text{gate}} = 7.761 \text{ V}$ ,  $B = 0.8 \text{ T}$ . The arrow in each panel marks the FWHM.

seen for the cases  $V_{\text{gate}} = 7.692 \text{ V}$  and  $V_{\text{gate}} = 7.033 \text{ V}$ , one being smaller by about a factor of two, the other one larger by a factor of two. These two states also show the largest and smallest overall conductance of the investigated cases. For  $V_{\text{gate}} = 7.033 \text{ V}$  with the smallest observed conductance the deviation is definitely partly due to systematic errors when reading off  $B_{\text{exch}}$ ,  $G(B_{\text{eff}} = 0)$ , and  $V_K$ . The strong deviation for  $V_{\text{gate}} = 7.692 \text{ V}$  comes a bit as a surprise, seeing that the ratio  $V_K/B_K$  is in principle closest to the expected value of that ratio for  $V_{\text{gate}} = 2.044 \text{ V}$ . These two charge states showed similarities when discussing the asymmetry of the scaling collapse which was attributed to the large overall conductance observed for both these values. The fact that the situation appears opposite in this case is not understood. This being said, as already stated, the small amount of available experimental data is not really suited for a systematic, maybe even statistical analysis, and the agreement in the order of magnitude can already be seen as a success of the measurement.

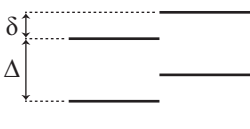
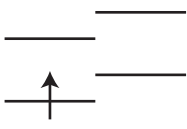
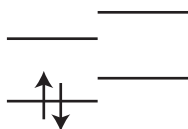
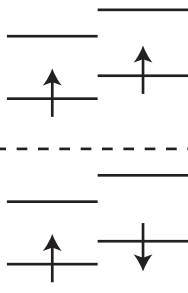


## 9. Summary and discussion

In this thesis, a thorough introduction on the structural and electronic properties of carbon nanotubes is presented. Starting from the band structure of a flat sheet of atomically thin carbon (graphene), the band structure of a carbon nanotube is deduced by imposing periodic boundary conditions to the wave function in the direction of the circumference of the tube. If the nanotube is also constricted longitudinally, a further quantization condition arises which leads to discrete states. The nanotube then becomes essentially a zero dimensional object, a quantum dot. The main properties of such a quantum dot are summarized in another chapter.

The second part of the introduction lays out the fundamentals of the Kondo effect. First this many body effect is described for a general situation of normal metallic contacts. It is also pointed out that peculiarly the Kondo correlations in a quantum dot give rise to an increased conductance while in a bulk system they increase the resistance. The major part of the corresponding chapter however is dedicated to the influence of magnetic contacts on the Kondo effect in a quantum dot. It is emphasized that the influence on the Kondo effect comes through the influence of the ferromagnetic contacts on the level structure. The states on the quantum dot are renormalized by charge fluctuations between the dot and the leads, i.e., the energy and the width of a certain level changes, according to the amount of charge fluctuations it is subject to. For spin imbalanced leads these charge fluctuations are spin dependent. An intuitive equation predicting the energy shift or rather the level splitting for different spin directions is given in terms of experimentally accessible parameters.

The experimental part finally can again be divided in two sections. The first part presents the observations of split Kondo resonances in carbon nanotube quantum dots with ferromagnetic leads, a main result of this thesis. First the qualitative features of the conductance resonance in terms of bias voltage and gate voltage are compared to theoretical considerations from chapter 4 and Ref. [53]. Then the results are also compared quantitatively. Having determined the coupling strength  $\Gamma$ , the magnetization  $\mathcal{M}$ , and the filling fraction  $\mathcal{F}$  of the present sample, equation 4.27 allows to theoretically predict a value for the tunneling induced spin splitting of the dot levels. This prediction compares very well to the experimentally determined value. The high level of understanding is further demonstrated by providing numerical renormalization group results, coming from calculations done by I. Weymann in the group of J. v. Delft in Munich, for the conductance of a Kondo quantum dot with ferromagnetic leads. For these calculations the experimentally

4N	4N + 1	4N + 2
 GS	 GS	 GS
		 1ES

**Figure 9.1.:** States participating in the charge fluctuations for an initial state  $|1, \uparrow\rangle$  (central column). We assume that also fluctuations into the energetically close excited states are possible. The characteristic energies of the spectrum are the level spacing  $\Delta\epsilon$  and the sub-band spacing  $\delta$ . The ground states are denoted as *GS* while the excited states are marked by *ES*.

determined parameters are used. The agreement between the experimental and numerical conductance data is very good.

The second part of the experimental discussion is dedicated to a more subtle property of Kondo physics. For normal contacts it is known that the conductance depends universally on the temperature in zero field or universally on an external field at zero temperature. Universal dependence in this context means that differences in the sample parameters as e.g. coupling strength between leads and nanotube or the actual position of the quantum dot level with respect to the Fermi energy all are lost when scaling the temperature or the field by a single parameter. Thus, universality means that all parameters determining the conductance in the Kondo regime can be summed up in a single parameter. The same behavior is found for the present case of ferromagnetic contacts if the field  $B$  is replaced by the effective field  $B_{\text{eff}} = B - B_{\text{exch}}$ , meaning that the universality in the temperature dependence is observed not at zero field but at zero effective field. Zero effective field in this context means that the tunneling induced exchange field is compensated by an external field. Just as well, the universality in the field dependence is recovered when shifting the magnetoconductance data by the value of the exchange field. This recovery of the universality feature in a finite external field is a very strong indication that the tunneling induced exchange field behaves completely analogous to an external field.

In the main part of the presented work the evaluation was mostly restricted to those mea-

surement features that clearly relate to the underlying physical effects discussed in the course of this work. The theoretical prediction for the tunneling induced exchange splitting, equation 4.1, and the experimentally observed value for the splitting differ by about a factor of 1.3 for the one case that was evaluated in detail in the main part. At the end of chapter 8 figure 8.10 showed the comparison between several experimental values and the theoretical prediction. For some values we see a considerable deviation from the predictions. One possible reason for this disagreement could be limitations of the single impurity model arising from the fact that a carbon nanotube provides more than just a single level as was shown in chapter 2. These additional levels could very well play an important role for the tunneling amplitudes and change the size of the energy correction.

Let us assume that a quantum dot contains one extra charge as depicted in the central panel of figure 9.1. The charge fluctuations that renormalize the energy of the state then again can be abbreviated by  $|1, \sigma\rangle \leftrightarrow |0\rangle$  and  $|1, \sigma\rangle \leftrightarrow |2\rangle$ . While there is only one way to carry out either of these processes for the single impurity model, the additional available states of a carbon nanotube might add to the tunneling amplitude. The ground state to ground state transitions must be extended by transitions involving excited states. The different possibilities for excited final states are visualized in figure 9.1. In order to simplify the discussion a bit, tunneling that involves states from a completely different orbital level are omitted. Also we assume the initial state always to be the ground state. The spin direction of the tunneling particle will be denoted by an arrow in the index, the orbital state as subscripts  $L$  or  $R$ .

The energy correction for the situation displayed in figure 9.1 has a completely analogous form to the correction for the single impurity Anderson model, cf. equation 4.6. This means that an integration of all available states in the leads is carried out over a sum of terms. Each of these terms corresponds to a certain charge fluctuation. The single terms are fractions where the numerator is the product of the tunnel coupling, for the spin direction tunneling, times the density of states from which or into which the charge tunnels. The denominator is the difference between the energy of the initial state and the final state. This way the tunneling process becomes less and less likely for higher energy difference between initial and final states. This results in the following expression:

$$\delta\epsilon_{\uparrow} = -\frac{1}{\pi} \int d\omega \left\{ \frac{\Gamma_{\uparrow}[1-f(\omega)]}{\omega - \epsilon_{L,\uparrow}} + \frac{\Gamma_{\downarrow}f(\omega)}{\epsilon_{L,\downarrow} + U - \omega} + \frac{\Gamma_{\uparrow}f(\omega)}{\epsilon_{R,\uparrow} + U - \omega} + \frac{\Gamma_{\downarrow}f(\omega)}{\epsilon_{R,\downarrow} + U - \omega} \right\} \quad (9.1)$$

Note that the subband spacing  $\delta$  does not appear explicitly in this notation since the difference in the orbital states was captured in the subscripts  $L$  and  $R$ . The first two terms then are the ones that already appeared in equation 4.6, while the last two terms correspond to the tunneling events involving excited states.



The same expression can be written down for the initial state with one spin on the dot but opposite spin direction  $|1, \downarrow\rangle$ . It reads

$$\delta\epsilon_{\downarrow} = -\frac{1}{\pi} \int d\omega \left\{ \frac{\Gamma_{\downarrow}[1-f(\omega)]}{\omega - \epsilon_{L,\downarrow}} + \frac{\Gamma_{\uparrow}f(\omega)}{\epsilon_{L,\uparrow} + U - \omega} + \frac{\Gamma_{\downarrow}f(\omega)}{\epsilon_{R,\downarrow} + U - \omega} + \frac{\Gamma_{\uparrow}f(\omega)}{\epsilon_{R,\uparrow} + U - \omega} \right\}. \quad (9.2)$$

With this the energy difference, i.e. the splitting, simply results in

$$\delta\epsilon_{\uparrow} - \delta\epsilon_{\downarrow} = -\frac{1}{\pi} \int d\omega \left\{ \frac{\Gamma_{\uparrow}[1-f(\omega)]}{\omega - \epsilon_{L,\uparrow}} - \frac{\Gamma_{\downarrow}[1-f(\omega)]}{\omega - \epsilon_{L,\downarrow}} + \frac{\Gamma_{\downarrow}f(\omega)}{\epsilon_{L,\downarrow} + U - \omega} - \frac{\Gamma_{\uparrow}f(\omega)}{\epsilon_{L,\uparrow} + U - \omega} \right\} \quad (9.3)$$

which is the same expression as the already known result from the single impurity Anderson model. This is actually quite intuitive as the excited states can be occupied by either spin direction and thus contribute equally to the corrections. Thus, when taking the difference these terms simply disappear. This remains correct also for the case of a dot occupation  $N + 3$  and also for higher excited states and shows that these additional levels do not contribute further to energy renormalization. This means that *fermionic* excitations alone do not lead to further contributions to the level splitting.

This changes however, when also bosonic excitations are taken into account. These are basically collective charge waves that can be excited at energies relevant in carbon nanotubes and provide further transport channels. These collective charge waves can be pictured as synchronized oscillation of the charge carriers in the nanotube due to Coulomb repulsion. It was shown recently by Koller et al. [107] that these bosonic excitation indeed need to be considered.

Another aspect that was neglected in the evaluation so far is spin orbit interaction. In the introduction it was already briefly addressed that spin orbit interaction was long thought to be absent in carbon nanotubes just like interaction between the electron spin and nuclear moments. However, the curvature of the nanotubes was in recent years more and more recognized as a source of spin orbit interaction. It turned out that indeed a finite spin orbit parameter could be determined and should be present in practically any situation [8, 9]. After these experimental evidences of spin orbit interaction in carbon nanotubes also first theoretical works started to investigate the influence of spin orbit coupling on the Kondo effect [108, 109]. Part of the predictions from these works is a rich substructure of satellite peaks in the conductance, see figure 9.2 from Ref [108]. Note that no ferromagnetic contacts were assumed in this case.

The discussion here should by no means be considered as conclusive but rather as an outlook onto what future experiments could aim at. A similar substructure was also observed in some of the measurements not presented in the main part. Most of the observations

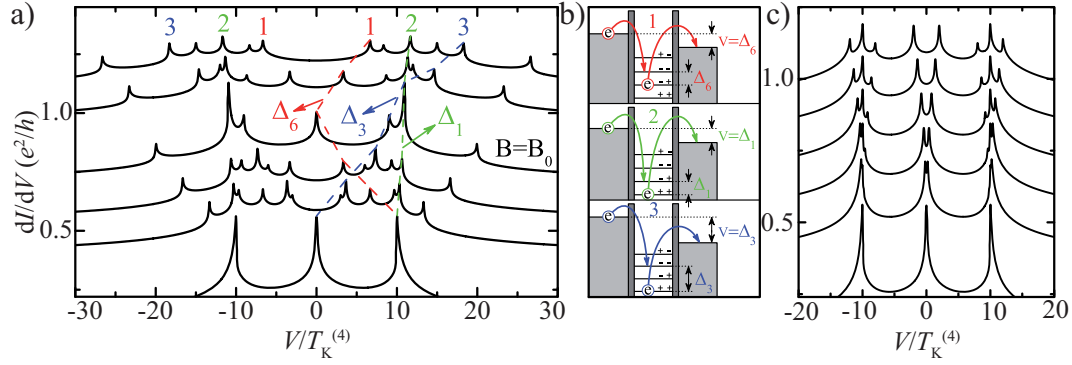


**Figure 9.2.:** Implications of the spin orbit coupling on the Kondo effect. (a) External magnetic field applied parallel to the tube axis. Due the SOI the Kondo peaks in the differential conductance split already at zero field. At higher fields a variety of peaks is predicted each of which can attributed to single electron cotunneling events shown in (b). (c) Differential conductance for the external field perpendicular to the axis. Taken from Ref. [108].

stem from an early measurement that best can be considered as preparatory. Such an example is presented in figure 9.3. Unfortunately there are no measurements for  $B = 0\text{ T}$  in the same gate voltage region, and the zero field splitting could not be determined. However, the splitting at  $B = -0.5\text{ T}$ ,  $\Delta\varepsilon = 412\mu\text{eV}$ , can be taken as an indication for the zero field splitting. Translating this value again into the tunneling induced exchange field this results in

$$B = \frac{412\mu\text{eV}}{2 \times 2 \times 5.788 \times 10^{-5} \text{ eV T}^{-1}} \sim 1.78\text{ T}.$$

Taking into account that the splitting at zero field probably was a little larger a good estimation for the tunneling induced exchange field would be  $2\text{ T}$ . In the context of what has been established in this work the expectation then would be to see the splitting being more and more compensated as an external field value of, e.g.,  $-2\text{ T}$  is approached. The result however looks completely different as figure 9.3(b) and (c) show. Instead of a smaller and smaller splitting additional peaks appear that are already visible in the color maps but even better in the corresponding line traces below the two dimensional plots. The energies at which the peaks are observed are typically of the order  $0.1\text{ mV}$ . Note that at least one experimental investigation [8] states a value of  $0.15\text{ meV}$  for the spin-orbit interaction strength. Also note that exactly at zero bias the conductance changes from a minimum at  $B = -0.5\text{ T}$  to a local maximum at  $B = -1\text{ T}$  and back to a minimum at  $B = -1.5\text{ T}$ , similar to what is observed in figure 9.2(a). Seeing that the contacts in the experimental case were ferromagnetic while the theoretical considerations were done for normal contacts, the albeit limited correspondence between figure 9.3 and figure 9.2 is certainly still intriguing at least. With the understanding of the tunneling induced exchange field to which the present work contributes and the knowledge of a sizeable spin orbit interaction especially in nanotubes with small diameters, future experiments should be able to target the appropriate parameter regime for observing the interplay between the two effects.

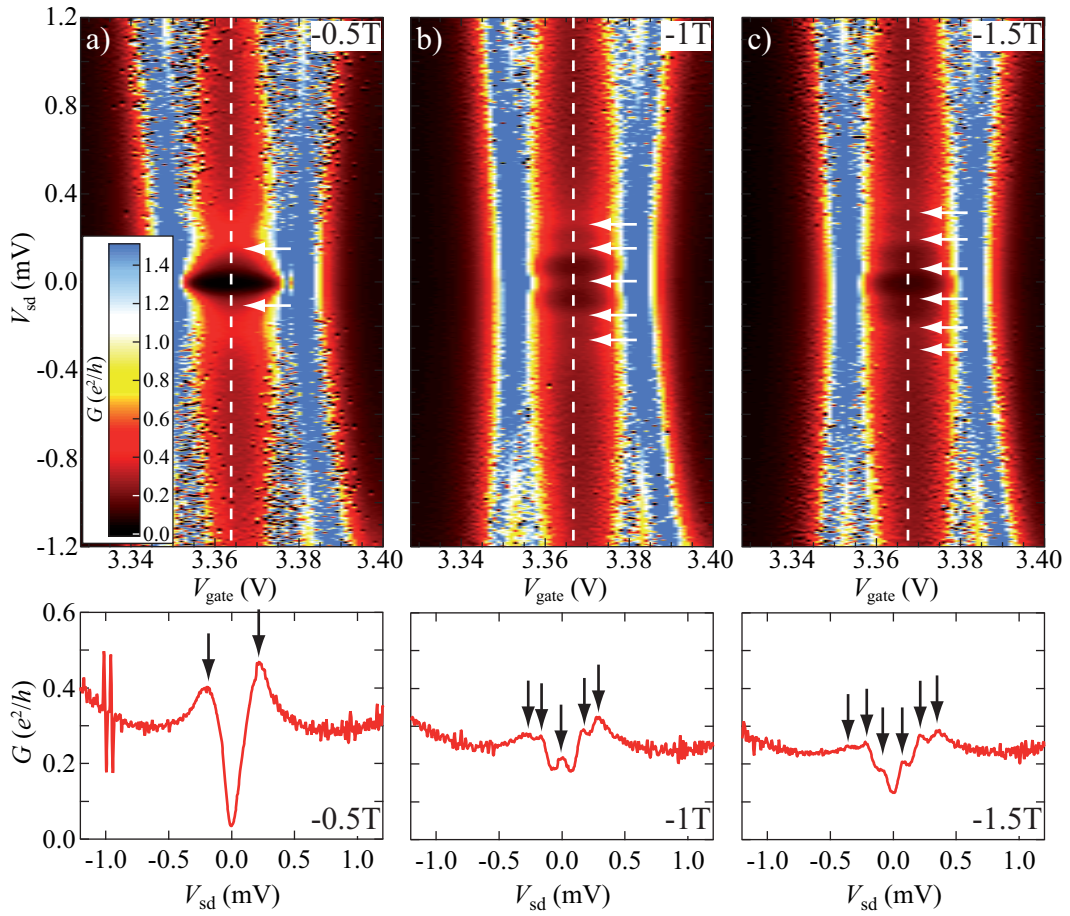


**Figure 9.3.:** Differential conductance for (a)  $B = -0.5\text{ T}$ , (b)  $B = -1\text{ T}$ , and (c)  $B = -1.5\text{ T}$ . The panels underneath each of the color scale plots show line traces along the dashed white lines in the upper panels. At  $B = -0.5\text{ T}$  the conductance shows the same feature as explained in the main text, two resonances at finite voltages. Increasing the field to higher absolute values however reveals a variety of peaks. Note that the conductance at zero bias changes from a minimum to a maximum and back to a minimum from left to right.

As perspective, the research presented here makes it conceivable to employ the different contributions from the Stoner field and the polarization to tailor the magnetic contacts such that the ground state spin of the quantum dot can be adjusted purely electrically [48]. Currently work is being continued in the direction of using exchange biased bilayers to stabilize the magnetization. In these materials, usually a ferromagnetic layer is combined with an antiferromagnetic one. The result is that the center of the hysteresis curve of such a bilayer system is shifted away from zero external field.

In addition, a very recent discussion revolves around potentially spin polarized transport channels being established by the Kondo effect. A combination of two such Kondo quantum dots in a double quantum dot may increase greatly the filter efficiency for a certain

spin direction. An application of such quantum dots under the influence of an exchange field can be imagined in the context of the recently introduced Cooper pair beam splitters [110, 111]. If signals at the two arms of such a beam splitter are found to depend on the potential spin selectivity induced by the Kondo dots, this can be seen as an indication of splitting a Cooper pair into two single, entangled electrons.

Research is by far not restricted to carbon nanotubes. It should in principle be easily extendable, e.g., to transport experiments in semiconductor nanowires. Such nanowires also represent a unique system for exploring phenomena at the nanoscale; they are expected to play a critical role in future electronic and optoelectronic devices [112]. Especially III-V nanowires, e.g. InAs or InSb, show very large  $g$ -factors [113]. The possibility to influence spin states should benefit from this fact. Similar experiments can also be performed in graphene, where the argument for the absence of hyperfine interaction in  $^{12}\text{C}$  remains. Additionally, the curvature induced spin-orbit interaction should not be present in the planar sheets of graphene. Spin injection and precession experiments in graphene show very promising spin coherence, see e.g. Ref. [114].

Besides these various alternative material systems, also nanotubes of course retain a high potential for fundamental research. A rapidly growing field of research deals with experiments employing the mechanical properties, briefly mentioned at the beginning of this work. It was shown for instance in Ref. [115] that a strong coupling between single-electron tunneling and nanomechanical motion is possible.

In summary, the experiments presented here demonstrate the versatility of quantum dots in general and carbon nanotubes in particular. The combination of a prominent example for a many particle phenomenon, the Kondo effect, and spin-selective spectroscopy of the quantum dot levels by transport experiments resulted in new insights. By employing similar combinations in hybrid systems, the research area of low temperature mesoscopic physics certainly will see many more fruitful discoveries in the future.



# A. Sample preparation parameters

The preparation parameters given in this chapter were used to fabricate all the samples mentioned in the main part of the thesis. Especially the parameters for the nanotube growth should be seen as a guide for potentially good growth results. Practice showed that the growth conditions can vary substantially even between consecutive growth processes and that the "sweet spot" of the CVD system is undergoing constant change.

## A.1. Substrate and alignment marks

For the substrate a highly doped (p++) silicon wafer with a thermally oxidized top layer of  $\text{SiO}_2$  is used. The oxide layer is typically 300 nm thick. The used wafers are 2" or 4" in diameter. Depending on the reliability of the process these are either cut into smaller pieces of  $4\text{ mm} \times 4\text{ mm}$  or, for a scaled up process,  $16\text{ mm} \times 16\text{ mm}$ .

The pattern for the alignment marks and the catalyst dot array both are defined by electron beam lithography (EBL). For the catalyst dots the lift-off after deposition often poses problems with a single layer of PMMA. For that reason a double layer system is employed in this step. The two layers are made up of PMMA with a molecular weight of 950K at 2% concentration in chlorobenzene on top of PMMA 200K at 7% concentration. The single layer resist for the alignment marks is made of PMMA 200K at 3.5% concentration.

After spin coating the samples, the resist is baked on a hot plate at  $150^\circ\text{C}$ . The spin coating is done in two stages. In the first stage the rotations per minute are set to 3000 for a duration of 5 s and an acceleration of 0. The second stage is 30 s at 8000 rpm and an acceleration of 9. The parameters for the electron beam that work for these resists were

- 25 kV acceleration voltage,  $195\mu\text{C}/\text{cm}^2$  for the alignment marks
- 25 kV acceleration voltage,  $300\mu\text{C}/\text{cm}^2$  for the catalyst dots.

The developing of the structure is done by rinsing the sample gently for 30 s in a mixture of one volume part MIBK and three volume parts 2-propanol. After that the sample is rinsed with 2-propanol and blown dry.

For the alignment marks, depending on whether the nanotubes are grown before or after, usually 40 nm of rhenium or gold are deposited. More details on processing the catalyst dots are given in the next section.

## A.2. Nanotube growth

As already mentioned in the main text, the nanotubes used in the presented experiments were produced in an upscaled process yielding a large number of samples. Processing was done by L. Herrmann in the framework of his thesis [95]. The parameters given here rely on these experiences.

### A.2.1. Catalyst

The catalyst is composed of:

- 30 ml methanol
- 40.0 mg  $\text{Fe}(\text{NO}_3)_3 \cdot 9 \text{H}_2\text{O}$  (Fluka Chemie AG)
- 30.0 mg  $\text{Al}_2\text{O}_3$  nanoparticles (diameter about 14 nm, Degussa GmbH)
- 10.0 mg  $[\text{CH}_3\text{COCH}=\text{C}(\text{O}-)\text{CH}_3]_2\text{MoO}_3$  (Sigma-Aldrich Chemie GmbH)

The catalyst suspension is brought onto the chip in following steps:

- stir suspension for 30 min
- prepare warm (60 °C) acetone
- use clean (rinse with propanol and methanol) glas pipette to disperse suspension on the sample
- gently blow the sample dry with nitrogen at a small angle
- put the sample on a heating plate at 150 °C for 6 min
- check the sample under the optical microscope for deposited catalyst
- disperse the sample upside down in the previously prepared warm acetone for lift-off
- clean the sample in two steps by rinsing it with acetone and submersing it in propanol for 30s
- blow the sample dry with nitrogen and once more check the result under the optical microscope

### A.2.2. Growth

- center the sample in the 1'' quartz tube closely to the thermometer of the oven
- seal the quartz tube tightly
- flush quartz tube with process gases (methane, argon, and hydrogen) for 2 min



- flush tube for another 2 min with pure argon at a flow of 1500 sccm
- with constant argon flow, heat furnace to 900°C
- set hydrogen flow to 700 sccm
- stop argon flow
- start the growth process: set methane flow to 760 sccm for 15 min
- end the growth process: stop methane flow
- flush quartz tube with 1500 sccm argon
- stop heater and open furnace; let the sample cool down to 600°C in flow of argon and hydrogen
- at 600°C stop the hydrogen flow; keep up argon flow at least down to 150°C
- stop all gas flows at below 150°C

Recent enhancements of the CVD system, like improving the tightness of the gas flow connection to the glass tube, changed these parameters significantly and growth, at the time of writing this, works best for a gas flow of 1 sccm methane and 2 sccm hydrogen at a growth temperature of 850°C

### A.3. Electron beam lithography and metallization

The EBL for the contacts to the tube is performed in two steps. In the first step the bonding pads and the leads towards the area where the tube was identified are structured. In the second step, exclusively the ferromagnetic contacts are lithographically defined. This way first the bonding pads and the leads can be deposited as a double layer of titanium and gold, both of which are non-magnetic. The ferromagnetic contacts are simple rectangles, and the domain structure is expected to be as regular as possible.

The EBL parameters for the pads and leads were

- PMMA 200K at 7%; 10 min postbake at 150°C.

For the different structure sizes different apertures were used in order to minimize the writing time; these were

- 30µm (74pA)
- 60µm (1300pA)
- 120µm (4800pA)

with the average current given in parenthesis. To develop the structure, the same process is used as given above for the alignment marks.

The metal is deposited in a vacuum chamber. For the pads and leads following parameters were used:

- 5 nm of Ti at an e-gun current of 40 mA and a rate of 1.4 Å/s
- 50 nm of Au thermally evaporated at a current of 130 A and a rate of 2 Å/s.

The lift-off is done in warm acetone, typically over night. After that, for the second eBL step, the sample is once more spin coated with the same resist (700K at 7%) and baked at 150 °C for 10 min.

The lithography for the ferromagnetic contacts is done by aligning the contacts with reference to the previously deposited gold leads. This step is written with an aperture of 30 μm.

Note that the scanning area of the image that is taken for connecting sample and microscope stage positions has to be the same as for the writing step. If the software adjusts the magnification of the microscope between the positioning and the writing a shift results that could in extreme cases end in disconnected sample structures.

## B. Measurement Scripts

This part of the appendix is intended to give a quick example of a measurement script that was used to conduct a simple measurement of the current  $I$  as a function of the voltage  $V$ . The scripts are based on the Lab::VISA Perl package, which was recently renamed to Lab::Measurement, see <http://www.labmeasurement.de/>. The voltage from a Yokogawa voltage source is swept from  $-1\text{ mV}$  to  $1\text{ mV}$  in steps of  $2\text{ }\mu\text{V}$  and the current through the device is read in from a digital multimeter. In the header of the script the device drivers and other utilities are loaded by the `use` command.

```
#!/usr/bin/perl

use strict;
use Lab::Instrument::Yokogawa7651;
use Lab::Instrument::HP3458A;
use Time::HiRes qw/usleep/;
use Lab::Measurement;
```

In this case the instruments are a Yokogawa current source and an Agilent digital multimeter (HP3458A). The package `Lab::Measurement` provides the main functions to construct the actual measurement.

Then the sweep parameters, the GPIB addresses of the instruments, and some constants are defined. Also the name of the destination file is given here. For the convenience of the user also a comment can be edited that is written automatically written into a meta file that contains useful information about the measurement.

```
my $start_sd=-1.000;
my $stop_sd=1.000;
my $step_sd=0.002;

my $gate_v=0;

my $gpib_sd=5;
my $type_sd="Lab::Instrument::Yokogawa7651";

my $gpib_hp=22;
my $hp=new Lab::Instrument::HP3458A(0,$gpib_hp);
$hp->set_nplc(0.1);

my $amp=1e-8;      # Ithaco amplification
my $Vdiv=1.088e-3;
```

```

my $name_gate = "Backgate";

my $sample="Sample_BA_-_Structure_22C";
my $title="1D_Biassweep";
my $filename="BiassweepVg=0V_B=0T_T=4p2K";

my $comment=<<COMMENT;
Yokogawa:    V_{SD}=$start_sd..$stop_sd mV an 3;
Ithaco:      Amplification $amp an 9, Rise Time 300 ms;
Gate:        $name_gate = $gate_v V;
Temperature: T = 4.2 K;
Vdiv:        Vsd = 1000:1;
GateResist:  10 MOhm
COMMENT

```

This next block initializes the voltage source at a certain GPIB address. Additionally some convenience functionalities like a maximum step size for that device can be supplied.

```

my $source_sd=new $type_sd({
  'GPIB_board'    => 0,
  'GPIB_address'  => $gpib_sd,
  'gate_protect'  => 0,

  'gp_max_volt_per_second' => 10,
  'gp_max_volt_per_step'  => 1,
  'gp_min_volt'    => -10,
  'gp_max_volt'    => 10, });

```

The following block contains the main part of the script, namely the actual measurement. The measurement itself is an object that has different methods and attributes. One attribute e.g. is the sample name for this measurement. Another one could be a live plot. The script launches a plotting tool at the beginning of the measurement and updates the plot every second. In the attributes constants, columns, and axes parameters are supplied to display the data correctly scaled and on the real physical axes. The actual measurement is then started by calling the method `start_block()`. The method `log_line()`, e.g., writes its arguments to a file named `filename`. The source and the multimeter objects know such methods as `set_voltage()` or `read_value()` that hardly need any further explanation.

```

my $measurement=new Lab::Measurement(
  sample      => $sample,
  title       => $title,
  filename_base => $filename,
  description  => $comment,

  live_plot   => 'IV-Curve',
  live_refresh => '1',

```

```

constants      => [
  {
    'name'       => 'AMP',
    'value'      => $amp,
  },
],
columns        => [
  {
    'unit'       => 'V',
    'label'      => 'Source-drain_voltage',
    'description' => 'Applied_via_1000:1_divider',
  },
  {
    'unit'       => 'V',
    'label'      => 'Amplifier_output',
    'description' => "Voltage_at_current_amplifier_set_to_$amp.",
  }
],
axes           => [
  {
    'unit'       => 'V',
    'expression' => '$C0',
    'label'      => 'source-drain_voltage',
    'min'        => ($start_sd<$stop_sd) ? $start_sd:$stop_sd,
    'max'        => ($start_sd<$stop_sd) ? $stop_sd:$start_sd,
    'description' => 'Applied_via_1000:1_divider',
  },
  {
    'unit'       => 'A',
    'expression' => "\$C1*AMP",
    'label'      => 'current',
    'description' => 'Current_through_dot',
#    'min'        => 0,
  },
],
plots          => [
  'IV-Curve'    => {
    'type'       => 'line',
    'xaxis'      => 0,
    'yaxis'      => 1,
    'grid'       => 'xtics,ytics',
  },
],
);

my $stepsign_sd=$step_sd/abs($step_sd);

$measurement->start_block();
$measurement->log_line("#Vbias_raw","Current_raw","Vbias","Current");

```

```
for (my $volt_sd=$start_sd;  
      $stepsign_sd*$volt_sd<=$stepsign_sd*$stop_sd;  
      $volt_sd+=$step_sd)  
{  
  
    $source_sd->set_voltage($volt_sd);  
  
    my $meas=$hp->read_value();  
  
    my $real=$volt_sd;  
  
    $measurement->log_line($real,$meas,$real*$Vdiv,$meas*$amp);  
}  
  
my $meta=$measurement->finish_measurement();
```

# Bibliography

- [1] G. E. Moore, “Cramming more components onto integrated circuits,” *IEEE Solid-State Circuits Newsletter*, vol. 38, p. 114, 1965.
- [2] see e.g. the ‘International Technology Roadmap for Superconductors’, <http://www.itrs.net/> (checked Nov. 29th 2011).
- [3] W. Gerlach and O. Stern, “Der experimentelle Nachweis der Richtungsquantelung im Magnetfeld,” *Zeitschrift für Physik*, vol. 9, p. 349, 1922.
- [4] S. D. Sarma, “Spintronics,” *American Scientist*, vol. 89, p. 516, 2001.
- [5] S. Datta and B. Das, “Electronic analog of the electro-optic modulator,” *Applied Physics Letters*, vol. 56, p. 665, 1990.
- [6] I. Žutić, J. Fabian, and S. D. Sarma, “Spintronics: Fundamentals and applications,” *Reviews of Modern Physics*, vol. 76, p. 323, 2004.
- [7] H. O. H. Churchill, A. J. Bestwick, J. W. Harlow, F. Kuemmeth, D. Marcos, C. H. Stwertka, S. K. Watson, and C. M. Marcus, “Electron–nuclear interaction in  $^{13}\text{C}$  nanotube double quantum dots,” *Nature Physics*, vol. 5, p. 321, 2009.
- [8] T. Jespersen, K. Grove-Rasmussen, J. Paaske, K. Muraki, T. Fujisawa, J. Nygård, and K. Flensberg, “Gate-dependent spin-orbit coupling in multielectron carbon nanotubes,” *Nature Physics*, vol. 5, p. 348, 2011.
- [9] F. Kuemmeth, S. Ilani, D. C. Ralph, and P. L. McEuen, “Coupling of spin and orbital motion of electrons in carbon nanotubes,” *Nature*, vol. 452, p. 448, 2008.
- [10] S. Sahoo, T. Kontos, C. Schönenberger, and C. Sürgers, “Electrical spin injection in multiwall carbon nanotubes with transparent ferromagnetic contacts,” *Applied Physics Letters*, vol. 86, 2005.
- [11] A. Jensen, J. R. Hauptmann, J. Nygård, and P. E. Lindelof, “Magnetoresistance in ferromagnetically contacted single-wall carbon nanotubes,” *Physical Review B*, vol. 72, p. 35419, 2005.
- [12] A. Cottet, T. Kontos, S. Sahoo, H. T. Man, M.-S. Choi, W. Belzig, C. Bruder, A. F. Morpurgo, and C. Schönenberger, “Nanospintronics with carbon nanotubes,” *Semiconductor Science and Technology*, vol. 21, p. S78, 2006.
- [13] H. Man, I. Wever, and A. Morpurgo, “Spin-dependent quantum interference in single-wall carbon nanotubes with ferromagnetic contacts,” *Physical Review B*,



- vol. 73, p. 241401, 2006.
- [14] C. Feuillet-Palma, T. Delattre, P. Morfin, J.-M. Berroir, G. Fève, D. C. Glattli, B. Plaçais, A. Cottet, and T. Kontos, “Conserved spin and orbital phase along carbon nanotubes connected with multiple ferromagnetic contacts,” *Physical Review B*, vol. 81, p. 115414, 2010.
  - [15] Z. Yao, C. L. Kane, and C. Dekker, “High-field electrical transport in single-wall carbon nanotubes,” *Physical Review Letters*, vol. 84, p. 2941, 2000.
  - [16] M. M. J. Treacy, T. W. Ebbesen, and J. M. Gibson, “Exceptionally high Young’s modulus observed for individual carbon nanotubes,” *Nature*, vol. 381, p. 678, 1996.
  - [17] J.-P. Salvetat, G. Briggs, J.-M. Bonard, R. Bacsá, A. Kulik, T. Stöckli, N. Burnham, and L. Forró, “Elastic and Shear Moduli of Single-Walled Carbon Nanotube Ropes,” *Physical Review Letters*, vol. 82, p. 944, 1999.
  - [18] Z. Liu, K. Chen, C. Davis, S. Sherlock, Q. Cao, X. Chen, and H. Dai, “Drug delivery with carbon nanotubes for in vivo cancer treatment,” *Cancer research*, vol. 68, p. 6652, 2008.
  - [19] S. Iijima, “Helical microtubules of graphitic carbon,” *Nature*, vol. 354, p. 56, 1991.
  - [20] S. Iijima and T. Ichihashi, “Single-shell carbon nanotubes of 1-nm diameter,” *Nature*, vol. 363, p. 603, 1993.
  - [21] D. S. Bethune, C. H. Klang, M. S. de Vries, G. Gorman, R. Savoy, J. Vazquez, and R. Beyers, “Cobalt-catalysed growth of carbon nanotubes with single-atomic-layer walls,” *Nature*, vol. 363, p. 605, 1993.
  - [22] U. Vohrer and N. Zschoerper, “Kohlenstoff-Nanoröhren – Phönix aus der Asche,” *Vakuum in Forschung und Praxis*, vol. 19, p. 22, 2007.
  - [23] L. V. Radushkevich and V. M. Lukyanovich, “The structure of carbon formed by thermal decomposition of carbon monoxide on iron contacts,” *Russian Journal of Physical Chemistry*, vol. 26, p. 88, 1952.
  - [24] J. Kong, H. Soh, A. Cassell, C. Quate, and H. Dai, “Synthesis of individual single-walled carbon nanotubes on patterned silicon wafers,” *Nature*, vol. 395, p. 878, 1998.
  - [25] S. J. Tans, M. H. Devoret, H. Dai, A. Thess, R. E. Smalley, L. J. Geerligs, and C. Dekker, “Individual single-wall carbon nanotubes as quantum wires,” *Nature*, vol. 386, p. 474, 1997.
  - [26] L. C. Venema, J. W. G. Wilder, C. Dekker, A. G. Rinzler, and R. E. Smalley, “Electronic structure of atomically resolved carbon nanotubes,” *Nature*, vol. 391, p. 59, 1998.
  - [27] P. Jarillo-Herrero, S. Sapmaz, C. Dekker, L. P. Kouwenhoven, and H. S. J. van der Zant, “Electron-hole symmetry in a semiconducting carbon nanotube quantum

- dot,” *Nature*, vol. 429, p. 389, 2004.
- [28] S. Sapmaz, P. J. Herrero, J. Kong, C. Dekker, L. P. Kouwenhoven, and H. S. J. van der Zant, “Electronic excitation spectrum of metallic carbon nanotubes,” *Physical Review B*, vol. 71, p. 153402, 2005.
- [29] W. Liang, M. Bockrath, D. Bozovic, J. Hafner, M. Tinkham, and H. Park, “Fabry-Perot interference in a nanotube electron waveguide,” *Nature*, vol. 411, p. 665, 2001.
- [30] A. Bachtold, C. Strunk, J.-P. Salvetat, J.-M. Bonard, L. Forró, T. Nussbaumer, and C. Schönenberger, “Aharonov–Bohm oscillations in carbon nanotubes,” *Nature*, vol. 397, p. 673, 1999.
- [31] K. Grove-Rasmussen, H. I. Jorgensen, and P. E. Lindelof, “Fabry–Perot interference, Kondo effect and Coulomb blockade in carbon nanotubes,” *Physica E: Low-dimensional Systems and Nanostructures*, vol. 40, p. 92, 2007.
- [32] G. van den Berg and J. de Nobel, “Les propriétés à basses températures des alliages des métaux normaux avec des solutés de transition,” *Journal de Physique et le Radium*, vol. 23, p. 665, 1962.
- [33] J. Rowell and L. Shen, “Zero-Bias Anomalies in Normal Metal Tunnel Junctions,” *Physical Review Letters*, vol. 17, p. 15, 1966.
- [34] D. van Delft and P. Kes, “The discovery of superconductivity,” *Physics Today*, vol. 63, p. 38, 2010.
- [35] J. Kondo, “Resistance Minimum in Dilute Magnetic Alloys,” *Progress of Theoretical Physics*, vol. 32, p. 37, 1964.
- [36] J. Appelbaum, “Exchange Model of Zero-Bias Tunneling Anomalies,” *Physical Review*, vol. 154, p. 633, 1967.
- [37] P. Anderson, “Localized Magnetic States and Fermi-Surface Anomalies in Tunneling,” *Physical Review Letters*, vol. 17, p. 95, 1966.
- [38] K. Wilson, “The renormalization group: Critical phenomena and the Kondo problem,” *Reviews of Modern Physics*, vol. 47, p. 773, 1975.
- [39] L. P. Kouwenhoven and L. Glazman, “Revival of the Kondo effect,” *Physics World*, vol. 14, p. 33, 2001.
- [40] D. Goldhaber-Gordon, H. Shtrikman, D. Mahalu, D. Abusch-Magder, U. Meirav, and M. A. Kastner, “Kondo effect in a single-electron transistor,” *Nature*, vol. 391, p. 156, 1998.
- [41] S. M. Cronenwett, T. H. Oosterkamp, and L. P. Kouwenhoven, “A Tunable Kondo Effect in Quantum Dots,” *Science*, vol. 281, p. 540, 1998.
- [42] J. Schmid, J. Weis, K. Eberl, and K. v. Klitzing, “A quantum dot in the limit of

- strong coupling to reservoirs,” *Physica B: Condensed Matter*, vol. 256-258, p. 182, 1998.
- [43] J. Nygård, D. H. Cobden, and P. E. Lindelof, “Kondo physics in carbon nanotubes,” *Nature*, vol. 408, p. 342, 2000.
- [44] M. Pustilnik and L. Glazman, “Kondo effect in quantum dots,” *Journal of Physics: Condensed Matter*, vol. 16, p. R513, 2004.
- [45] K. Hamaya, M. Kitabatake, K. Shibata, M. Jung, M. Kawamura, K. Hirakawa, T. Machida, T. Taniyama, S. Ishida, and Y. Arakawa, “Kondo effect in a semiconductor quantum dot coupled to ferromagnetic electrodes,” *Applied Physics Letters*, vol. 91, 2007.
- [46] T. Kobayashi, S. Tsuruta, S. Sasaki, T. Fujisawa, Y. Tokura, and T. Akazaki, “Kondo Effect in a Semiconductor Quantum Dot with a Spin-Accumulated Lead,” *Physical Review Letters*, vol. 104, 2010.
- [47] A. N. Pasupathy, R. C. Bialczak, J. Martinek, J. E. Grose, L. A. K. Donev, P. L. McEuen, and D. C. Ralph, “The kondo effect in the presence of ferromagnetism,” *Science*, vol. 306, p. 86, 2004.
- [48] J. R. Hauptmann, J. Paaske, and P. E. Lindelof, “Electric-field-controlled spin reversal in a quantum dot with ferromagnetic contacts,” *Nature Physics*, vol. 4, p. 373, 2008.
- [49] J. Martinek, Y. Utsumi, H. Imamura, J. Barnaś, S. Maekawa, J. König, and G. Schön, “Kondo Effect in Quantum Dots Coupled to Ferromagnetic Leads,” *Physical Review Letters*, vol. 91, p. 127203, 2003.
- [50] J. König, J. Martinek, J. Barnas, and et al., “Quantum Dots Attached to Ferromagnetic Leads: Exchange Field, Spin Precession, and Kondo Effect,” in *Lecture Notes in Physics* (K. Busch, et al., ed.), vol. 658, p. 145, Springer Verlag, 2005.
- [51] M. S. Choi, D. Sánchez, and R. López, “Kondo Effect in a Quantum Dot Coupled to Ferromagnetic Leads: A Numerical Renormalization Group Analysis,” *Physical Review Letters*, vol. 92, p. 056601, 2004.
- [52] J. Martinek, M. Sindel, L. Borda, J. Barnaś, R. Bulla, J. König, G. Schön, S. Maekawa, and J. von Delft, “Gate-controlled spin splitting in quantum dots with ferromagnetic leads in the Kondo regime,” *Physical Review B*, vol. 72, p. 121302, 2005.
- [53] M. Sindel, L. Borda, J. Martinek, R. Bulla, J. König, G. Schön, S. Maekawa, and J. von Delft, “Kondo quantum dot coupled to ferromagnetic leads: Numerical renormalization group study,” *Physical Review B*, vol. 76, p. 045321, 2007.
- [54] I. Weymann and L. Borda, “Underscreened Kondo effect in quantum dots coupled to ferromagnetic leads,” *Physical Review B*, vol. 81, p. 115445, 2010.

- [55] D. Steininger, *Magnetische Eigenschaften von mesoskopischen PdFe und PdNi Streifen*. Diplomarbeit, Universität Regensburg, 2009.
- [56] J. C. Ododo, “The onset of ferromagnetism in transition metal alloys as a cooperative phase transition,” *Journal of Physics F: Metal Physics*, vol. 10, p. 2515, 1980.
- [57] J. C. Ododo, “Percolation concentration and saturation of the Pd moment in ferromagnetic Pd alloys,” *Journal of Physics F: Metal Physics*, vol. 13, p. 1291, 1983.
- [58] J.-Y. Chauleau, B. J. McMorran, R. Belkhou, N. Bergéard, T. O. Menteş, M. Niño, A. Locatelli, J. Unguris, S. Rohart, J. Miltat, and A. Thiaville, “Magnetization textures in nipd nanostructures,” *Phys. Rev. B*, vol. 84, p. 094416, 2011.
- [59] R. Saito, G. Dresselhaus, and M. S. Dresselhaus, *Physical Properties of Carbon Nanotubes*. London: Imperial College Press, 1998.
- [60] E. Thune and C. Strunk, “Quantum Transport in Carbon Nanotubes,” vol. 680 of *Lecture Notes in Physics*, book part (with own title) 14, p. 351, Berlin: Springer Verlag, 2005.
- [61] J.-C. Charlier, X. Blase, and S. Roche, “Electronic and transport properties of nanotubes,” *Reviews of Modern Physics*, vol. 79, p. 677, 2007.
- [62] K. S. Novoselov, A. K. Geim, S. V. Morozov, D. Jiang, Y. Zhang, S. V. Dubonos, I. V. Grigorieva, and A. A. Firsov, “Electric field effect in atomically thin carbon films,” *Science*, vol. 306, p. 666, 2004.
- [63] M. S. Dresselhaus, G. Dresselhaus, and P. Avouris, *Carbon Nanotubes - Synthesis, Structure, Properties, and Applications*. Springer Verlag, Berlin, 2001.
- [64] X. Blase, L. Benedict, E. Shirley, and S. Louie, “Hybridization effects and metallicity in small radius carbon nanotubes,” *Physical Review Letters*, vol. 72, p. 1878, 1994.
- [65] M. Büttiker, Y. Imry, R. Landauer, and S. Pinhas, “Generalized many-channel conductance formula with application to small rings,” *Physical Review B*, vol. 31, p. 6207, 1985.
- [66] C. Schönenberger, A. Bachtold, C. Strunk, J.-P. Salvetat, and L. Forró, “Interference and Interaction in multi-wall carbon nanotubes,” *Applied Physics A: Materials Science & Processing*, vol. 69, p. 283, 1999.
- [67] N. Nemec, *Quantum transport in carbon-based nanostructures*. PhD thesis, Universität Regensburg, 2007.
- [68] L. L. Sohn, L. P. Kouwenhoven, and G. Schön, *Mesoscopic electron transport*. NATO ASI series: Applied sciences, Dordrecht: Kluwer Academic Publishers, 1997.
- [69] L. P. Kouwenhoven, C. M. Marcus, P. L. McEuen, S. Tarucha, R. M. Westervelt,

- and N. S. Wingreen, "Electron transport in quantum dots," in *Mesoscopic Electron Transport* (Sohn, L. L. and Kouwenhoven, L. P. and Schön, G., ed.), vol. 345, p. 105, 1997.
- [70] L. P. Kouwenhoven and C. M. Marcus, "Quantum Dots," *Physics World*, vol. 11, p. 35, 1998.
- [71] A. K. Hüttel, *Gekoppelte Quantenpunkte im Bereich niedrigster Elektronenzahlen*. PhD thesis, Ludwig-Maximilians-Universität München, 2005.
- [72] L. P. Kouwenhoven, N. C. Vaart, A. T. Johnson, W. Kool, C. J. P. M. Harmans, J. G. Williamson, A. A. M. Staring, and C. T. Foxon, "Single electron charging effects in semiconductor quantum dots," *Zeitschrift für Physik B Condensed Matter*, vol. 85, pp. 367–373, 1991.
- [73] H. Grabert, "Single charge tunneling: A brief introduction," *Zeitschrift für Physik B Condensed Matter*, vol. 85, p. 319, 1991.
- [74] U. Meirav, P. L. McEuen, M. A. Kastner, E. B. Foxman, A. Kumar, and S. J. Wind, "Conductance oscillations and transport spectroscopy of a quantum dot," *Zeitschrift für Physik B Condensed Matter*, vol. 85, p. 357, 1991.
- [75] C. W. J. Beenakker, "Theory of Coulomb-blockade oscillations in the conductance of a quantum dot," *Physical Review B*, vol. 44, p. 1646, 1991.
- [76] S. Sapmaz, P. Jarillo-Herrero, L. P. Kouwenhoven, and H. S. J. van der Zant, "Quantum dots in carbon nanotubes," *Semiconductor Science and Technology*, vol. 21, p. S52, 2006.
- [77] H. Grabert and M. H. Devoret, *Single charge tunneling: Coulomb blockade phenomena in nanostructures*, vol. 294 of *NATO ASI series: Physics*. New York: Plenum Press, 1992.
- [78] I. O. Kulik and R. I. Shekhter, "Kinetic phenomena and charge discreteness effects in granulated media," *Soviet Physics - JETP*, vol. 41, p. 308, 1975.
- [79] D. V. Averin and K. K. Likharev, "Coulomb blockade of single-electron tunneling, and coherent oscillations in small tunnel junctions," *Journal of Low Temperature Physics*, vol. 62, p. 345, 1986.
- [80] H. Van Houten, C. W. J. Beenakker, and A. A. M. Staring, "Coulomb-Blockade Oscillations in Semiconductor Nanostructures," in *Single charge tunneling: Coulomb blockade phenomena in nanostructures* (H. Grabert and M. H. Devoret, eds.), p. 167, 1992.
- [81] P. E. Lindelof, J. Borggreen, A. Jensen, J. Nygård, and P. R. Poulsen, "Electron Spin in Single Wall Carbon Nanotubes," *Physica Scripta*, vol. T102, p. 22, 2002.
- [82] E. Pallecchi, M. Gaass, D. A. Ryndyk, and C. Strunk, "Carbon nanotube Josephson junctions with Nb contacts," *Applied Physics Letters*, vol. 93, p. 072501, 2008.

- [83] Y. Oreg, K. Byczuk, and B. Halperin, “Spin Configurations of a Carbon Nanotube in a Nonuniform External Potential,” *Physical Review Letters*, vol. 85, p. 365, 2000.
- [84] W. Buckel and R. Kleiner, *Supraleitung*. Weinheim: WILEY-VCH Verlag GmbH & Co. KGaA, 2004.
- [85] A. Hewson, *The Kondo Problem to Heavy Fermions*. Cambridge: Cambridge University Press, 1993.
- [86] W. G. van der Wiel, *Electron transport and coherence in semiconductor quantum dots and rings*. PhD thesis, Technische Universiteit Delft, 2002.
- [87] P. Anderson, “Localized Magnetic States in Metals,” *Physical Review*, vol. 124, p. 41, 1961.
- [88] T. K. Ng and P. A. Lee, “On-Site Coulomb Repulsion and Resonant Tunneling,” *Physical Review Letters*, vol. 61, p. 1768, 1988.
- [89] L. Glazman and M. E. Raikh, “Resonant Kondo transparency of a barrier with quasilocal impurity states,” *JETP Lett.*, vol. 47, p. 452, 1988.
- [90] D. Goldhaber-Gordon, J. Göres, M. Kastner, H. Shtrikman, D. Mahalu, and U. Meirav, “From the Kondo Regime to the Mixed-Valence Regime in a Single-Electron Transistor,” *Physical Review Letters*, vol. 81, p. 5225, 1998.
- [91] T. A. Costi, A. C. Hewson, and V. Zlatic, “Transport coefficients of the Anderson model via the numerical renormalization group,” *Journal of Physics: Condensed Matter*, vol. 6, p. 2519, 1994.
- [92] F. Schwabl, *Quantenmechanik*. Berlin: Springer Verlag, 6 ed., 2002.
- [93] J. Martinek, M. Sindel, L. Borda, J. Barnaś, J. König, G. Schön, and J. von Delft, “Kondo Effect in the Presence of Itinerant-Electron Ferromagnetism Studied with the Numerical Renormalization Group Method,” *Physical Review Letters*, vol. 91, p. 247202, 2003.
- [94] T. Kreutz, T. Greber, P. Aebi, and J. Osterwalder, “Temperature-dependent electronic structure of nickel metal,” *Physical Review B*, vol. 58, p. 1300, 1998.
- [95] L. Herrmann, *Carbon nanotubes as Cooper pair beam splitters*. PhD thesis, Universität Regensburg, 2010.
- [96] S. Sahoo, T. Kontos, J. Furer, C. Hoffmann, M. Gräber, A. Cottet, and C. Schönenberger, “Electric field control of spin transport,” *Nature Physics*, vol. 1, p. 99, 2005.
- [97] A. Javey, J. Guo, Q. Wang, M. Lundstrom, and H. Dai, “Ballistic carbon nanotube field-effect transistors,” *Nature*, vol. 424, p. 654, 2003.
- [98] T. Kontos, M. Aprili, J. Lesueur, X. Grison, and L. Dumoulin, “Superconducting Proximity Effect at the Paramagnetic-Ferromagnetic Transition,” *Physical Review*



- Letters*, vol. 93, p. 137001, 2004.
- [99] J. W. Loram and K. A. Mirza, "Dilute PdNi-a homogeneous magnetic system of fluctuating moments," *Journal of Physics F: Metal Physics*, vol. 15, p. 2213, 1985.
  - [100] J. Gonzalez-Pons, J. Henderson, E. del Barco, and B. Ozyilmaz, "Geometrical control of the magnetization direction in high aspect-ratio PdNi ferromagnetic nanoelectrodes," *Physical Review B*, vol. 78, p. 4, 2008.
  - [101] D. Steininger, A. Hüttel, D. Preusche, M. Ziola, M. Kiessling, M. Sperl, G. Bayreuther, and C. Strunk, "Electric and magnetic characterization of PdNi contact electrodes," *in preparation*, 2011.
  - [102] F. Pobell, *Matter and Methods at Low Temperatures*. Berlin: Springer Verlag, 1992.
  - [103] C. Strunk, *Moderne Thermodynamik*. Berlin: Springer Verlag, in preparation.
  - [104] S. Koller, L. Mayrhofer, and M. Grifoni, "Spin transport across carbon nanotube quantum dots," *New Journal of Physics*, vol. 9, p. 348, 2007.
  - [105] A. V. Kretinin, H. Shtrikman, D. Goldhaber-Gordon, M. Hanl, A. Weichselbaum, J. von Delft, T. Costi, and D. Mahalu, "Spin-1/2 Kondo effect in a InAs nanowire quantum dot: the Unitary limit, conductance scaling and Zeeman splitting," *arXiv:1108.1773*, 2011.
  - [106] J. v. Delft. private communications, 2011.
  - [107] S. Koller, J. Paaske, and M. Grifoni, "Sources of negative tunneling magneto-resistance in multilevel quantum dots with ferromagnetic contacts," *arXiv:1109.6599*, 2011.
  - [108] T.-F. Fang, W. Zuo, and H.-G. Luo, "Kondo Effect in Carbon Nanotube Quantum Dots with Spin-Orbit Coupling," *Physical Review Letters*, vol. 101, p. 246805, 2008.
  - [109] M. R. Galpin, F. W. Jayatilaka, D. E. Logan, and F. B. Anders, "Interplay between Kondo physics and spin-orbit coupling in carbon nanotube quantum dots," *Physical Review B*, vol. 81, p. 075437, 2010.
  - [110] L. Hofstetter, S. Csonka, J. Nygård, and C. Schönenberger, "Cooper pair splitter realized in a two-quantum-dot Y-junction.," *Nature*, vol. 461, p. 960, 2009.
  - [111] L. G. Herrmann, F. Portier, P. Roche, A. Levi Yeyati, T. Kontos, and C. Strunk, "Carbon Nanotubes as Cooper-Pair Beam Splitters," *Physical Review Letters*, vol. 104, p. 026801, 2010.
  - [112] W. Lu and C. M. Lieber, "Semiconductor nanowires," *Journal of Physics D: Applied Physics*, vol. 39, p. R387, 2006.
  - [113] S. Nadj-Perge, S. M. Frolov, E. P. A. M. Bakkers, and L. P. Kouwenhoven, "Spin-orbit qubit in a semiconductor nanowire.," *Nature*, vol. 468, p. 1084, 2010.



- 
- [114] N. Tombros, C. Jozsa, M. Popinciuc, H. T. Jonkman, and B. J. van Wees, “Electronic spin transport and spin precession in single graphene layers at room temperature.,” *Nature*, vol. 448, p. 571, 2007.
- [115] G. A. Steele, A. K. Hüttel, B. Witkamp, M. Poot, H. B. Meerwaldt, L. P. Kouwenhoven, and H. S. J. van der Zant, “Strong coupling between single-electron tunneling and nanomechanical motion.,” *Science*, vol. 325, p. 1103, 2009.



# Acknowledgments

These last pages are dedicated to everyone who helped me in these last years. Their contributions and support eventually led to the present thesis. Without any of them this would have never been possible. With apologies to anyone who unintentionally remained unmentioned, I would like to specially thank

- my advisor *Prof. Dr. Christoph Strunk*, whom I remember telling me more than seven years ago on the day I approached him with the interest to work in his group that his view on experimental physics is that it means “putting one’s ears closer to nature”. This notion was a constant companion over all these years has stood the test of time. Thank you Christoph for all your support and guidance!
- *Dr. Andreas Hüttel*, whose contribution can not be valued high enough. His appearance in our group presented an extreme boost for my productivity. All of a sudden there was someone who seemed to be an expert in just about anything, be it CVD growth of carbon nanotubes, transport measurements, or data collection and evaluation. Andi, you basically influenced every aspect of my work and I can not thank you enough!
- *Prof. Dr. Kicheon Kang*, who spent his sabbatical in our group. Kicheon, I still remember the first internal workshop you attended during your time with us. Seeing my data, you immediately had the right idea for the underlying physics and not only pointed us in the right direction but also helped me during the whole evaluation. I thank you for this extremely fruitful and enjoyable collaboration!
- *Prof. Dr. Jan von Delft* and *Prof. Dr. Ireneusz Weymann* from the Ludwig-Maximilians University, Munich and the Adam Mickiewicz University, Poznań for the numerical renormalization group calculations and all the help in writing our publication.
- *Prof. Dr. Dieter Weiss*, the head of the chair at which this work was performed, for the excellent equipment of the clean room and all other facilities.
- *Prof. Dr. Milena Grifoni*, with whom we had countless discussions about the renormalization processes and who pointed out the additional contributions from bosonic excitations.
- *Dr. Sergey Mankovsky* who provided the ab initio calculations from which we could

extract the filling fraction and check the assumptions for the magnetization as well as the polarization.

None of the experiments conducted within this work would have been possible without the help of the people “in the background” who keep the micro-cosmos university running. These are especially

- our secretaries Claudia and Elke, who are taking basically all of the bureaucratic weight off of our shoulders.
- our technicians Conny, Uli, Tom, and Michael who are responsible for just about everything from the systems and the facilities in the clean room to every last small pump.
- Christian Haimerl and Thomas Solleder from whom you could *always* get liquid Helium even in times of severe shortages - if you only asked nicely.
- Dieter Riedl and the whole team of the electronics workshop.

Many more people at the university helped in producing this thesis, some with a bit less scientific and a more social component. Especially in dire days of broken samples or blocked Helium circulation this latter component provided what was necessary not to despair. Here I want to mention

- my office mates and long term PhD colleagues and friends Tom and Andi, with whom I did not only share the office space but also many experiences. I have always enjoyed the discussions with you, be it physical, political, sociological, or any other type.
- everyone, who shared a long passage along the way with me. Some of them go as far back as the first semester of my studies. Martin, Flo, Holger, Dominik, Ben, Emiliano, David, and all others - getting to know and becoming friends with you is one of the most valuable experiences I will take away from university.
- all members of our work group that made everyday life at the university what it was. Lunch and coffee breaks, filled with interesting conversations, were a welcome interruption of the office hours. Thank you Martin, Daniel, Maurice, Sasmita, Matthias, Ina, Sung-Ho, Daniel, Peter, and Elisabeth.
- all the members of the chair. It was always a pleasure to work side by side with any of you in the clean room as well as the labs.

At the very end of these acknowledgments I want to thank my family. Especially my girlfriend really deserves this appreciation more than almost anyone else and so I want to thank

- Beate for so many things that it is hard to even get started. It is probably easiest to thank you for simply being you, the most understanding, patient, even-tempered, supportive, and warm-hearted person I have met in my entire life. Yet, an even

bigger achievement is probably that even I did not change that. Thank you for everything!

- my parents for their constant support of which I could always be certain. I hope I will ever get the chance to even start paying you back what I owe you!
- my brother Thomas and my sister Lisa who are not only always there for me, but who give me the feeling that I can and should also be there for them. Thank you so much for this identification.

